2008

Ultrashort Laser Pulse Interaction With Photo-thermo-refractive Glass

Leo Siiman
University of Central Florida

STARS Citation

Siiman, Leo, "Ultrashort Laser Pulse Interaction With Photo-thermo-refractive Glass" (2008). *Electronic Theses and Dissertations, 2004-2019*. 3725.
https://stars.library.ucf.edu/etd/3725

ULTRASHORT LASER PULSE INTERACTION WITH PHOTO-THERMO-REFRACTIVE GLASS

by

LEO A. SIIMAN
B.S. University of Florida, 2001

A dissertation submitted in partial fulfillment of the requirements
for the degree of Doctor of Philosophy
in the College of Optics and Photonics
at the University of Central Florida
Orlando, Florida

Summer Term
2008

Major Professor: Leonid B. Glebov

ABSTRACT

Photo-thermo-refractive (PTR) glass is an ideal photosensitive material for recording phase volume holograms. It is a homogeneous multi-component silicate glass that demonstrates all the advantages of optical glass: thermal stability, high laser damage threshold, and a wide transparency range. Moreover the ability to record phase patterns (i.e. spatial refractive index variations) into PTR glass has resulted in the fabrication of volume holograms with diffraction efficiency greater than 99%. The conventional method of recording a hologram in PTR glass relies on exposure to continuous-wave ultraviolet laser radiation.

In this dissertation the interaction between infrared ultrashort laser pulses and PTR glass is studied. It is shown that photosensitivity in PTR glass can be extended from the UV region to longer wavelengths (near-infrared) by exposure to ultrashort laser pulses. It is found that there exists a focusing geometry and laser pulse intensity interval for which photoionization and refractive index change in PTR glass after thermal development occur without laser-induced optical damage. Photoionization of PTR glass by IR ultrashort laser pulses is explained in terms of strong electric field ionization. This phenomenon is used to fabricate phase optical elements in PTR glass.

The interaction between ultrashort laser pulses and volume holograms in PTR glass is studied in two laser intensity regimes. At intensities below ~10^{12} W/cm^2 properties such as diffraction efficiency, angular divergence, selectivity, and pulse front tilt are shown to agree with the theory of linear diffraction for broad spectral width lasers. A volume grating pair arrangement is shown to correct the laser pulse distortions arising from pulse front tilt and angular divergence. At higher intensities of irradiation, nonlinear generation and diffraction of third harmonic is observed for three types of interactions: sum-frequency generation, front-surface THG generation, and THG due to phase-matching with a grating formed by modulation of the nonlinear refractive index of PTR glass.

Selle väitekirja pühendan oma emale ja isale, kes on mind kõigi nende aastate jooksul piiritult armastanud, toetanud ja julgustanud.

ACKNOWLEDGMENTS

I would like to thank my advisor Dr. Leonid B. Glebov for providing an ideal environment to conduct scientific research. His enthusiasm for science and historical perspective are qualities that I will embrace in my future career as a scientist.

I thank my advisory committee members, Dr. Boris Ya. Zeldovich, Dr. Michael Bass, Dr. David J. Hagan, and Dr. Alfons Schulte for their constructive remarks on my thesis work and for sharing their expertise and knowledge in optics.

I thank Julien Lumeau for supervising my research and pushing me to become a better scientist. *Mon ami, la prochaine fois que l'on se voit en France, on se fait une bouffe*.

I also want to thank my first supervisor, now Director of Holography and Diffractive Optics at Optigrate, Vadim Smirnov. His imaginative ideas are always interesting to consider.

The PPL group at CREOL was vital for my research success. Just before my first conference presentation I still had not finished all my experiments and Larissa Glebova offered to work on the weekend to prepare new glass samples. Thank you Larissa, you've always been ready to help and bail me out whenever my experiments went wrong. I'm also grateful to Ina Ciapurina and Irina Popkova for glass sample preparation. Ina, I feel that it is now safe to confess that I broke more than half of the thin, less than 200 μm thick, glass samples you prepared for me. I also want to apologize to Igor Ciapurin and Nikolai Vorobiev for constantly turning off the lights and keeping the lab in darkness. In retrospect I should have invested a little money in an IR card. I think I understand now why Igor always wanted to chat for hours. Thanks

for all the enlightening conversations we had in room 249. I am thankful to George Venus and Armen Sevian for giving me a hard time during group meetings. I am also thankful to Vasile Rotar for fabrication of volume Bragg gratings. Overall I wish to express my sincere appreciation to all members of the PPL team, past and present. Their hard work helped support my research activities. Большое спасибо!

An unexpected pleasure during my Ph.D. work was to take part in a six-month research stay at the University of Bordeaux 1, France. I acknowledge the National Science Foundation's financial support through IMI-NFG. I want to thank Laurent Sarger for inviting me to France and Lionel Canioni for hosting me in his research group. Additional thanks to Laurent for loaning me a bicycle with a rusty chain.

Pursuing my Ph.D. degree at CREOL has been a privilege. Even when my lab didn't have the necessary equipment to make an experiment there was someone in CREOL who did. First of all I thank Richard Zotti for his expertise in building scientific apparatus and teaching me how to use machine tools. I wish to thank Dr. George Stegeman and his students Sergiy Suntsov and Georgios Siviloglou for letting me use their OPA system. I am grateful to Dr. Stephen Kuebler and his student Toufic Jabbour for allowing me to use their FROG system.

Finally, in addition to the friends already mentioned, I am particularly grateful to have met Troy Anderson, Oleksiy Andrusyak, Dave Haefner, Jeff Hunker, Mario Leiria, Chris Middlebrook, Sergiy Mokhov, Eugene Rotari, Arnaud Royon, and Grady Webb-Wood during the past five years at CREOL. It has been a worthwhile experience and I will miss the people at CREOL very much.

TABLE OF CONTENTS

LIST OF NOMENCLATURE

$\hbar$	Planck’s constant (6.582×10^{-16} eV·sec)
c	Speed of light in free space (2.998×10^{8} m·sec^{-1})
m_e	Electron rest mass (9.1095×10^{-31} kg)
e	Electron charge (1.602×10^{-19} C)
ε_0	Permittivity of free space (8.854×10^{-12} F·m^{-1})
μ_0	Permeability of free space ($4\pi \times 10^{-7}$ H·m^{-1})
k_B	Boltzmann’s constant (8.617×10^{-5} eV·K^{-1})
eV	Electron volt (1.602×10^{-19} J)
α	Decimal absorption coefficient
D	Dosage
Δn	Change in refractive index
E	Electric field
E	Energy
E_g	Band gap energy
I	Intensity
λ	Wavelength
Λ	Grating spatial period
n_0	Linear refractive index
n_2	Nonlinear refractive index
ω	Angular frequency
x, y, z	Position coordinates
mJ	Millijoule (10^{-6} J)
mrad	Milliradian (10^{-3} rad)
msec	Millisecond (10^{-3} sec)
nsec	Nanosecond (10^{-9} sec)
psec	Picosecond (10^{-12} sec)
fsec	Femtosecond (10^{-15} sec)
kHz	Kilohertz (10^{3} Hz)
MHz	Megahertz (10^{6} Hz)
cm	Centimeter (10^{-2} m)
mm	Millimeter (10^{-3} m)
µm	Micrometer (10^{-6} m)
nm	Nanometer (10^{-9} m)
pm	Picometer (10^{-12} m)
MW	Megawatt (10^{6} W)
GW	Gigawatt (10^{9} W)
TW	Terawatt (10^{12} W)

CPA	Chirped pulse amplification
cw	Continuous wave
He-Cd	Helium-Cadmium
He-Ne	Helium-Neon
HOE	Holographic optical element
$HWe^{-2}M$	Half width at e^{-2} of intensity maximum
IR	Infrared
PFT	Pulse front tilt
ppm	Parts per million
PTR	Photo-thermo-refractive
SFG	Sum frequency generation
RBG	Reflecting Bragg grating
SI	Spectral interferometry
TBG	Transmitting Bragg grating
THG	Third harmonic geneation
UV	Ultraviolet

LIST OF FIGURES

LIST OF TABLES

CHAPTER ONE: INTRODUCTION

Conventional optical devices such as lenses, mirrors, and prisms work by refracting or reflecting light. A simple geometrical ray optics approach is often sufficient to predict the behavior of light by these elements. But light has a wave nature and optical elements can be made based on the diffraction of light. A diffraction grating is an example of such an element where the laws of geometrical optics no longer apply (the angle of reflection is not necessarily equal to the angle of incidence). With the advent of holography an even more complex class of optical elements has emerged; holographic optical elements. These are elements which use diffraction to manipulate the characteristics of light waves. HOEs can exhibit remarkable properties such as narrowband filtering and almost 100% energy coupling into a single diffracted order. But success of any optical element depends critically on using the right material. It is possible that Galileo disregarded the existence of nebulae (starless clouds composed of gas and dust that appear hazy) because he thought a better quality telescope (the lenses in his telescope were filled with tiny bubbles, colored by a greenish tint, and an irregular lens shape gave poor focus near the periphery) would always resolve nebulae into clusters of distant stars. Newton asserted that an achromatic lens was unattainable because he believed all transparent materials have the same refractive index. In modern times the need to understand the material properties of optical elements has been reinvigorated by the invention of the laser. High-energy laser applications require optical materials that can handle extreme temperatures, severe environmental conditions, and laser-induced damage. A new material for HOE design, photo-thermo-refractive (PTR) glass, has recently shown great success in satisfying these criteria. This thesis deals with new phenomena related to the interaction between high-power ultrashort laser pulses and PTR glass. To establish the general context of the thesis work we will first survey important background information.

1.1 Holography

Holography was invented by Dennis Gabor in 1948 as way of recording the phase information of electromagnetic waves [1]. The traditional way of recording the information content of light waves, i.e. photography, only obtains amplitude information. Phase information is lost. This is why a photographic image appears two-dimensional. Holograms are able to reconstruct a three-dimensional image because they contain both amplitude and phase information. Gabor recorded the first hologram by interfering two coherent light waves (an object wave and a reference wave) on a photographic plate. When the processed plate was illuminated by the reference wave alone the original object wave reappeared. The reconstructed object wave contained both amplitude and phase information. This method of holography requires light waves that exhibit both spatial and temporal coherence. Gabor's original experiments used light from a high-pressure mercury lamp which had a coherence length of only 100 μm. Further development in holography required longer coherence lengths and occurred only after the introduction of the laser in 1960 [2] and the helium-neon laser (1962) in particular [3]. Leith and Upatnieks first applied the laser to holography and improved the recording technique by introducing off-axis recording [4]. This technique allowed them to separate the object wave from the reference wave during reconstruction. Denisyuk introduced a scheme for recording three-dimensional holograms [5] and van Heerden showed that the maximum data storage capacity of three-dimensional holograms would be one bit per λ^3 [6]. At present time the Blu-ray optical disc (120 mm diameter, 1.2 mm thickness) can hold 50 GB of data giving it a data capacity of

3×10^{10} bits/cm^3. Utilizing the blue laser wavelength of 405 nm for holographic recording could theoretically allow 1.5×10^{13} bits/cm^3, a 500× improvement over current technology. In the early days of holography photosensitive materials were not considered to be three-dimensional media because their thickness was smaller than the finest detail of the recorded diffraction pattern. But thick photographic emulsions soon appeared. Thick (called volume) holograms obey a diffraction process analogous to that of Bragg diffraction by crystals. A crystal can be considered to behave like a three-dimensional grating when irradiated by X-rays. W.H. Bragg and W.L. Bragg showed that diffraction of X-rays from crystals depends on both the wavelength of radiation as well as the angle of incidence [7]. This dependence is given by the famous Bragg equation

$$m\lambda = 2\Lambda \sin\theta, \tag{1.1}$$

where m is an integer, λ is the wavelength of electromagnetic radiation, Λ is the spatial period of diffracting planes, and θ is the angle of incidence. Diffraction of optical waves by volume holograms also depends on the wavelength and incident angle used for reconstruction. This dependency is called spectral and angular selectivity, respectively. In 1969 Herwig Kogelnik analyzed Bragg diffraction of light by thick hologram gratings using coupled-wave theory [8]. His analysis showed that volume phase gratings can theoretically couple 100% of the incident radiation energy into the diffracted order. Thus a comprehensive theoretical understanding of holographic optical elements was in place by the late 1960s. However no material at the time satisfied all the requirements of an ideal holographic medium.

1.2 Photographic Emulsion

The first photosensitive material used in holography was silver-halide emulsion. The history of using silver-halide crystals for photosensitivity dates back to the beginning of photography when

Niépce and Daguerre experimented with processes for preserving images. A typical photographic emulsion consists of small silver halide crystals (“grains”) embedded in a protective matrix (usually gelatin). Silver-halide crystals are cubical in shape and each positively charged silver ion (Ag^+) is surrounded by negatively charged halide ions. The most common silver-halide crystals are silver bromide (Ag^+Br^-), silver chloride (Ag^+Cl^-), and silver iodide (Ag^+I^-). We will use the general designation Ag^+X^- for any silver halide crystal. The photographic process is a two-step process. First, the silver halide emulsion is exposed to light. During exposure the silver halide crystals undergo an invisible change called latent image formation represented by the reaction

$$\mathrm{Ag^+X^-} \xrightarrow{\hbar\omega} \mathrm{Ag^+X^0} + e, \tag{1.2}$$

where e is a free electron and X^0 can be considered to be a hole. Diffusion and trapping of electrons and/or holes causes metallic silver (Ag^0) to form. In the Gurney-Mott theory it is trapping of free electrons which lead to Ag^0 formation [9]. In Mitchell’s theory trapping of holes is believed to cause Ag^0 formation [10]. In any case trapping of electrons and/or holes is essential. These traps are associated with defect sites in the lattice. It has been shown that pure silver-halide crystals without defects are actually *insensitive* to light [11]. A latent image requires at least a few silver atoms at one site to be developable. At this stage there is no noticeable change (i.e. no significant absorption or refractive index change has occurred). This first step involving silver-halide exposure to light is called latent image formation. In order to develop the neutral silver atoms into a visible change a second step is required. Chemical development of the latent image converts the silver atoms to non-sensitive metallic silver. Absorption by metallic silver generates the visible change seen in a photograph (which in the case we described is a negative image). It is important to emphasize the astonishing photosensitivity of silver-halide crystals. A single silver ion has a diameter of about 0.23 nm. For a silver-halide grain size of 35 nm there will be about 4×10^6 silver ions present. It is generally agreed that at least four absorbed photons create a developable silver speck. After chemical development the entire grain is converted to metallic silver atoms. Thus four photons lead to a process which eventually creates 4×10^6 metallic silver atoms, an amplification of 10^6. Conventional high-speed photographic film can have amplification greater than 10^9! In addition to photographic emulsion as a photosensitive material used in holography dichromated gelatin has also found success. However both photographic emulsion and dichromated gelatin use photosensitive agents embedded in a gelatin matrix. Gelatin is an organic substance with weak laser energy tolerance. For high-power laser applications the only optical materials with suitable energy handling capabilities are inorganic solids (i.e. crystals and glasses).

1.3 Photorefractive Crystals

In 1966 Ashkin et al. observed changes in refractive index in lithium niobate ($LiNbO_3$) and other ferroelectric crystals due to intense exposure to light [12]. Light exposure causes excitation of charge carriers which migrate until trapped at new locations within the crystal. Exposure to an interference pattern of light generates a distribution of charges whose concentration follows the gradient distribution of the interference pattern. The trapped charges then create an electric space charge field that changes the local refractive index via the electro-optic effect. The most widely used model for explaining photorefractive phenomena that includes the rate equations for free carriers and impurity densities, the current equation, and Poisson’s equation was introduced by Kukhtarev in 1979 [13]. Photorefractive crystals are advantageous for holography because holograms can be recorded and erased. However the disadvantages of photorefractive crystals include poor sensitivity and the fact that the stored hologram is temporary (during reconstruction the hologram is partially erased).

1.4 Photosensitive Glasses

In the late 1940s S.D. Stookey at Corning introduced a new medium for photography, photosensitive glass [14]. This was an alkali metal-alkaline earth-silicate glass doped with a photosensitive agent (e.g silver, gold, or copper), an optical sensitizer (e.g. cerium), and thermoreducing agents (typically tin and antimony). Stookey applied the two-step photographic process to photosensitive glass. First, exposure is done using ultraviolet radiation to produce ionization of cerium ions. The released electrons are trapped by silver ions, Ag^+, converting them to neutral silver, Ag^0. The reaction is given by

$$Ag^+ + Ce^{+3} \xrightarrow{\hbar\omega} Ag^0 + Ce^{+4}. \tag{1.3}$$

This stage corresponds to latent image formation and no significant change in absorption or refractive index occurs. The second step is to develop the latent image into an observable change. In the photographic process chemical development is used. With photosensitive glass Stookey used heat treatment. By heating the glass to temperatures at or above its annealing temperature submicroscopic metal particles begin to precipitate in the areas that were irradiated during exposure. Light scattering and absorption by these particles causes a visible picture to be formed in the glass. Researchers at Corning later discovered that precipitation of microscopic nonmetallic crystals can also be used to make translucent or opaque images in photosensitive glass [15]. The next significant development came in 1985 by Borrelli and coworkers when they discovered that a refractive index change also occurs during the photosensitive process [16]. A sodium fluoride microcrystalline phase in photosensitive glass decreases the local refractive index because of a mismatch between the refractive index of NaF crystals and the surrounding glass matrix. A phase optical pattern was demonstrated. However, the glass still showed losses (absorption and/or scattering) after thermal development (i.e. a red color was observed in the exposed areas). A more complex phase pattern (a hologram) was demonstrated in photosensitive glass by Glebov and coworkers in 1989 at the Vavilov State Optical Institute in St. Petersburg, Russia [17]. However, scattering was a problem and absolute transmission efficiency of the optical element was limited to less than 50%. Further improvements were not achieved until the late 1990s when Glebov and coworkers at CREOL, the University of Central Florida were able for the first time to make pure and homogenous photosensitive glass and demonstrate optical elements with absolute losses less than 5% [18-20]. Because the coloration property of photosensitive glass was no longer utilized, only its ability to change refractive index, this new glass was named photo-thermo-refractive glass.

1.5 Photo-Thermo-Refractive Glass

PTR glass is a highly homogeneous and transparent sodium-zinc-aluminum-silicate glass doped with silver, cerium, fluorine, and bromine. Table 1.1 summarizes the various elemental components found in a typical sample of PTR glass and their respective functions. PTR glass is a crown-type optical glass characterized by having a refractive index at 587.5 nm equal to 1.4959 and an Abbe number of 59.2. Linear photosensitivity is determined by photoexcitation of Ce^{3+} ions. Typically near ultraviolet radiation is used for exposure. The electrons that are released from cerium are trapped by silver ions to form neutral silver. Thermal development at temperatures in the range 450-500°C leads to diffusion of silver atoms and formation of silver containing particles. These particles serve as nucleation centers for sodium fluoride crystal growth at temperatures between 500 and 550°C. After this final step a refractive index change of up to 10^{-3} occurs between exposed and unexposed areas in the glass.

Table 1.1. Typical PTR glass composition. Adapted from Ref. [15].

Glass component	mol.%	Function
SiO_2	72.3	Glass matrix
Na_2O	13.6	
ZnO	5.2	
Al_2O_3	2.3	
NaF	3.7	Nanocrystal constituents
AlF_3	1.3	
Ag_2O	0.01	Photosensitive agents, optical sensitizer
KBr	1.5	
CeO_2	0.01	
Sb_2O_3	0.03	Thermal sensitizers, redox agents, refining agents
SnO_2	0.02	

The refractive index change is actually a decrement because NaF crystals have a lower index value than the surrounding glass. However because the volume fraction of NaF is limited the maximum refractive index decrease amounts to 10^{-3}. The photo-thermo-refractive process in PTR glass is shown in Figure 1.1 using the energy level diagram to illustrate the respective processes occurring during laser exposure and thermal development. It is also important to see the effect of cerium on the absorption spectra of PTR glass, Figure 1.2. For linear photosensitivity it was necessary to introduce cerium since the band gap of PTR glass is placed at about 5.8 eV (212 nm). An absorption band peak characteristic of Ce^{3+} ions is located at about 4 eV (305 nm). A Helium-Cadmium laser operating at 3.8 eV (325 nm) will photoionize PTR glass via linear absorption. Figure 1.3 shows how the refractive index changes in PTR after exposure to cw laser light from a He-Cd laser and thermal development for one hour at 515ºC.

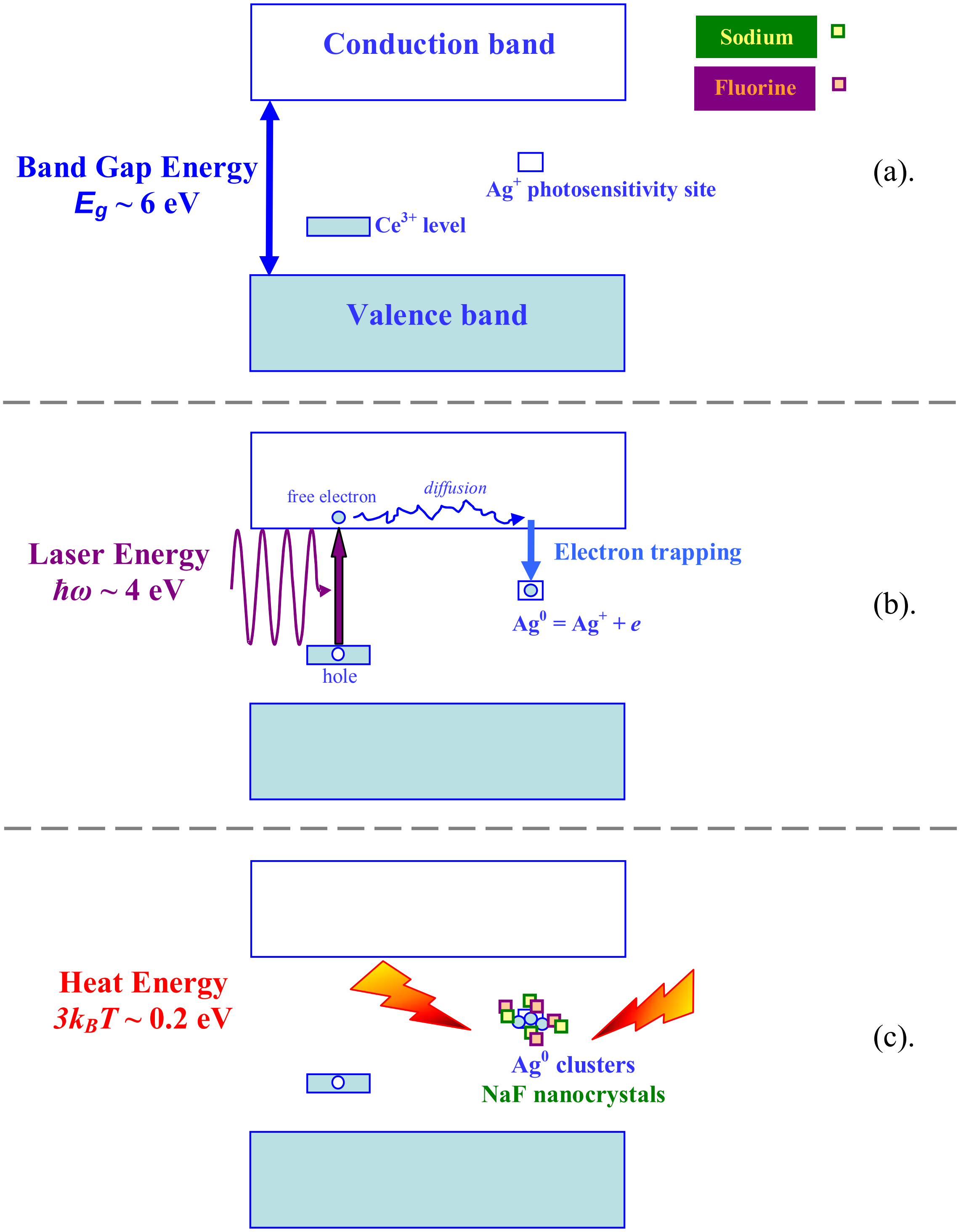

Figure 1.1. Process of linear photosensitivity in PTR glass: (a) Energy-level diagram for PTR glass (b) exposure to ionizing radiation (c) thermal development.

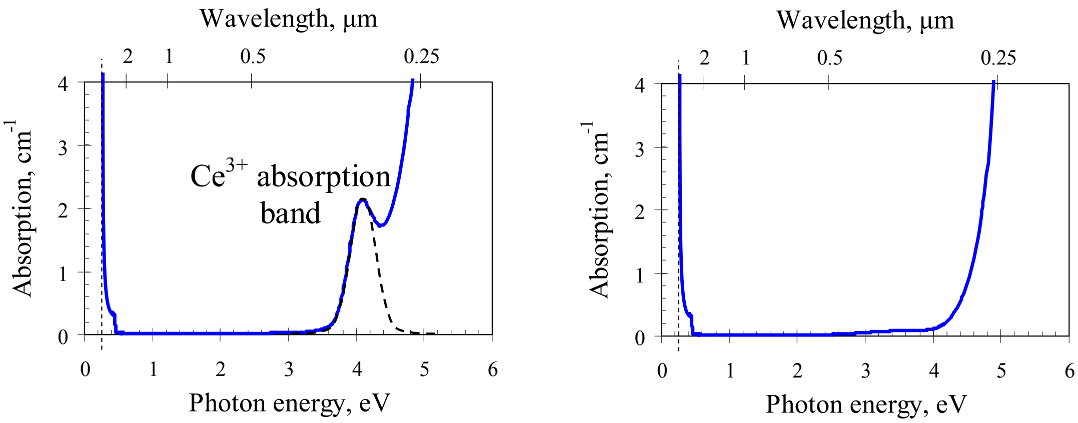

(a).

(b).

Figure 1.2. Absorption spectra of PTR glass: (a) Ce-doped (b) Ce-free.

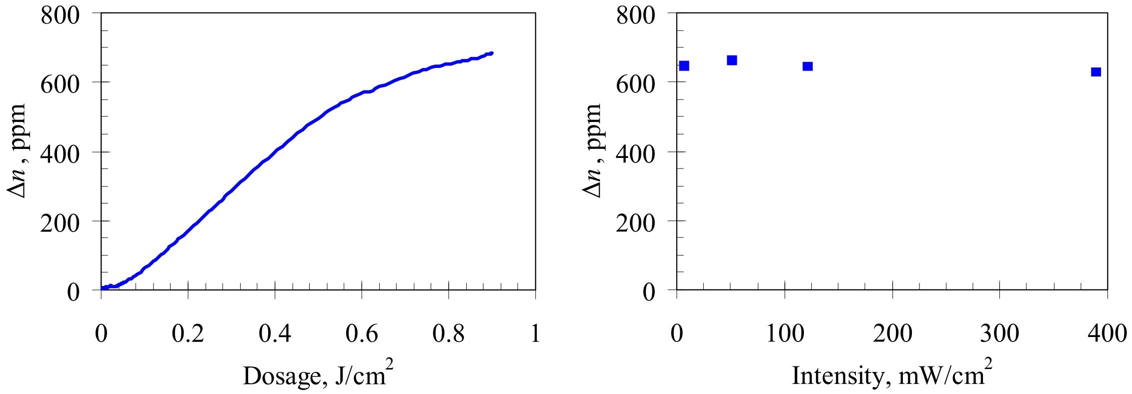

(a).

(b).

Figure 1.3. Linear photosensitivity of PTR glass. Exposure to He-Cd laser and thermal development for one hour at 515ºC.

By accurately controlling the refractive index change in PTR glass it has been possible to fabricate volume Bragg gratings. The conventional fabrication procedure is to holographically interfere light from a He-Cd laser through a PTR glass sample. After exposure the glass sample is thermally developed to achieve the correct refractive index modulation for a desired value of diffraction efficiency. PTR glass volume Bragg gratings can have absolute diffraction efficiency greater than 95% and relative diffractive efficiency above 99.9%. Volume Bragg gratings are advantageous because of their selectivity properties. A RBG in PTR glass can have spectral selectivity as small as 10 pm (FWHM). This permits one to use RBGs for spectral filtering. High brightness semiconductor laser operation using a RBG in PTR glass for spectral narrowing has been demonstrated [21]. In addition to spectral selectivity volume Bragg gratings exhibit angular selectivity. A TBG in PTR glass can have angular selectivity as small as 0.1 mrad (FWHM). Angular filtering is useful when one considers that different transverse modes in a laser resonator travel at different angles with respect to the optical axis. It has been shown that TBGs in PTR glass provide selection of a single transverse mode from a wide stripe laser diode [22]. When incident laser light on a volume Bragg condition does not satisfy the Bragg condition the grating will not diffract the light and thus the incident light is transmitted through the grating. Diffraction depends on the specific conditions of detuning from Bragg condition but usually there are nulls where diffraction efficiency is zero. Therefore two laser beams incident on a volume Bragg grating (one beam satisfying Bragg condition and the other beam slightly detuned in wavelength to satisfy a null condition) can be combined into a single beam. This approach to spectral beam combining has been tested with both RBGs and TBGs. Use of RBGs in PTR glass resulted in five-channel combining with maximum output power greater than 750 W and overall combining efficiency greater than 90% [23]. A major advantage of PTR glass diffractive optical elements is that they are able to withstand high temperatures. The photo-induced refractive index change is stable up to ~400°C and is determined by the glass transition temperature of PTR glass (450°C) not by the melting temperature of the nanocrystals (1000°C). Also, absorption in PTR glass is very low (a few 10^{-4} cm^{-1} at 1 μm). The result is that PTR glass elements are resistant to high-energy laser irradiation and can be used as low less elements in high-power laser systems. Transparent glass-ceramics are also known to have better thermal stability and strength than pure glass [24]. To effectively manage thermal effects in glass optical elements it is apparent that an embedded crystalline phase inside the glass matrix is advantageous.

1.6 Nonlinear Optics

The first nonlinear optical experiments were done using pulsed lasers. In continuous-wave operation lasers do not usually reach their maximum potential for energy extraction from the gain medium. Lasing is based on population inversion (more electrons in an upper energy level than a lower one) and stimulated emission of the upper level electrons to the lower level. When the upper laser level lifetime is longer than the gain buildup time for stimulated emission then population inversion does not reach the maximum possible value allowed by the system. Q-switching was proposed by Hellwarth in 1961 as a way of operating a laser with highest possible gain extraction [25]. The method uses a shutter to prevent laser cavity oscillation and thereby allows the population inversion to grow to large values. When the shutter is suddenly opened, stimulated emission quickly extracts the stored energy, and a "giant pulse" of laser output results. The pulse durations are determined by the cavity decay time and are typically on the order of 10 nsec. To obtain shorter pulse durations the technique of mode-locking was proposed. The method requires that the longitudinal modes of a laser combine in such a way that each mode exhibits phase coherence with the others. In this case pulses are generated with durations equal to the inverse of the laser gain bandwidth. Oftentimes mode-locked pulses are generated from an oscillator that generates only low energy pulses. In order to amplify these pulses special care must be taken. The technique of chirped pulse amplification was invented to solve the problem of short amplified pulses damaging the laser gain media [26]. With CPA a mode-locked pulse is first temporally stretched before going to the amplifier. After amplification the pulse is recompressed. Typically grating arrangements are employed for stretching and compressing [27].

Nonlinear optical effects are the result of high-intensity electric field interaction with matter. The following discussion makes use of reference material found in the textbook Nonlinear Optics by R.W. Boyd [28]. In linear optics the simplest way to understand how laser light interacts with matter is by using the classical dipole oscillator model developed originally by H.A. Lorentz [29]. Basically matter is considered to be a collection of individual dipole oscillators. Each dipole consists of an electron attached to the atom by a binding force. In the linear approximation the restoring force varies linearly with displacement of the electron from equilibrium. However in the case of strong electric fields the displacements will be large and the linear approximation is no longer valid. Nonlinear processes can be described by rewriting the polarization response of matter to include higher order terms

$$\begin{aligned}\mathbf{P} &= \varepsilon_0\boldsymbol{\chi}^{(1)}\mathbf{E} + \varepsilon_0\boldsymbol{\chi}^{(2)}\mathbf{EE} + \varepsilon_0\boldsymbol{\chi}^{(3)}\mathbf{EEE} + \cdots \\ &= \mathbf{P}^{(1)} + \mathbf{P}^{(2)} + \mathbf{P}^{(3)} + \cdots.\end{aligned} \tag{1.4}$$

Isotropic matter, such as glass, possesses inversion symmetry and consequently the second-order susceptibility $\boldsymbol{\chi}^{(2)}$ is equal to zero. Our focus will be on the effects of $\boldsymbol{\chi}^{(3)}$. Let us consider the simple case where the driving electric field is given by

$$E(t) = E_0 \cos \omega t. \tag{1.5}$$

Solving for the nonlinear polarization results in

$$\begin{aligned}P^{(3)}(t) &= \varepsilon_0 \chi^{(3)} E(\mathrm{t})^3 \\ &= \frac{3}{4}\varepsilon_0 \chi^{(3)} E_0^3 \cos \omega t + \frac{1}{4}\varepsilon_0 \chi^{(3)} E_0^3 \cos 3\omega t.\end{aligned} \tag{1.6}$$

It is seen in Equation 1.6 that the nonlinear response of the material to a driving electric field of frequency ω has two terms, one oscillating at frequency ω and the other at 3ω. The term oscillating at 3ω is responsible for the nonlinear effect of third-harmonic generation. To study another important third-order nonlinearity we switch to the frequency domain representation and consider one of the electric field components to be complex conjugated. We then have

$$\begin{aligned} P(\omega) &= \varepsilon_0\chi^{(1)}E(\omega) + 3\varepsilon_0\chi^{(3)}(\omega=\omega-\omega+\omega)E(\omega)E^*(\omega)E(\omega) \\ &= \varepsilon_0\left[\chi^{(1)} + \frac{3}{2n_0\varepsilon_0 c}\chi^{(3)}I\right]E(\omega) = \varepsilon_0\chi_{eff}E(\omega) \end{aligned} \tag{1.7}$$

where we have written the intensity of light as

$$I = 2n_0\varepsilon_0 c\, E(\omega)E^*(\omega). \tag{1.8}$$

The refractive index is written in general as

$$n = \sqrt{1+\chi_{eff}}\,. \tag{1.9}$$

From Equation 1.7 we have an expression for χ_{eff}, the linear refractive index n_0 is given by $n_0 = (1+\chi^{(1)})^{1/2}$, and making the approximation $(1+x)^{1/2} \approx 1+x/2$ which is valid for $x < 1$ we obtain

$$\begin{aligned} n &= \sqrt{n_0^2 + \frac{3}{2n_0\varepsilon_0 c}\chi^{(3)}I} \\ &= n_0\sqrt{1+\frac{3}{2n_0^3\varepsilon_0 c}\chi^{(3)}I} \\ &= n_0 + \frac{3}{4n_0^2\varepsilon_0 c}\chi^{(3)}I = n_0 + n_2 I, \end{aligned} \tag{1.10}$$

where in the last line we introduce a new constant n_2 called the intensity-dependent refractive index. The result is that the refractive index of the medium is no longer constant but depends on the intensity of the excitation source. The intensity-dependent refractive index is responsible for several nonlinear effects such as self-focusing and supercontinuum generation.

1.7 Ultrashort Laser Pulse Interaction with Matter

The influence of high-intensity electric fields on an atomic system can lead to dissociation of electrons from nuclei. When a gas is exposed to high-power focused laser pulses the light is absorbed by multiphoton ionization and inverse bremsstrahlung resulting in the formation of an expanding electron/ion cloud, i.e. plasma. Typical electron plasma temperatures are several electron volts. Some characteristics of plasmas include white-light emission, sparks due to recombination of electrons and ions, and a pressure wave. The first demonstration of laser-induced damage in a transparent solid was reported by Hercher in 1964 [30]. A glass sample was irradiated by Q-switched, multi-mode nanosecond laser pulses and filamentary damage tracks were observed. The mechanism responsible for laser-induced damage in transparent dielectrics was proposed by Bloembergen et al. to be electron avalanche breakdown [31]. However, results by other researchers produced experimental data inconsistent with a model based on intrinsic avalanche breakdown [32-36]. Jones et al. have proposed a model of laser-induced damage based on phonon heating [36]. Important results dealing with femtosecond laser pulse interaction with transparent solids came in 1996 by three groups: an American group at Harvard University [37], a Japanese group at Kyoto University [38], and a German group from the University of Essen [39]. The American group showed that tightly focused femtosecond pulses can damage only a localized area within the glass. The Japanese group showed that a positive refractive index change occurs due to this type of damage and a waveguide optical element was demonstrated. In contrast to first two groups the German group reported a remarkable resistance of transparent dielectrics to femtosecond laser-induced optical breakdown. They were unable to cause damage in the bulk of fused silica glass with femtosecond pulses focused from a low numerical aperture lens. Moreover they also offered a tentative explanation in terms of self-defocusing due to a negative refractive index change that accompanies the developing plasma. The next decade saw tremendous growth in micromachining of glass with tightly focused femtosecond laser pulses. However progress was limited with low numerical aperture lens focusing of femtosecond pulses.

The reason being that optical breakdown was thought to be the only way to generate a refractive index change in glass by ultrashort laser pulse exposure.

1.8 Thesis Outline

The first part of this thesis reports on a new approach for fabricating phase optical elements in PTR glass. Instead of direct writing by ultrashort laser pulse exposure it is shown that nonlinear ionization in PTR glass can occur at intensities below the damage threshold. The photo-thermo-refractive process is used to generate a change in refractive index. Nonlinear ionization allows the wavelength regime of photosensitivity in PTR glass to be extended to longer wavelengths. Chapter 2 discusses characterization of nonlinear photosensitivity in PTR glass and Chapter 3 describes the nonlinear ionization mechanisms. To demonstrate practical utility of nonlinear photosensitivity Chapter 4 discusses the recording and testing of phase optical elements.

The second part of the thesis deals with the interaction between ultrashort laser pulses and volume Bragg gratings in PTR glass. Two intensity regimes are studied. Chapter 5 shows that at intensities below $\sim 10^{12}$ W/cm^2 properties such as diffraction efficiency, angular dispersion, selectivity, and pulse front tilt agree with classical linear diffraction theory for broad spectral width lasers. Chapter 6 shows that at higher intensities nonlinear generation and diffraction of the third harmonic occurs. Three separate THG conditions are described and explained theoretically.

Chapter 7 summarizes the results of the thesis and presents an outlook for the future.

CHAPTER TWO: NONLINEAR PHOTOSENSITIVITY OF PTR GLASS

It would be beneficial to have photosensitivity in PTR glass at wavelengths longer than the linear photosensitivity limit (~350 nm, 3.5 eV). This would permit one to record complex holograms in PTR glass for applications in the visible and near-infrared spectral regions. Since a linear photoionization process is not possible (the glass is transparent in the visible and near-infrared) the approach is to use nonlinear effects from high-intensity laser pulses to obtain photosensitivity. To begin let us consider the general problem of shifting photosensitivity to longer wavelengths.

2.1 Shifting PTR Glass Photosensitivity to Longer Wavelengths

The linear photosensitivity limit of a photosensitive material is determined by its absorption edge. In PTR glass the absorption edge of the glass matrix is placed at about 5.8 eV (212 nm) [40]. However, the absorption edge can shifted to longer wavelengths by adding dopants or impurities. In this case the effective absorption edge of the glass no longer corresponds to the intrinsic (band gap) absorption edge. Figure 2.1(a) illustrates how doping with cerium shifts the absorption edge of PTR glass to 3.5 eV (350 nm) and allows commercially available lasers (e.g. He-Cd laser at 3.8 eV, 325 nm) to be used for linear photosensitivity. A similar effect can be observed in soda-lime glass by the addition of iron impurities, Figure 2.1(b). Soda-lime glass ($22NaCa{\cdot}3CaO{\cdot}75SiO_2$) is the most widely available glass on the market. It is used for windowpanes, light bulbs, vessels, ornaments, etc. In commercial production the most cost effective method for producing soda-lime glass results in the presence of iron impurities. A thick piece of commercial soda-lime glass will show a greenish tint due to absorption by iron impurities. Thus in order to study the intrinsic absorption band of alkali-silicate glasses it is important to melt soda-lime glass with a minimal concentration of iron impurities (less than a few ppm). The mistake of assuming the band gap edge of soda-lime glass to be at 4 eV (300 nm) still exists today in scientific literature [41]. In 1963 Smith and Cohen showed that the band gap edge of alkali-silicate glasses is around 5.6 eV (221 nm) [42].

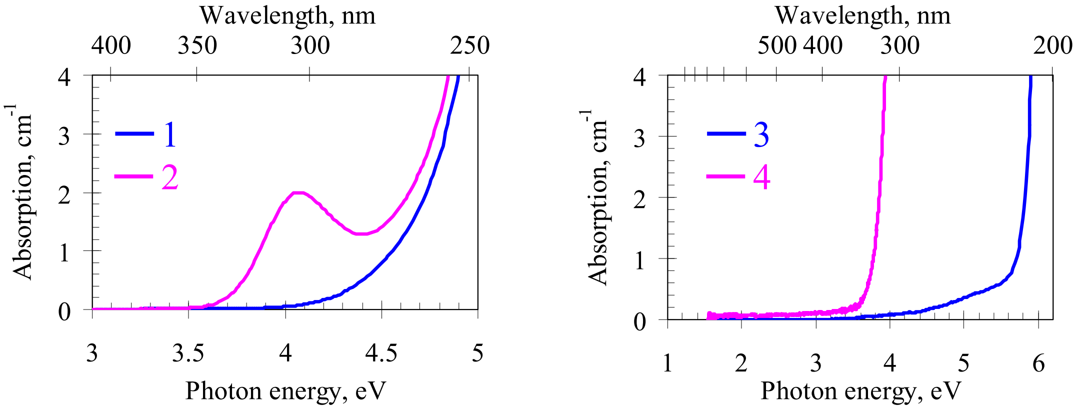

(a). (b).

Figure 2.1. Affect of dopants and impurities on the absorption spectra of glass: (a) PTR glass 1 – without cerium 2 – with cerium (b) soda-lime glass 3 – high purity melt 4 – commercial melt.

For silicate glasses the band gap edge is in the ultraviolet region and thus in the visible and infrared region these glasses are transparent. The intrinsic absorption of silicate glass in the infrared is very low. It was shown by Kapron et al. in 1970 that high-purity glass fibers can be fabricated with losses close to the theoretical limit [43]. Today loss by intrinsic absorption in fused silica fibers is no longer a problem. Instead the fundamental transmission limit is due to Rayleigh scattering which at 1550 nm attenuates light by 0.2 dB/km (losses equal to 2×10^{-7} cm^{-1}). For fabrication of bulk glass as opposed to glass fibers the intrinsic absorption limit has not yet been reached. Returning to the discussion of shifting photosensitivity to longer wavelengths Figure 2.1(a) showed that the dopant cerium in PTR glass shifts photosensitivity. This approach to shifting photosensitivity is called chemical sensitization. Dopants, however, introduce undesirable linear absorption at the wavelength of interest. The goal is to have long wavelength photosensitivity in PTR glass without sacrificing transparency. Thus another approach was considered in Ref. [44]. The idea was to use two-step illumination. First PTR glass is uniformly exposed with ultraviolet radiation to convert Ag^+ to Ag^0. Then a high-intensity long wavelength laser is used to bleach the Ag^0 centers back to their original valency of Ag^+. After thermal development the area exposed to the long wavelength laser will show smaller refractive index change than the surrounding area. A complex hologram in PTR glass was recorded and tested by this two-step process [45]. Pre-exposure was done by He-Cd laser light at 325 nm, dosage of 200 J/cm^2. Long-wavelength exposure was done by high-intensity nanosecond pulses at 532 nm (intensity at 250 MW/cm^2 and dosage of 10 kJ/cm^2). The glass sample was thermally developed for three hours at 515°C. Testing of the complex hologram was performed using a collimated He-Ne laser at 543 nm. Figure 2.2 shows the results of testing.

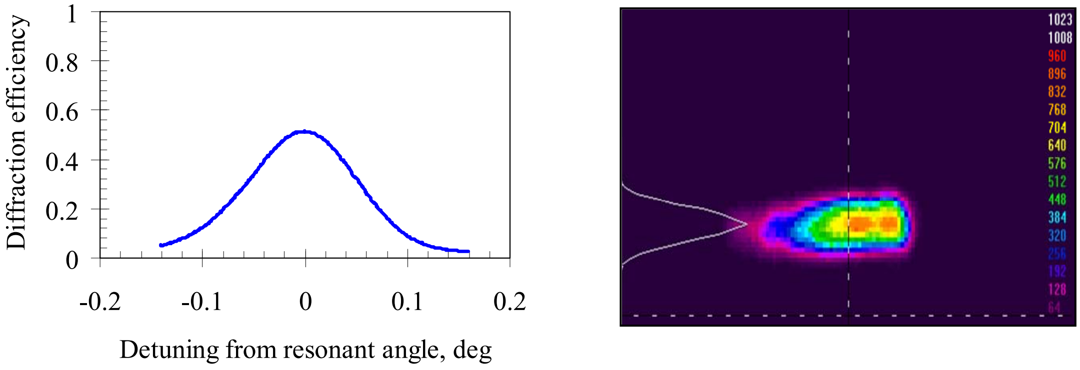

(a).

(b).

Figure 2.2. Reconstruction of a complex hologram (interference between focused beams) recorded in PTR glass by two-step illumination: (a) relative diffraction efficiency (b) spatial profile of diffracted beam. Hologram recording by focused nanosecond pulses at 532 nm. Hologram reconstructed by collimated He-Ne laser at 543 nm.

Figure 2.2(a) shows that the relative diffraction efficiency of the hologram reached 50% and Figure 2.2(b) illustrates that diffraction of a collimated beam has divergent properties proving that the recorded hologram behaved like a complex hologram. This two-step process relied on long-wavelength radiation to bleach Ag^0 in PTR glass back into Ag^+. Not all wavelengths are suitable for this interaction to occur. Moreover the efficiency of the process is low and the maximum achievable refractive index change is five to ten times smaller than that obtained by linear photosensitivity. Therefore a more general technique for shifting PTR glass photosensitivity to longer wavelengths is needed. The approach considered in this thesis consists of shifting photosensitivity in PTR glass to long-wavelengths by nonlinear ionization. The idea is that high-intensity laser pulses at long wavelengths (low energy photons) will photoionize PTR glass by multiphoton absorption or other nonlinear effects and subsequent thermal development will result in a photo-thermo-refractive induced change in refractive index. To prove this hypothesis we first study photoionization and then proceed to study refractive index change.

2.2 Photoionization in Glasses

Photoionization in condensed matter is the process whereby a photon excites an electron from the valence band into the conduction band. This interpretation of photoionization relies on the band theory of solids originally derived by Felix Bloch [46]. Bloch solved the Schrödinger equation assuming a periodic potential and arrived at solutions which predicted that the allowed energies for the electrons were divided into zones with gaps between them. An insulator is therefore a material that has a energy gap between a zone filled with electrons and an empty zone above it. These zones are called the valence and conduction bands respectively. In his theory Bloch assumed a periodic potential that is representative of the long-range symmetry found in crystalline solids. But can the concepts of band theory be applied to disordered solids for which long-range periodicity does not exist. Let us consider what happens to the energy levels of several individual atoms when they are brought closer and closer together. According to the exclusion principle more than two electrons cannot share the same orbital. Thus to accommodate several electrons the energy levels are split. In a solid the atoms are so close to each other that the splitting results in so many discrete levels that they form an essentially continuous range of energies which is called the energy band. This interpretation of how energy bands arise does not require the solid to have spatial periodicity and therefore energy bands can be expected to occur in disordered solids. Glass is a disordered solid. However the structure of glass is not purely random. There is a degree of order even though no long-range periodicity exists. Let us examine the length scales at which disorder exists in glass. We follow the approach of White [47] and partition the structure of a covalent glass into length scales described by Table 2.1.

Table 2.1. Length scales of structural order in covalent glass.

Length Scale, nm	Structure	Building Block
0.3-0.4	Short range order	Network polyhedron
0.5-1.5	Medium range order	Basic structural unit
1.2-10	Nanostructure	Clustered unit
> 10	Microstructure	Bulk glass

At small scales the forces between atoms in glasses and crystals are essentially the same and therefore a glass exhibits what is called short-range order. The actual difference between glasses and crystals begins when the length scale increases to beyond nearest atomic neighbors and the periodicity of a crystal is no longer present in a glass. Zachariasen formulated a continuous random network model for glass in which the fundamental short-range units for silicate glass are SiO_4 tetrahedra linked randomly over the long-range [48]. The repeating tetrahedral configuration ensures charge neutrality since each O^{-2} ion is shared by two Si^{+4} ions. This arrangement of a Si^{+4} ion bonded to four O^{-2} ions is termed fourfold coordination. Figure 2.3 illustrates the crystalline and non-crystalline bonding in SiO_2 using the fundamental tetrahedral building blocks.

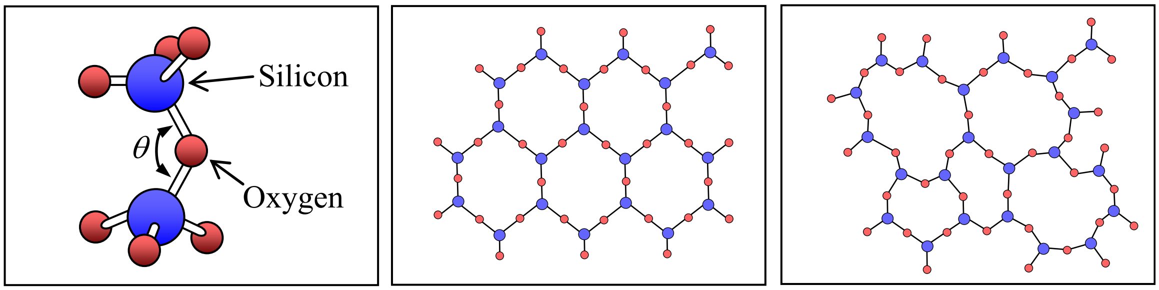

(a). (b). (c).

Figure 2.3. Structural bonding of SiO_2: three-dimensional view of (a) fundamental tetrahedral units; two-dimensional view of (b) regular arrangement in crystal (c) disordered arrangement in glass.

Now let us ask how an energy band gap can arise in glass. In fact let us frame the question the way Mott did in his 1977 Nobel lecture when he asked “how can glass be transparent?” [49]. Because Bloch’s theorem is only valid for a periodic potential we cannot use it to justify a band gap in glass. In 1958 Anderson solved the Schrödinger equation for a crystalline array of potential wells with a random potential at each well [50]. The solution Anderson derived predicted that the eigenmodes of a disordered lattice are altered by strong interference effects among multiple scattering events which cause the electron wave function to collapse from an extended state (Bloch waves) into exponentially-localized states. In other words disorder leads to localization and thus the material behaves like a non-absorbing insulator. This is the reason why glass is transparent. Ioffe and Regel used the uncertainty principle to derive a relationship between the wavelength of the plane waves and the mean free path to determine when strong scattering begins [51]. Although Anderson localization was derived for electrons in a disordered potential it can be applied in general to any wave system with disorder [52]. Recently it was shown that optical wave propagation in disordered one-dimensional photonic waveguide lattices with random fluctuations exhibits transverse localization (i.e. the optical wave no longer diffracts) [53]. Anderson localization was used by Mott to predict that the lowest states in the conduction band of glass are localized [54]. Only at a critical value, known as the mobility edge, will the electrons transform from localized to extended states. An ideal disordered solid has no broken bonds and uniform bond angles and lengths. In reality structural defects exist within a material. For example a dangling bond in glass creates deep localized states within the band gap. These localized states are different from the localized states due to glass network disorder. When these defect states trap charge carriers characteristic absorption can be observed. This will be discussed in further detail in Section 2.3. For now let us conclude by drawing the energy band diagram appropriate for glass, Figure 2.4.

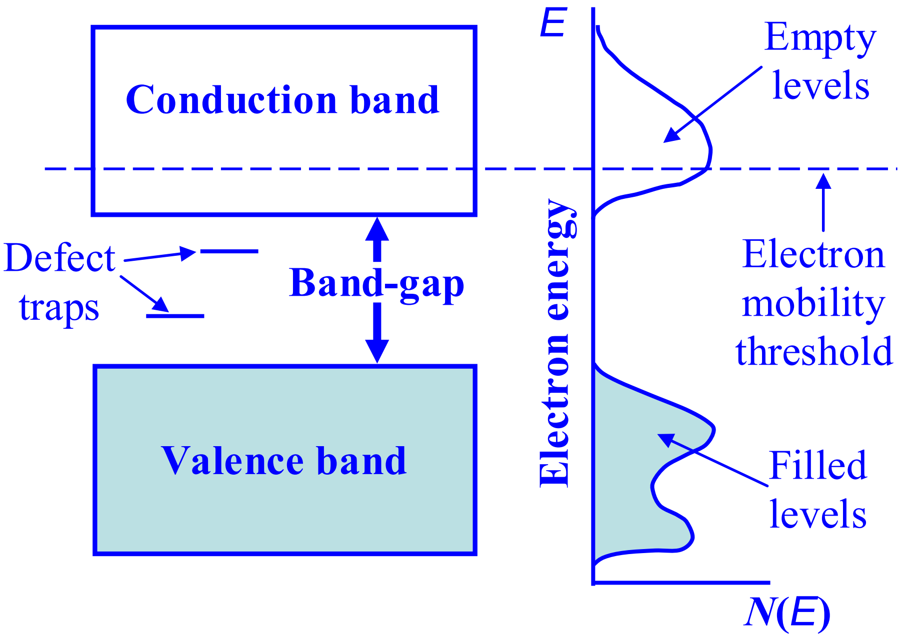

Figure 2.4. Energy band diagram for electron states in glass. *N(E)* is the density of states.

It is important that the transformation of the energy level diagram from crystalline to disordered solid is only minor because experiments show that glassy and crystalline solids of the same composition have many common traits. For example the positions and structure of the main absorption bands are very similar and diffraction studies show that nearest neighbor positions of atoms are nearly the same.

2.3 Defects in Glasses

Defects in glass can be treated as traps for electrons or holes. They typically arise from broken or missing bonds in the atomic structure of a glass. One important property they have is that an electron or hole trapped at a defect sites will exhibit absorption characteristics different from the surrounding glass matrix. Often the absorption will be in the visible region and thus the name ‘color centers’ has been given to these types of defects. Radiation can create defects in glass. Röntgen noticed that the glass door knob in his X-ray room had assumed a blue-gray color and solarization of glass by ultraviolet light from the sun was identified already in the 19th century. One example of a color-center in silicate glass is the E’ (E-prime) center. It was first discovered in 1956 by Weeks using the technique of electron spin resonance [55]. The E’ center behaves as a hole center and exhibits characteristic absorption at 5.8 eV. In general alkali-silicate glasses show a number of intrinsic color centers. Each of the induced color center absorption bands can be described mathematically with a Gaussian band shape. Accurate studies have been done by Glebov et al. to determine the peak positions and halfwidths of the intrinsic color center bands in alkali-silicate glass [56]. Using the known band positions and halfwidths of color center bands in alkali-silicate glass a study was done to compare defect creation by different sources of irradiation [57]. Figure 2.5 summarizes the results. The important conclusion is that short laser pulses at long wavelengths will create hole center bands. The presence of hole centers is evidence of glass matrix ionization and therefore we can expect that the same laser pulses will photoionize PTR glass. If PTR glass can be photoionized by short laser pulses then the question is whether a photo-thermo-induced refractive index change will occur. In the Section 2.4 we study photosensitivity in PTR glass by exposure to short laser pulses.

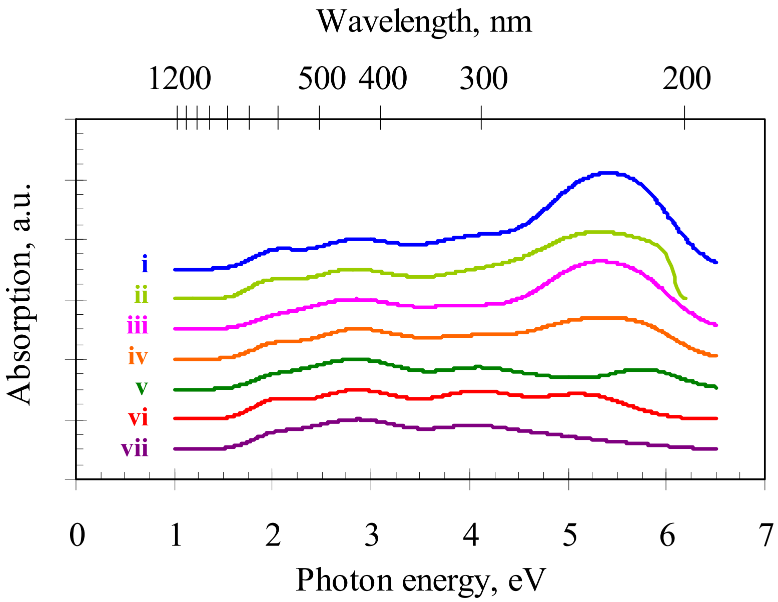

Figure 2.5. Induced color center absorption in soda-lime glass after exposure to (i) X-rays, 1.25 keV (ii) picosecond pulses at 1550 nm, 0.8 eV (iii) nanosecond pulses at 355 nm, 3.5 eV (iv) femtosecond pulses at 780 nm, 1.6 eV (v) nanosecond pulses at 266 nm, 4.7 eV (vi) gamma-rays, 1.17&1.33 MeV (vii) Xeon lamp, 5.8-6.5 eV. All graphs are normalized to the color center peak at 2.85 eV and shifted vertically for clarity.

2.4 PTR Glass Nonlinear Photosensitivity

Photosensitivity in PTR glass is quantified by the induced refractive index change Δn after successive exposure and thermal development. Depending on the duration of thermal development, Δn in PTR glass can be as high as 10^{-3} (1000 ppm). For a linear photosensitivity process the typical dependence of Δn on energy dosage and intensity was shown in Figure 1.3. It can be seen that for a linear process, refractive index change does not depend on the intensity of light but only on the exposure dosage. The Δn versus dosage dependence for linear photosensitivity obeys a hyperbolic relationship given by the equation

$$\Delta n(D) = n_{\max} \frac{D}{k + D} \qquad (2.1)$$

where $\Delta n(D)$ is the refractive index change as a function of dosage, $n_{\max}$ is the saturation index, and k is a fitting parameter. Typically exponential curves are used to fit photosensitivity dependencies. An exponential dependence is expected when photoionization releases an electron and the electron is subsequently trapped by a photosensitivity site. However it is possible for the electron to be retrapped by the hole center generated by photoionization instead of by the photosensitivity site. In this case solving the appropriate differential equation for photoionization and trapping results in a hyperbolic relationship [58]. To characterize nonlinear photosensitivity in PTR glass we performed experiments to determine the Δn vs. dosage and Δn vs. intensity curves. The approach is exactly the same as in Ref. [59] except now laser pulses are used as the exciting radiation instead of cw laser radiation. First PTR glass samples are fixed to a computer controlled translation stage and moved across the excitation laser beam at constant velocity. A lens is used to obtain the high-intensities needed for nonlinear ionization and a polarizer controlled the exact value of intensity. Figure 2.6 summarizes the setup. For translation along the y-axis this exposure results in a line with a lateral x-axis profile of energy dosage [J/cm^2] given by

$$D(x) = \sqrt{\frac{2}{\pi}} \frac{E_p R}{v w} \exp\left(-2 \frac{x^2}{w^2} \right) \qquad (2.2)$$

where E_p is the energy per pulse [J/pulse], R is the repetition rate of the laser [pulses/sec], v is the scanning velocity [cm/sec] and w is the beam waist, HWe^{-2}M [cm]. This equation is only valid for laser pulses with Gaussian spatial distribution of energy and for scanning conditions that obey $v/R < w$ (this last condition is necessary to ensure that the pulses overlap and create a smooth profile).

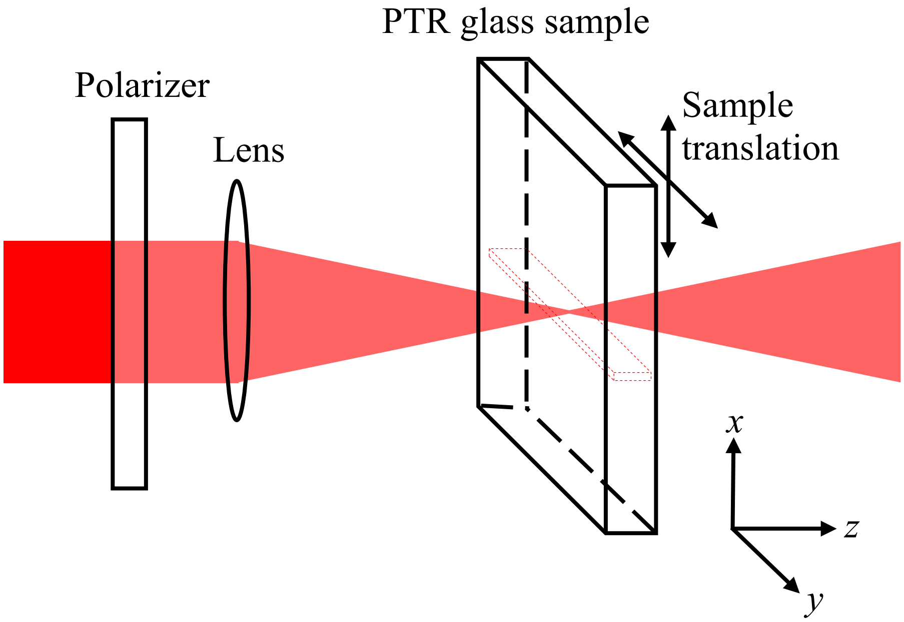

Figure 2.6. Experimental setup for short laser pulse line scanning in PTR glass. Laser radiation travels in the +*z*-direction.

The intensity *I* at the center of an incident Gaussian laser pulse is determined by

$$I = \frac{2}{\pi}\frac{E_p}{w^2\tau} \tag{2.3}$$

where τ is the temporal width, FWHM [sec], of the laser pulse. Glass samples were placed after the focal point of the lens in order to avoid optical damage at the surface. Knife-edge measurements were performed to determine the beam waist and confirmed that the beam spot profile was close to Gaussian. The value of the beam waist obtained gave values for the laser intensity only at the front surface of the glass. Femtosecond pulses were generated from a Ti:sapphire regenerative amplifier system operating at the wavelength 780 nm, repetition rate 1 kHz, pulse duration ~120 fsec, and maximum energy per pulse about 1 mJ. For complete photosensitivity characterization several lines with different laser intensity and dosage were scanned in the same glass sample. In one square PTR glass sample (25 mm × 25 mm) approximately forty lines could be scanned. After scanning, the glass was thermally developed for 2 hours at 515°C. The refractive index change of each line was then measured using a shearing interferometer setup [59]. Its basic principle is to create an interferogram that relates the optical path change to a fringe shift. A liquid cell with index matching fluid was used to eliminate glass sample thickness variations from contributing to the fringe shift and therefore the interferometer measured only refractive index variations. Figure 2.7 shows typical interferograms of a PTR glass sample after exposure and thermal development. We see a fringe shift due to refractive index change in areas exposed to both low power UV radiation and high power IR femtosecond laser pulses. The lateral profile given by Equation 2.4 is evident in the exposed regions. The refractive index change Δn is determined by the formula

$$\Delta n = \frac{\lambda_{test}}{2L}\frac{\Delta\Lambda}{\Lambda} \tag{2.4}$$

where λ_{test} is the wavelength of the laser used in the shearing interferometer setup (here 632.8 nm), L is the thickness of the glass sample (about 2 mm), and $(\Delta\Lambda/\Lambda)$ is the fringe shift at maximum distortion. It is important to note that the fringe shift seen in Figure 2.7 for femtosecond laser scanning is in the same direction as for cw laser scanning. This indicates that the refractive index change by femtosecond pulse exposure after thermal development is negative, as one would expect for the process of photosensitivity in PTR glass. Moreover, interferograms taken before thermal development show no appreciable fringe shift after femtosecond pulse exposure. Only after heat treatment does the refractive index change appear. Thus we can reliably attribute the index change in PTR glass induced by IR femtosecond pulses as occurring from the photo-thermo-refractive process.

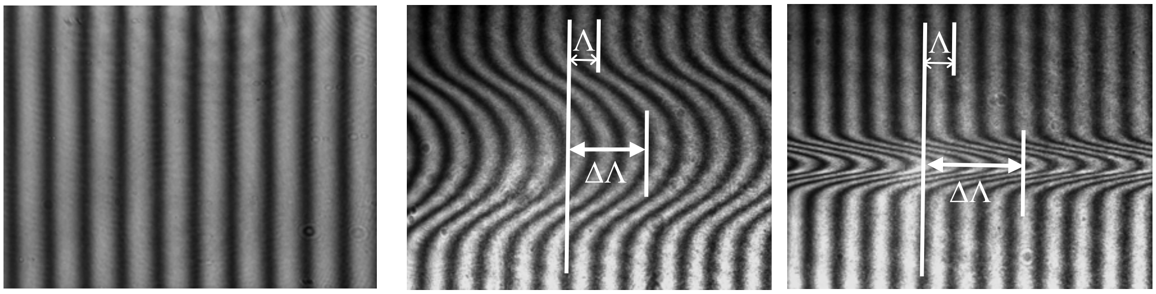

(a). (b). (c).

Figure 2.7. Interferograms of thermally developed PTR glass: (a) unexposed region (b) exposure to cw laser scanning (c) exposure to IR femtosecond laser scanning.

The nonlinear photosensitivity curves for femtosecond exposure of PTR glass are presented in Figure 2.8 [60]. For Δ*n* versus dosage we note that dosage is plotted on a log scale in contrast to the linear scale used for Δ*n* versus intensity. Curves of Δ*n* versus dosage could be fitted to hyperbolic curves, just like the curves describing linear photosensitivity, of the form given by Equation 2.1. The dependence of Δ*n* on intensity shows a starting threshold and quickly reaches saturation. Induced refractive index could not be observed after femtosecond exposure with intensity below about 1 TW/cm^2 while at 5 TW/cm^2 induced refractive index is at saturation. This dependence of Δ*n* on laser intensity indicates a strong nonlinear process occurred.

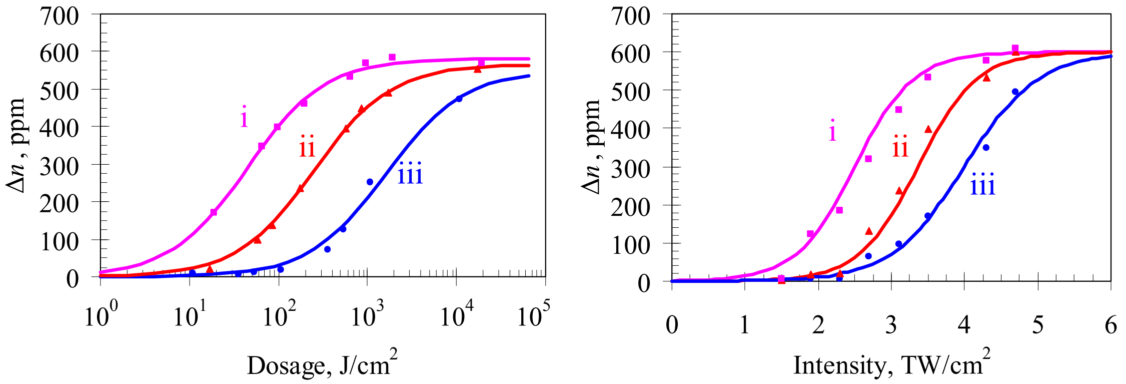

(a). (b).

Figure 2.8. Nonlinear photosensitivity characterization: (a) Δ*n* versus dosage (i) 1.9 TW/cm^2 (ii) 3.1 TW/cm^2 and (iii) 3.5 TW/cm^2; Δ*n* versus intensity (i) 25 J/cm^2 (ii) 130 J/cm^2 and (iii) 860 J/cm^2. Pulse wavelength 780 nm, pulse duration ~120 fsec, spot diameter 200 μm.

It has been shown that IR femtosecond pulses photoionize the glass matrix of PTR glass [61]. Therefore it is probably not necessary to include the dopant cerium in order to obtain nonlinear photosensitivity. To investigate the role of cerium in nonlinear photosensitivity by femtosecond laser pulses we prepared a PTR glass without the sensitizer cerium. After exposure to femtosecond laser pulses and thermal treatment this glass also shows a refractive index decrement with similar dependence on intensity and dosage as in the case of glass with cerium. Other laser pulse wavelengths and pulse durations were also tested. Both picosecond laser pulses at 1550 nm and nanosecond pulses at 355 nm showed nonlinear photosensitivity in PTR glass. The mechanism for nonlinear photosensitivity by nanosecond pulses at 355 nm can be explained by two-photon absorption. In the case of ultrashort laser pulses at 780 nm and 1550 nm nonlinear photosensitivity by nonlinear ionization requires further justification.

2.5 Summary

We discussed different approaches for shifting PTR glass photosensitivity to longer wavelengths. We established that PTR glass is photosensitive to short laser pulses at wavelengths longer than the linear absorption limit of PTR glass. No photosensitivity was observed when the intensity of laser pulses was below a certain threshold. It was shown that nonlinear photosensitivity is due to glass matrix photoionization. The mechanism responsible for photoionization by nanosecond pulses at 355 nm was shown to be two-photon absorption of laser radiation. The mechanism responsible for nonlinear photosensitivity by ultrashort pulses at infrared wavelengths will be discussed in the next chapter.

CHAPTER THREE: MECHANISM OF NONLINEAR PHOTOSENSITIVITY

In Chapter 2 we established that PTR glass is photosensitive to ultrashort laser pulses at wavelengths longer than the linear photosensitivity range for PTR glass. We saw that thermal development of PTR glass after exposure to ultrashort laser pulses leads to negative refractive index change and we characterized the index change as a function of laser intensity and energy dosage. The characteristic color center absorption in the exposed areas of the glass indicated that the glass matrix of PTR glass was photoionized. Thus it was possible to obtain nonlinear photosensitivity in PTR glass without the sensitizing dopant cerium. But how are photons with energy as little as 0.8 eV (1550 nm) able to photoionize the glass matrix of PTR glass which is placed at about 5.8 eV (212 nm) [40]? In this chapter we investigate the underlying physical mechanism responsible for nonlinear photosensitivity in PTR glass.

3.1 Introduction

Understanding the basic mechanisms of nonlinear photosensitivity in PTR glass requires analysis of laser pulse interaction with glass for different conditions of irradiation. At first let us analyze the effect for pulses with pulse duration long enough that the material response is not entirely electronic but may include other processes (e.g. molecular response). By misaligning the compressor gratings in a Ti:sapphire femtosecond laser system we obtained pulses with durations ranging from several to tens of picoseconds. Other laser parameters were photon energy of 1.6 eV (780 nm), linear polarization, 1 kHz repetition rate, and energy per pulse up to 1 mJ. A PTR glass sample of dimension 5×5×25 mm was prepared and polished on all sides. A 15 mm focal length lens was used to focus the pulses into the glass. Figure 3.1(a) shows the setup and Figure 3.1(b) shows a photograph from the experiment. After focusing inside the glass the picosecond pulses reach very high-intensity and generate plasma. The free electron density is high enough that the plasma absorbs and emits white-light. The plasma emission is seen to move in a direction opposite to that of the incident radiation. This is in agreement with the moving focus model of laser pulse self-focusing [62, 63]. The plasma generation causes permanent damage inside the glass.

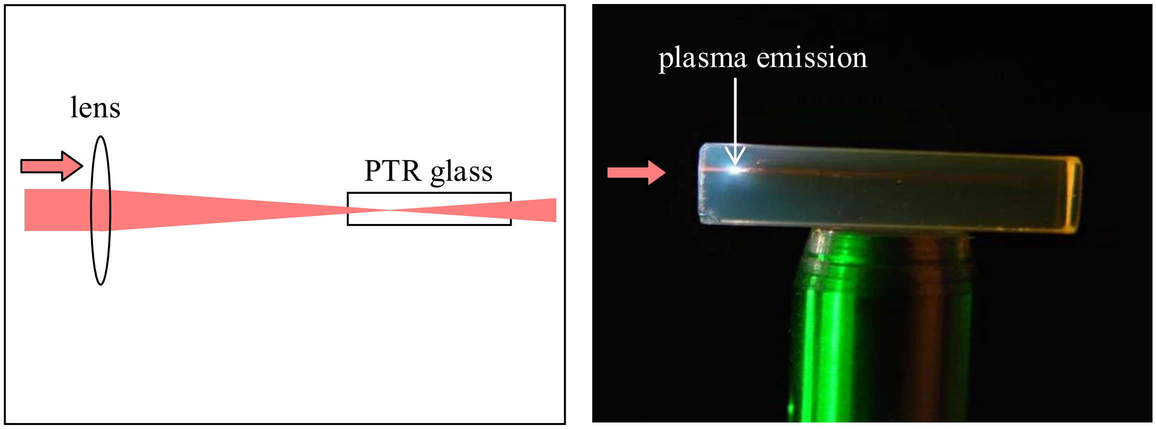

(a). (b).

Figure 3.1. A PTR glass sample irradiated by focused laser pulses ($\tau > 1$ psec): (a) setup (b) photograph from experiment. Laser pulses at 1.6 eV (780 nm), 1 kHz, ~1 mJ.

Let us now see what happens when the compressor gratings are correctly aligned and the pulses are shorter than one picosecond. Figure 3.2 shows the setup and a photograph from the experiment when femtosecond laser pulses interact with PTR glass. It should be noted that the glass sample was placed after the focal point of the lens and thus a diverging beam was incident on the glass. Three important observations can be made:

1. A long blue filament is formed inside the glass bulk.
2. Supercontinuum generation is emitted and extends into the visible spectral region.
3. The emitted supercontinuum shows a short-wavelength cutoff.

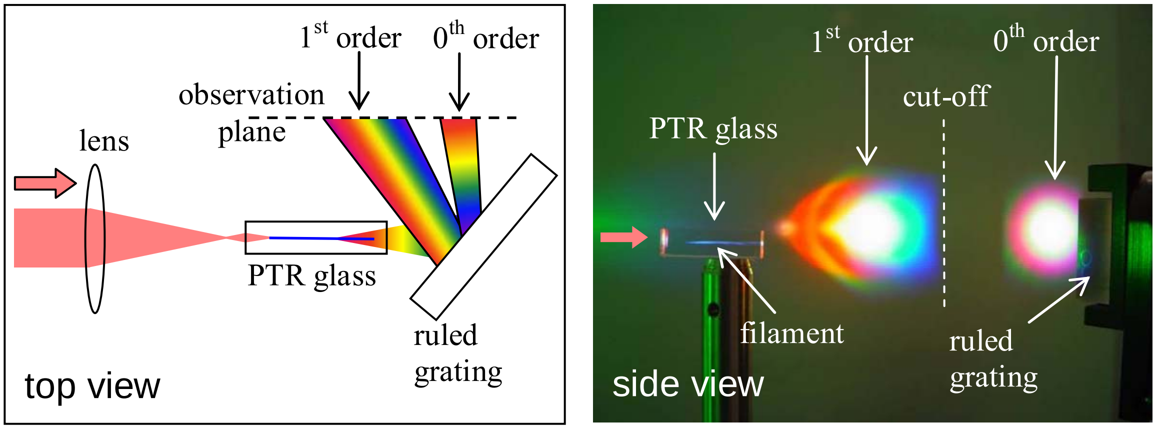

(a). (b).

Figure 3.2. A PTR glass sample irradiated by focused femtosecond laser pulses ($\tau < 1$ psec): (a) setup (b) photograph from experiment. Laser pulses at 1.6 eV (780 nm), 1 kHz, ~1 mJ.

Let us examine the blue filament in more detail. Figure 3.3 shows a magnified view of the filament. The onset of filamentation occurs inside the glass bulk at some distance from the front surface and is visible due to blue luminescence. In alkali-silicate glasses blue luminescence indicates recombination of intrinsic electron and hole centers produced by glass matrix ionization [64]. In PTR glass this area of blue luminescence is the area in which refractive index change occurs after thermal development. It is important to remark on the characteristics of supercontinuum generation from PTR glass. Figure 3.4 compares supercontinuum generation by IR femtosecond laser pulse irradiation for two different types of glasses; PTR glass and fused silica glass. In the case of fused silica we see that supercontinuum extends to significantly shorter wavelengths. Typically a spectrometer could detect supercontinuum wavelength components from fused silica extending to 250 nm whereas supercontinuum from PTR glass extended to only about 450 nm. However PTR glass is transparent up to 350 nm and one should expect supercontinuum to extend to this wavelength. One possible explanation for this effect is that the band gap of PTR glass shrunk under the influence of strong electric fields and linear absorption of wavelength components below about 450 nm occurred. The effect of strong electric fields will be considered in Section 3.4.

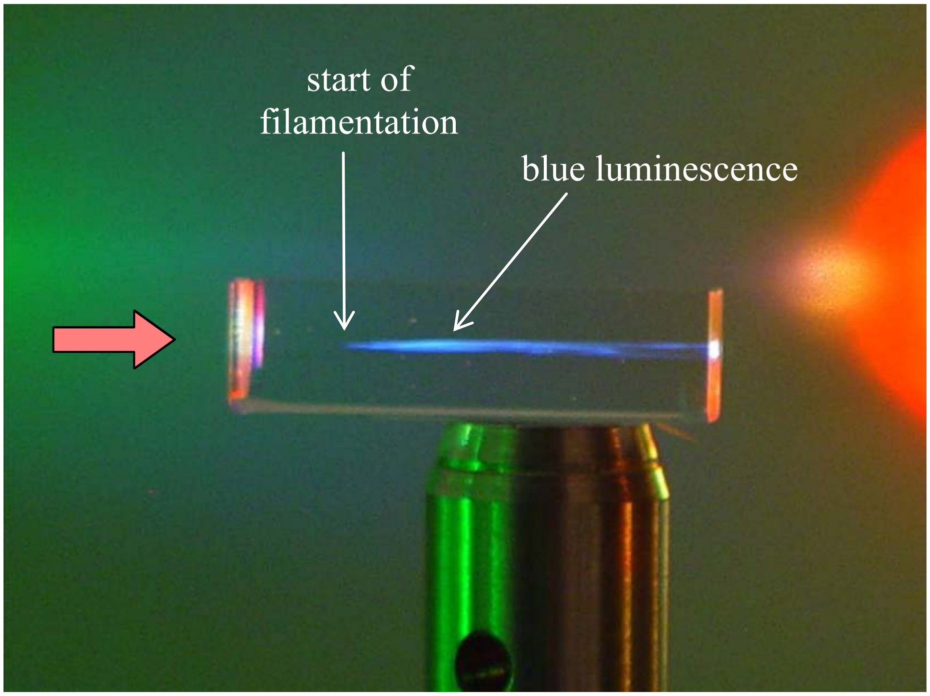

Figure 3.3. Filamentation in a PTR glass sample under irradiation by femtosecond laser pulses. Laser pulses at 1.6 eV (780 nm), 1 kHz, ~1 mJ.

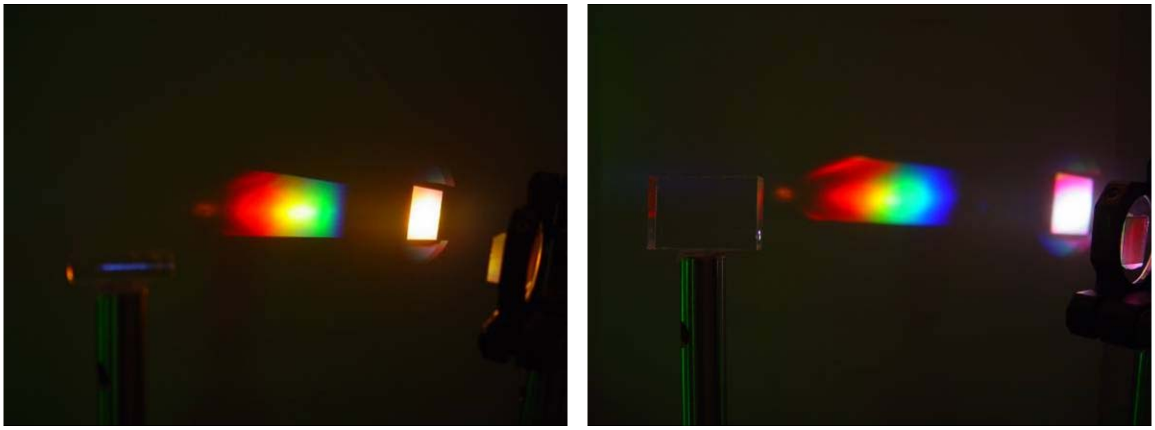

(a). (b).

Figure 3.4. IR femtosecond pulse irradiation of glass and diffraction by a ruled grating of the emitted supercontinuum: (a) PTR glass (b) fused silica glass. Laser pulses at 1.6 eV (780 nm), 1 kHz, ~1 mJ.

3.2 Intensity-Dependent Refractive Index

One of the most important effects to consider when high-intensity laser pulses interact with a material is how the refractive index of the material is modified. We write the intensity-dependent refractive index for Kerr-like media as

$$n(\mathbf{r},t) = n_0 + n_2\, I(\mathbf{r},t), \tag{3.1}$$

where n_0 represents the linear refractive index, n_2 is the second-order nonlinear refractive index, and I is the intensity of the optical field. For PTR glass the value of n_2 is approximately 3.3×10^{-20} m^2/W [65]. Equation 3.1 shows that refractive index variations will follow intensity variations. The intensity can vary in either the spatial or temporal domain. To explain why filamentation occurs at some distance inside the PTR glass sample we assume that self-focusing occurs. Self-trapping of light was considered by Chiao et al. to be a result of the nonlinear refractive index balancing the effects of spreading by diffraction [66]. A laser pulse with Gaussian spatial distribution of intensity will cause the greatest change in refractive index at the center where its intensity is the highest. For a material with positive n_2 the pulse causes the material to behave like a positive lens. Therefore as the pulse propagates inside the media it is also focused. The critical power for self-focusing is given by

$$P_{cr} = \frac{\pi \varepsilon_0 c (1.22)^2 \lambda_0^2}{32 n_2}. \tag{3.2}$$

For PTR glass the critical power at the wavelength 780 nm is calculated by Equation 3.2 to be 2 MW. A Ti:sapphire femtosecond laser operating at the wavelength 780 nm with pulse duration of 120 fsec and 1 mJ of energy per pulse has a peak power on the order of 8 GW. Therefore self-focusing of femtosecond pulses will occur in PTR glass. Whereas self-focusing is caused by modification of the refractive index due to the spatial profile of the pulse intensity we can also consider effects due to the temporal profile of the pulse intensity. The phase of a monochromatic plane wave can be written as

$$\phi = \mathbf{k} \cdot \mathbf{r} - \omega_0 t = \frac{\omega_0}{c} n(\mathbf{r}, t) \hat{\mathbf{k}} \cdot \mathbf{r} - \omega_0 t, \tag{3.3}$$

where we explicitly write the refractive index as being intensity-dependent. The instantaneous frequency of the wave is given by the time derivative of the phase and using Equation 3.1 to express the refractive index we arrive at

$$\omega = -\frac{d\phi}{dt} = \omega_0 - n_2 \frac{\omega_0}{c} \frac{dI}{dt} \hat{\mathbf{k}} \cdot \mathbf{r}. \tag{3.4}$$

Equation 3.4 shows that the instantaneous frequency in general is not constant but will change in time due to the time derivative of the intensity. An increase in intensity causes a red shift whereas a decrease causes a blue shift. This effect is called self-phase modulation and is usually used to explain supercontinuum generation [67]. Other important mechanisms that contribute to supercontinuum generation are four wave mixing and stimulated Raman scattering.

We have seen that the intensity-dependent refractive index can explain both self-focusing and supercontinuum generation in matter. Self-focusing is a result of spatial variations in the intensity of the exciting wave whereas supercontinuum generation is a result of temporal variations in the intensity. Self-focusing in PTR glass permits one to explain why an incident diverging beam is refocused inside the glass bulk. However self-focusing is a phenomena usually associated with catastrophic optical breakdown. In the case of irradiation by femtosecond laser pulses we observe a filament but unlike the case of plasma generation from picosecond pulses optical damage is not obvious. In the next section we investigate laser-induced damage in glass by ultrashort pulse irradiation.

3.3 Laser-Induced Damage

We first examined laser-induced damage in PTR glass samples with an optical microscope. The glass samples were irradiated by ultrashort laser pulses. However instead of irradiating the PTR glass samples at a single spot we placed the samples on a computer-controlled translation stage and scanned multiple lines (grating patterns) to obtain a larger area for microscopic examination. Thin samples, about 2 mm in thickness, were used. A long focal lens, f = 1 m, was used to achieve a long Rayleigh length at the focal plane and therefore a constant beam size throughout the glass sample. Any photoionization process (linear or nonlinear) in PTR glass is accompanied with the appearance of induced absorption in the UV/visible range. Thus to differentiate the effects of optical damage from induced absorption a cw He-Cd laser at 325 nm was also used for laser scanning in the same glass sample in which ultrashort laser pulse scanning was performed. This permits the cw-irradiated areas to be used as a reference against the ultrashort laser pulse irradiated areas. Figure 3.5 shows the scanning setup and the expected uniform transverse distribution of the beam dosage in the sample.

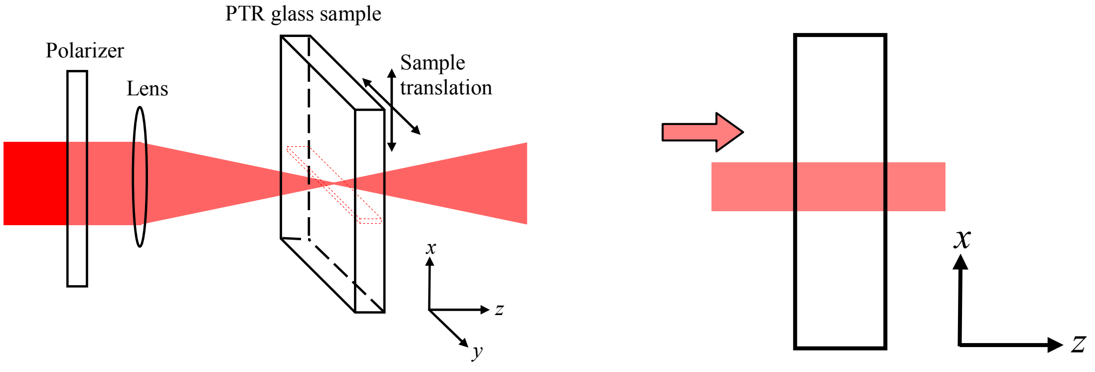

(a).   (b).

Figure 3.5. Femtosecond and cw laser irradiation of PTR glass for optical microscope study of laser-induced damage: (a) scanning setup (b) lateral view of the sample at the focal plane when irradiated by a long Rayleigh length laser beam.

Figure 3.6 shows the result of femtosecond and cw laser scanning of PTR glass. The surface damage seen in Figure 3.6(a) was the result of an extrinsic glass defect initiating damage. The triangular pattern that resulted was due to the initial damage site growing after each additional line was scanned. It is possible to observe photo-induced coloration in PTR glass after exposure to ionizing radiation. In the femtosecond laser irradiated area strong yellow coloration characteristic of color centers generated by glass matrix ionization is observed. In the cw laser irradiated area the coloration is weak, almost invisible, because photoionization of cerium does not result in stable color centers with absorption as strong as colors centers resulting from glass matrix ionization.

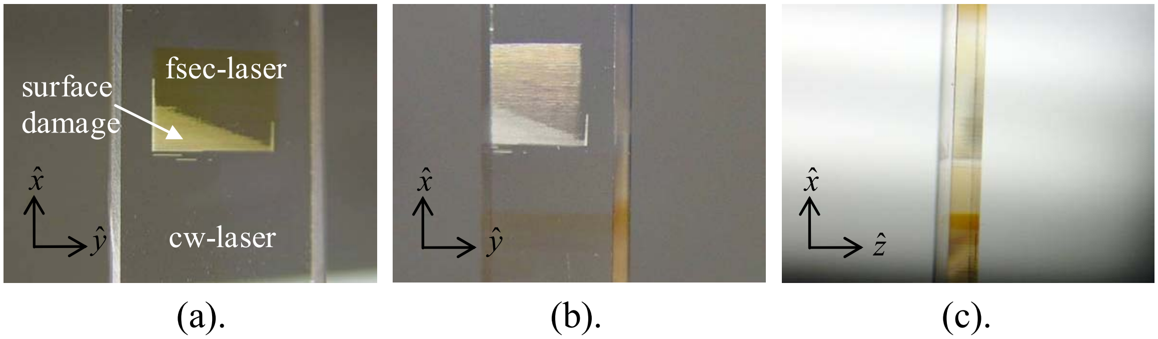

(a). (b). (c).

Figure 3.6. Photographs of PTR glass after irradiation by femtosecond and cw laser scanning to produce grating patterns: front view (a) before (b) after thermal development (c) lateral view after thermal development.

Figure 3.7 shows microscope images of the PTR glass sample seen in Figure 3.6 at a boundary between the surface damage area and the induced absorption area due to femtosecond laser exposure. It is apparent that damage differs from photo-induced coloration. This suggests that there is a condition when the intensity of ultrashort laser pulses is high enough for photoionization to occur in PTR glass but still below the damage threshold.

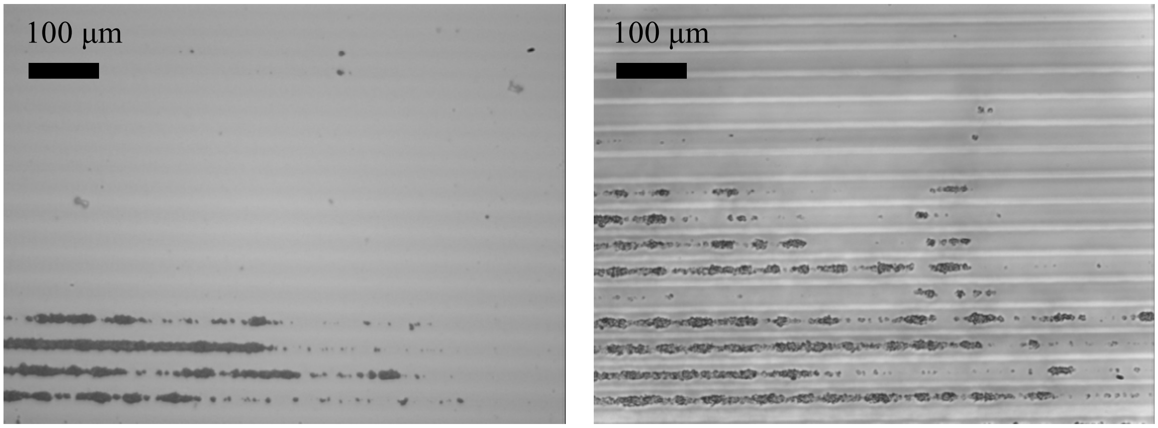

(a). (b).

Figure 3.7. Microscope images of PTR glass with a grating pattern produced by femtosecond laser scanning: (a) before (b) after thermal development.

Figure 3.8 shows also the effect of cw laser scanning in the PTR glass sample. At different depths of focus with the microscope the cw induced absorption lines stay the same. However in the case of femtosecond laser scanning we see that there is a depth of focus near the front surface where the morphology of the photo-induced lines changes, Figure 3.8(b). At this location the femtosecond laser most likely caused damage.

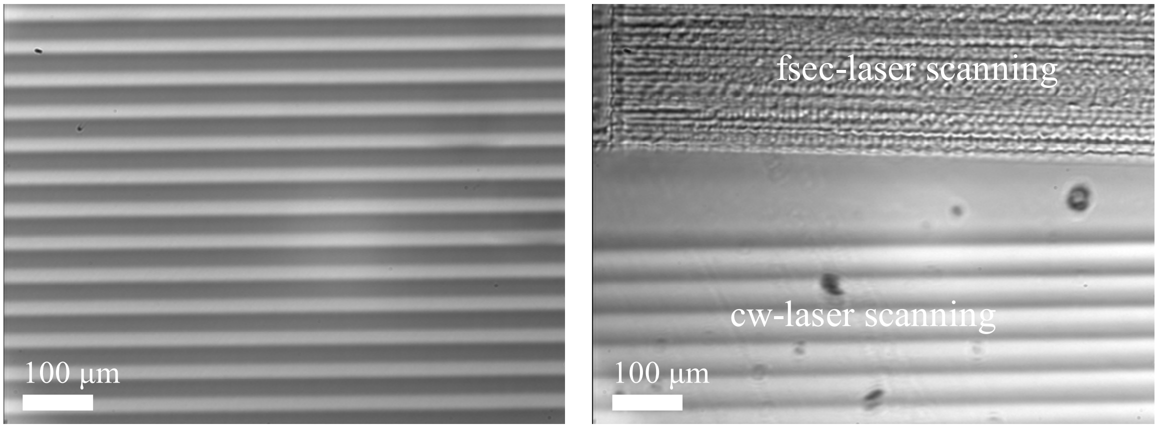

(a). (b).

Figure 3.8. Microscope images of PTR glass with grating pattern induced by cw laser scanning after thermal development: (a) only cw laser scanning (b) boundary between cw and femtosecond laser scanning.

Microscope images were also taken along the lateral direction of the PTR glass sample. This corresponds to imaging the surface seen in Figure 3.6(c). The results are shown in Figures 3.9 & 3.10.

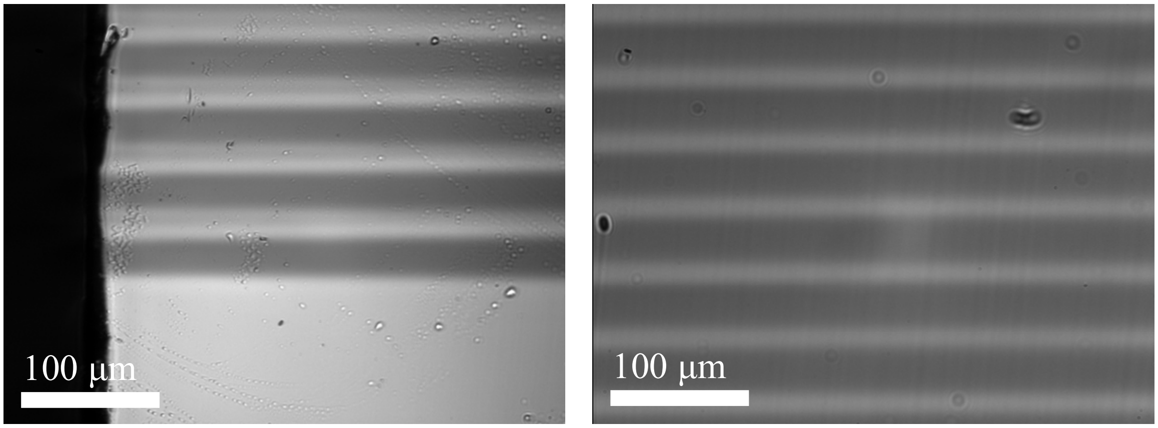

(a). (b).

Figure 3.9. Microscope images of lateral view of PTR glass exposed to cw laser scanning after thermal development: (a) front surface (b) near back surface.

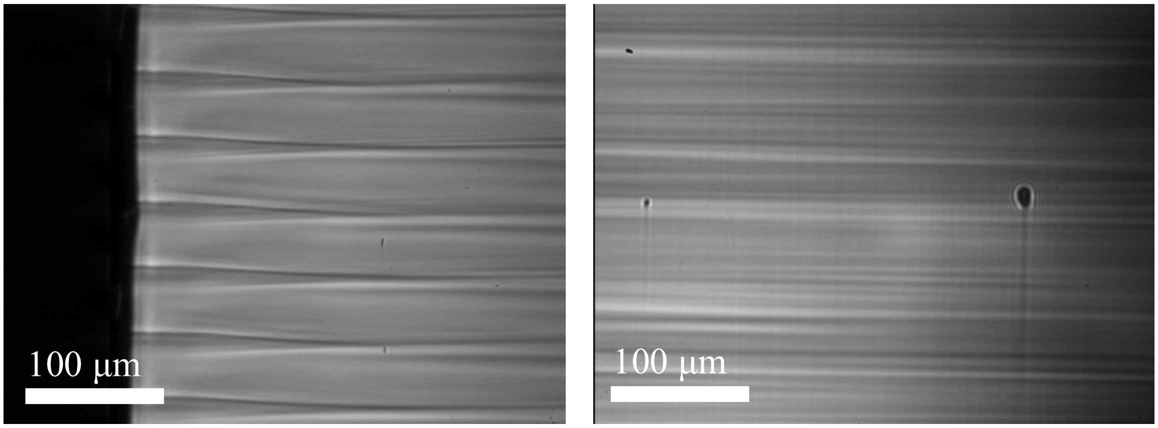

(a). (b).

Figure 3.10. Microscope images of lateral view of PTR glass exposed to femtosecond laser scanning after thermal development: (a) front surface (b) near back surface.

Lateral imaging shows that cw laser irradiation produces a constant photo-induced line along the entire thickness of the glass sample. However in the case of femtosecond pulse irradiation the photo-induced pattern was seen to self-focus near the front surface and form a filament. But by the time this filament reached the back surface it had broken up into multiple filaments and a clear single line cannot be seen, Figure 3.10(b). Breakup of a filament into multiple filaments has been described by Bespalov and Talanov to arise from instabilities in the propagating electromagnetic wave [68].

The results with the optical microscope show that damage by femtosecond pulse filamentation in PTR glass may have occurred at a single point near the front surface of the glass but did not extend through the bulk. However, this conclusion may be a result of inadequate resolution with the optical microscope and therefore we continued to examine laser-induced damage using scattering probe techniques. The first scattering technique we employed was to look at diffraction of the grating patterns that were recorded in PTR glass after laser scanning and after thermal development induced a refractive index change. The objective was to compare diffraction by the gratings created by femtosecond laser scanning with diffraction by gratings created by cw laser scanning. If the femtosecond laser caused damage then one would see not only diffraction but additional scattering by the probe laser. Figure 3.11 shows the diffraction patterns of the gratings. Testing was done with a 5 mW He-Ne laser at 633 nm. These gratings had a spatial period of ~50 μm and therefore were planar type gratings rather than volume type gratings. Planar type gratings exhibit multiple diffracted orders rather a single diffracted order characteristic of volume type gratings. In Figures 3.11(a) & (b) we see that diffraction by the grating formed by cw laser scanning is different from diffraction by the grating due to femtosecond laser scanning. The difference is that the femtosecond grating shows diffraction in the vertical direction whereas the cw laser grating only shows diffraction in the horizontal direction. This is attributed to the fact the femtosecond laser created filaments that broke up into multiple filaments before exiting the glass sample. Therefore after thermal development the refractive index changes were not constant throughout the glass bulk and a perfect grating pattern was not recorded. Therefore some diffraction occurs along the vertical direction. Nevertheless additional scattering due to laser-induced damage by the femtosecond laser is not obvious. In Figure 3.11(c) additional scattering due to the front surface damage is clearly observed.

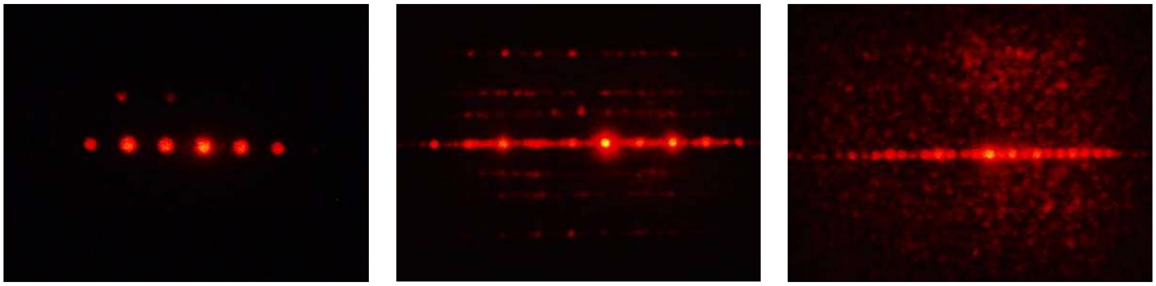
(a). (b). (c).

Figure 3.11. Photographs of diffraction of He-Ne laser at 633 nm by grating patterns in PTR glass produced by laser scanning: (a) cw laser scanning (b) femtosecond laser scanning (c) surface damaged femtosecond laser scanning.

Another scattering probe technique was performed. Instead of probing PTR glass after laser exposure and thermal development we performed real-time scattering measurements during laser irradiation. In this case it was possible to observe the time evolution of damage versus different parameters of laser irradiation. Rather than use the femtosecond laser at 780 nm we used a tunable picosecond laser (1.1-1.7 μm) to investigate real-time photoionization and damage in glass. As we will see scattering of third harmonic radiation indicates the creation of damage sites. Therefore, when the picosecond laser is tuned to 1550 nm its third harmonic is at 517 nm (green) and can be observed visually without absorption in the glass. Third harmonic of the femtosecond laser at 780 nm is placed at 266 nm (ultraviolet) and is not observable to the human eye as well as it is absorbed by PTR glass. In order to perform a more general study of laser-induced damage in silicate glass by ultrashort laser pulses we chose to make measurements in both fused silica glass, band gap is placed at about 9.3 eV (133 nm), and PTR glass. The setup for experiments is shown in Figure 3.12. A spherical lens (BK7 glass, *f* = 15 mm) is used to focus incident picosecond pulses into a fused silica glass sample (30 mm in length).

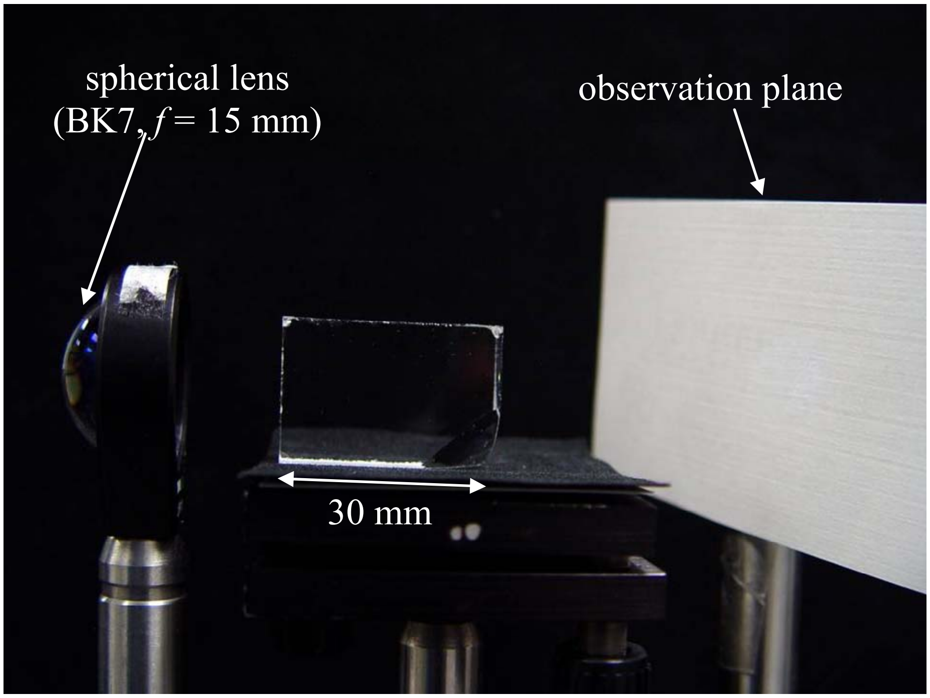

Figure 3.12. Setup for picosecond experiments with a spherical lens and fused silica glass.

Picosecond laser pulses were obtained from an Optical Parametric Amplifier (OPA) pumped by laser pulses at 800 nm from an amplified Ti:sapphire ultrashort laser pulse system. The picosecond pulses were tunable in the range 1.1-1.7 μm, ~1.2 psec in pulse duration, 1 kHz repetition rate, and ~20 μJ energy per pulse. The first wavelength tested was 1550 nm. This places third harmonic at 517 nm (green). Figure 3.13 shows a fused silica glass sample under irradiation by picosecond pulses at 1550 nm. Two important features are observed. First is that self-focusing increases the intensity of the picosecond pulses so that red luminescence is observed in the glass bulk. Second is that supercontinuum generation is emitted at the output of the glass.

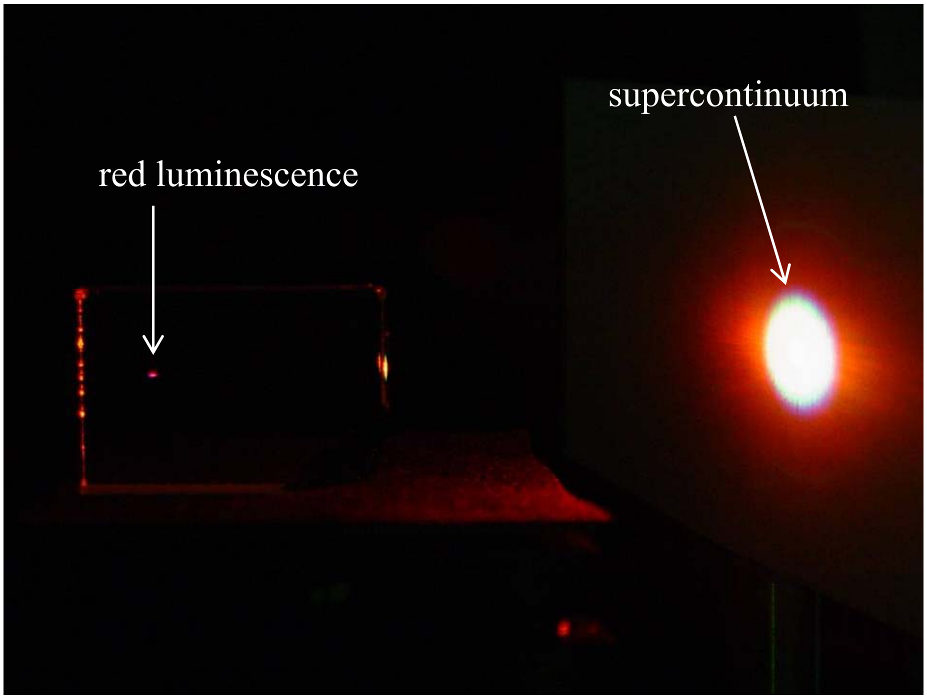

Figure 3.13. Fused silica glass irradiated by picosecond pulses at 1550 nm.

The time evolution of the fused silica sample during exposure to picosecond pulses is shown in Figure 3.14. For picosecond pulses at 1550 nm, Figure 3.14(a), we see a red spot in the glass bulk and supercontinuum generation at the glass output. The red spot is characteristic of defect centers (non-bridging oxygen hole centers) which luminescence at 1.85 eV (650 nm) [69]. After about two minutes the red spot begins to scatter green light (third harmonic of 1550 nm) and a green scattering ring is observed at the observation plane, Figure 3.14(b). Also the intensity of supercontinuum decreases. After about five minutes supercontinuum almost disappears (it recurs at irregular intervals) and the red spot is no longer noticeable due to strong green scattering, Figure 3.14(c). A similar time evolution is observed for picosecond pulses at 1430 nm (third harmonic at 477 nm, blue), Figure 3.14(d-f). However the difference with 1430 nm picosecond pulses is that the scattering ring appears earlier in time, a long red luminescent filament is observed, and supercontinuum never disappears after several minutes of exposure.

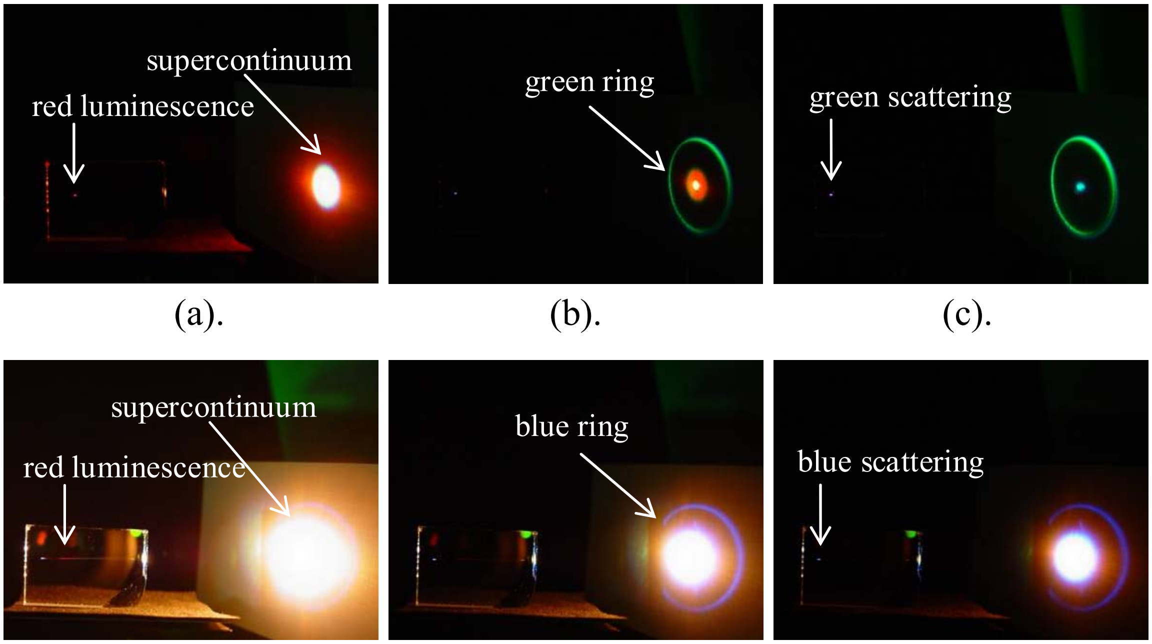

(a). (b). (c).

(d). (e). (f).

Figure 3.14. Time evolution of focused picosecond pulse propagation in fused silica glass: Pulses at 1550 nm (a) start time (b) after two minutes (c) after five minutes; at 1430 nm (d) start time (e) after < 1 minute (f) after five minutes.

The long red filament in the case of 1430 nm picosecond pulse irradiation is in contrast to the "spot" observed with 1550 nm picosecond pulses. A larger picture of the filament produced by 1430 nm picosecond pulses is shown in Figure 3.15. However once damage begins and blue third harmonic appears, the filament decreases in length. Again it is important to emphasize that red luminescence in fused silica glass results from recombination of intrinsic electron and hole centers produced by glass matrix ionization. The band gap of fused silica is placed at 9.3 eV. For pulses at 1550 nm (0.8 eV) to cause glass matrix ionization requires a twelve-photon process. To check if such a process can occur we must calculate the probability of nonlinear ionization.

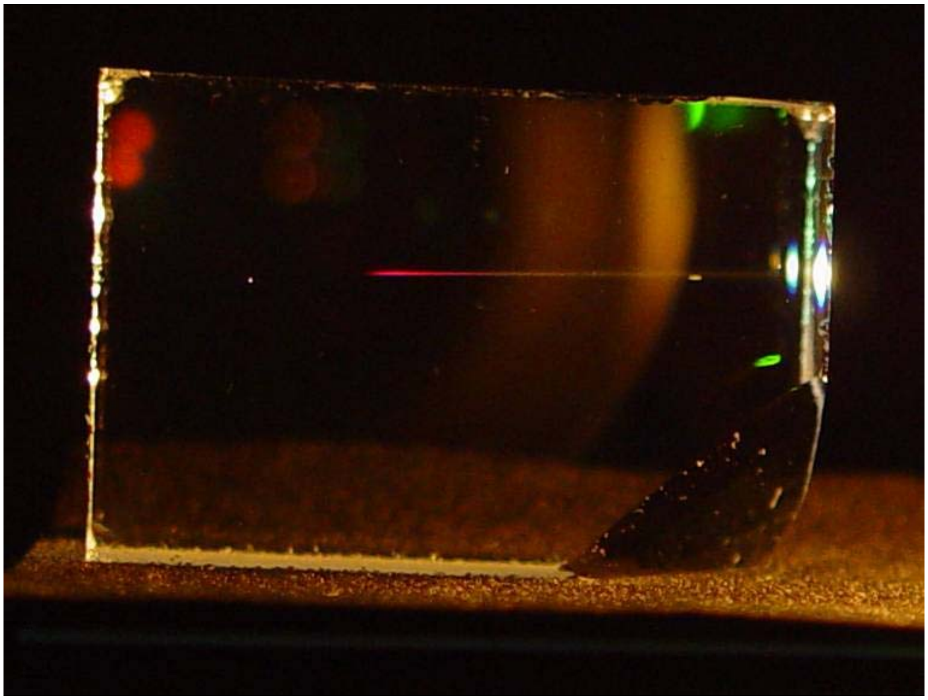

Figure 3.15. Red filament in fused silica glass observed by focused high-intensity 1430 nm picosecond pulses.

3.4 Nonlinear Ionization

To model nonlinear ionization it is necessary to apply the laws of quantum mechanics. We want to know how the wave function $\psi(\mathbf{r},t)$ of an electron in glass evolves over time under the influence of an ultrashort laser pulse. Therefore it is necessary to solve the time-dependent Schrödinger equation

$$i\hbar \frac{\partial \psi(\mathbf{r},t)}{\partial t} = \hat{H}\psi(\mathbf{r},t), \tag{3.5}$$

where the Hamiltonian *H* is written as

$$\hat{H} = \hat{H}_0 + \hat{V}(t). \tag{3.6}$$

The Hamiltonian accounts for all forces acting on the electron. For simplification it is assumed that the static part of the Hamiltonian can be separated from the time-dependent part. If only electric-dipole transitions are considered the interaction energy of an atom can be written as

$$\hat{V}(t) = -e\mathbf{r} \cdot \boldsymbol{E}(t). \tag{3.7}$$

Perturbation theory is often used to solve for nonlinear ionization in terms of multiphoton absorption. The theory works under the assumption that $V_0 << H_0$ where V_0 is the magnitude of $V(t)$. To check the validity of this theory for high-intensity ultrashort laser pulse irradiation we calculate the magnitude of V_0 which is given by $V_0 = e\,x_0\,E_0$ where E_0 is the magnitude of the electric field and x_0 is the maximum displacement of the electron. Assuming free electron motion the parameter x_0 can be determined from

$$x_0 = \frac{eE_0}{m_e\,\omega^2}, \tag{3.8}$$

which results in

$$V_0 = \frac{e^2 E_0}{m_e\,\omega^2}. \tag{3.9}$$

Equation 3.9 is also the expression for the ponderomotive energy. For a strong electric field value of $E_0 = 10^8$ V/cm (intensity equal to 10^{13} W/cm^2) and photon energy equal to 1.6 eV ($\omega = 2.4\times10^{15}$ rad/sec) the interaction energy V_0 is equal to 3 eV. This can be a significant perturbation. For PTR glass the parameter H_0 can be taken to be equal to 5.8 eV (the band gap energy) and the assumption $V_0 << H_0$ needed for perturbation theory no longer holds.

It is known that strong electric fields affect the band structure of dielectric solids via the Franz-Keldysh effect [70, 71]. In terms of nonlinear ionization it is therefore important to account for another mechanism, i.e. tunneling, when considering multiphoton processes induced by ultrashort laser pulses. Figure 3.16 illustrates how both direct (multiphoton) and indirect (tunneling) processes result in nonlinear ionization.

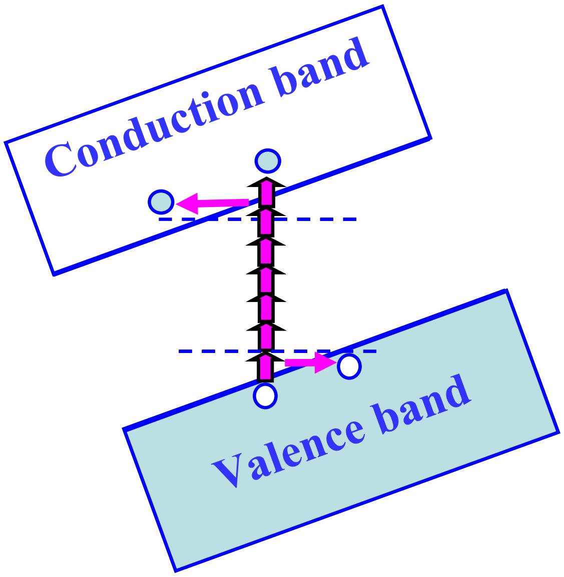

Figure 3.16. Influence of a strong electric field on the energy band structure of a dielectric solid. Nonlinear ionization can occur directly by multiphoton absorption or indirectly via tunneling.

A general model that accounts for the influence of strong electric fields on the ionization rate in matter was first proposed by L.V. Keldysh in 1965 [72]. Although the model assumes an energy band structure most appropriate for narrow gap semiconductors we will attempt to use it for glass. The expression derived by Keldysh for the ionization rate per unit volume is given by

$$\begin{aligned} W = \frac{2\omega}{9\pi}\left(\frac{\sqrt{1+\gamma^2}}{\gamma}\frac{m^*\omega}{\hbar}\right)^{3/2} Q\left(\gamma,\frac{\tilde{E}_g}{\hbar\omega}\right)\exp\left\{-\pi\left\langle\frac{\tilde{E}_g}{\hbar\omega}+1\right\rangle\right. \\ \left.\times\left[K_1\left(\frac{\gamma}{\sqrt{1+\gamma^2}}\right)-K_2\left(\frac{\gamma}{\sqrt{1+\gamma^2}}\right)\right]\Big/ K_2\left(\frac{1}{\sqrt{1+\gamma^2}}\right)\right\}, \end{aligned} \tag{3.10}$$

where

$$\tilde{E}_g = \frac{2}{\pi}E_g\frac{\sqrt{1+\gamma^2}}{\gamma}K_2\left(\frac{1}{\sqrt{1+\gamma^2}}\right), \tag{3.11}$$

$$\gamma = \frac{\omega}{e}\sqrt{\frac{m^* n_0\,\varepsilon_0\,c E_g}{2I}}, \tag{3.12}$$

$$K_1(x) = \int_0^{\frac{\pi}{2}} \frac{d\theta}{\sqrt{1 - x^2 \sin^2 \theta}}, \tag{3.13}$$

$$K_2(x) = \int_0^{\frac{\pi}{2}} \sqrt{1 - x^2 \sin^2 \theta}\, d\theta, \tag{3.14}$$

$$\Phi(z) = \int_0^{z} \exp\left(y^2 - z^2\right) dy, \tag{3.15}$$

and

$$\begin{aligned} Q(\gamma, x) = {} & \left[\pi \middle/ 2K_1\left(\frac{1}{\sqrt{1+\gamma^2}} \right) \right]^{1/2} \sum_{n=0}^{\infty} \exp\left\{ -\pi n \left[K_1\left(\frac{\gamma}{\sqrt{1+\gamma^2}} \right) \right. \right. \\ & \left. \left. - K_2\left(\frac{\gamma}{\sqrt{1+\gamma^2}} \right) \right] \middle/ K_2\left(\frac{1}{\sqrt{1+\gamma^2}} \right) \right\} \\ & \times \Phi\left\{ \left[\pi^2 \left(2\langle x+1 \rangle - 2x + n \right) \middle/ 2K_1\left(\frac{1}{\sqrt{1+\gamma^2}} \right) K_2\left(\frac{1}{\sqrt{1+\gamma^2}} \right) \right]^{1/2} \right\}. \end{aligned} \tag{3.16}$$

The parameters in the above expressions are defined as follows: I is the peak intensity, m^* is the effective reduced mass of the electron and hole pair, E_g is the energy band gap of the material, ω is the laser frequency, and $\langle\ \rangle$ denotes the integer part of the argument. To avoid the complicated mathematical expression for the ionization rate we refer to it simply as W and emphasize it is a function of only four unknown variables

$$W = W_{Keldysh}\left(E_g, \omega, m^*, I\right). \tag{3.17}$$

For the experiment using focused 1550 nm picosecond laser pulses in fused silica glass we have parameter values given in Table 3.1.

Table 3.1. Values of parameters used to solve Keldysh expression for nonlinear ionization in fused silica glass excited by 1550 nm picosecond laser pulses.

Parameter	Value
E_g	9.3 eV (133 nm)
ω	1.2×10^{15} rad sec^{-1} (1550 nm)
n_0	1.444
m^*	$0.2m_e$

The one difficult parameter to estimate is the effective mass m^*. The effective mass is largely a measure of the average strength of the dipole matrix element in the Keldysh theory and is not expected to correspond to real transport carrier properties in the material. To determine m^* for fused silica we solved the Keldysh transition rate equation for the case of two-photon absorption for which there are published values of the two-photon absorption coefficient [73, 74]. The formulas for the multiphoton absorption coefficient and multiphoton cross-section are given by

$$\beta^{(\mathrm{N})} = 2\frac{\mathrm{N}\hbar\omega}{I^{\mathrm{N}}}W, \tag{3.18}$$

$$\delta^{(\mathrm{N})} = 2\mathrm{N}\left(\frac{\hbar\omega}{I}\right)^{\mathrm{N}}\frac{W}{N_A}, \tag{3.19}$$

where

$$\mathrm{N} = \left\langle \widetilde{E}_g / \hbar\omega + 1 \right\rangle. \tag{3.20}$$

and N_A is the number of atoms per unit volume. Table 3.2 lists the predicted values of two- and three-photon parameters assuming an effective mass of $0.2m_e$ and concentration $N_A = 10^{22}$ cm^{-3}.

Table 3.2. Two- and three-photon predicted values for multiphoton absorption coefficient and cross-section coefficient for fused silica using Keldysh theory of multiphoton ionization. Effective mass assumed to be equal to $0.2m_e$.and concentration $N_A = 10^{22}$ cm^{-3}.

N	$\beta^{(N)}$ [cm^{2N-3} erg$^{-(N-1)}$ sec^{N-1}]	$\delta^{(N)}$ [cm^{2N} photon$^{-(N-1)}$ sec^{N-1}]
2	2×10^{-18}	5×10^{-50}
3	5×10^{-39}	3×10^{-82}

The effective mass was chosen to be $0.2m_e$ because it reproduces the two-photon absorption coefficient value of $\beta^{(2)} = 2 \times 10^{-18}$ cm erg^{-1} sec^{1} in fused silica reported by Ref. [74]. When the parameters ω, E_g, and m^* are known the nonlinear transition rate given by Equation 3.17 is only a function of intensity. Our goal is to use the Keldysh formula to determine a value of intensity and compare its order of magnitude to known values for filamentation, supercontinuum generation, and/or laser-induced damage in optical materials. Therefore we need a second equation relating the nonlinear transition rate to the intensity of the optical field. In the next section we discuss how to determine this second equation.

3.5 Free-Electron Generation

We have seen that focused ultrashort laser pulses in glass will form filaments. Therefore a mechanism exists that stops self-focusing. We have also seen that filamentation will photoionize fused silica glass. Thus with these two observations let us consider the possibility that free electrons are responsible for stopping self-focusing. This approach was first used by Yablonovitch and Bloembergen to support their theory of intrinsic optical damage by avalanche ionization [75]. However in our experiments damage does not occur instantaneously. Furthermore the theory of intrinsic damage by avalanche ionization has been questioned by several authors [32-36]. Nevertheless the assumption of defocusing by free-electrons is independent of the theory of avalanche ionization. When defocusing by free-electrons is considered Equation 3.1 must be rewritten in the form

$$n = n_0 + n_2 I - \frac{2\pi N_e e^2}{n_0 m_e (\omega^2 + {\nu_e}^2)}, \tag{3.21}$$

where N_e is free-electron density and ν_e is the electron collision frequency. We follow the approach of Brodeur and Chin to determine the final equation that balances self-focusing with free electron defocusing [76]. In the limit that $\omega >> \nu_e$ we have

$$n_2 I = \frac{2\pi N_e e^2}{n_0 m_e \omega^2}. \tag{3.22}$$

Because the electric field of an optical wave is alternating very quickly we consider only the number of free-electrons generated in a time interval of half an optical cycle, i.e. $\Delta t = ½(2\pi/\omega)$. We write the free-electron density as the transition rate multiplied by the time interval for transitions

$$N_e = W\,\Delta t = W\frac{\pi}{\omega}. \tag{3.23}$$

Combining Equations 3.22 and 3.23 gives

$$W_{free-electrons} = \frac{n_2 n_0\, m_e \omega^3}{2\pi^2 e^2} I, \tag{3.24}$$

where we emphasize that this transition rate determines the number of free-electrons needed to balance the effect of self-focusing. Equation 3.24 is the second equation relating the transition rate to intensity that we were looking for. Using Equations 3.17 & 3.24 we can calculate a value for the intensity that photoionizes fused silica as well as balances the effects of self-focusing to form a filament. An analytic solution is not possible but we can plot both equations and find where they intersect. Figure 3.17 shows both Equations 3.17 & 3.24 plotted on the same graph using the parameter values given in Table 3.1 and assuming the nonlinear refractive index n_2 is equal to 3×10^{-16} cm^2/W.

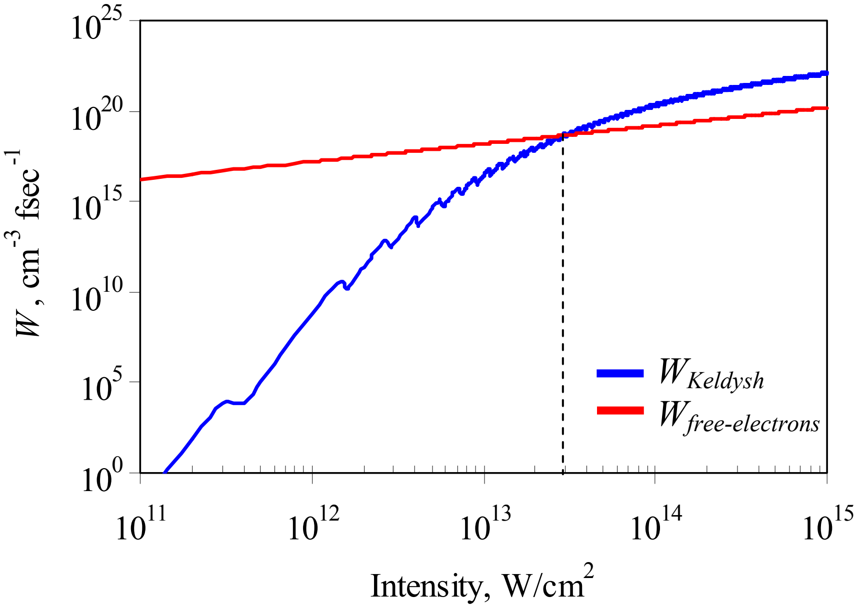

Figure 3.17. Transition rates for nonlinear ionization (blue) and free-electron balance of self-focusing (red) for fused silica irradiated by 1550 nm picosecond pulses.

From Figure 3.17 the intensity and rate at which $W_{Keldysh} = W_{free\text{-}electrons}$ are 3×10^{13} W/cm^2 and 4.5×10^{18} cm^{-3} fsec^{-1} respectively. Solving Equation 3.23 for the free-electron density gives a value of 1×10^{19} cm^{-3}. Our value of intensity compares reasonably with published results of damage threshold in glass, ~10^{13} W/cm^2 [77, 78]. To check our estimate for free-electron density generation we can compare it to a pump-probe experiment done in fused silica with ultraviolet femtosecond pulses that resulted in permanent structural changes only when the electron density exceeded ~4×10^{19} cm^{-3} [79]. The preceding analysis of balancing between self-focusing and free-electron generation can also be applied to PTR glass irradiated by femtosecond laser pulses at 780 nm. Table 3.3 lists the values of parameters and the nonlinear refractive index n_2 of PTR glass is taken to be 3.3×10^{-16} cm^2/W.

Table 3.3. Values of parameters used to solve Keldysh expression for multiphoton absorption in femtosecond irradiated PTR glass.

Parameter	Value
E_g	5.8 eV (212 nm)
ω	2.4×10^{15} rad $\sec^{-1}$ (780 nm)
n_0	1.49
m^*	$0.2m_e$

The result for PTR glass is that the intensity required for nonlinear ionization to stop self-focusing is 1×10^{13} W/cm^2 and the corresponding free-electron density is 2×10^{19} cm^{-3}. To check this estimate of free-electron density let us calculate the density of electrons needed to saturate the refractive index change in PTR glass since oftentimes PTR glass samples irradiated by ultrashort laser pulses showed saturation in the refractive index change. From the linear photosensitivity behavior of PTR glass we know that a dosage of 2 J/cm^2 in a 0.2 cm thick sample for laser light exposure at 325 nm will saturate the change in refractive index. The electron density generated by linear absorption can be determined from the following formula

$$N = \left(1 - 10^{-\alpha t}\right)\frac{D/\hbar\omega}{L}., \tag{3.25}$$

where D is the dosage, L is the thickness of the sample, ω is the laser frequency, and α is the absorption coefficient. For light at 325 nm the absorption coefficient of PTR glass is about 0.7 cm^{-1}. Solving Equation 3.25 for the electron density gives a value of 4.5×10^{18} cm^{-3}. Our estimate of free-electron generation is almost one order of magnitude greater. Therefore ultrashort laser pulses are able to saturate the refractive index change in PTR glass. Finally it is important that we compare our value of free-electron density to the value of critical plasma density. In our experiment we did not observe effects associated with a critical plasma density (e.g. white-light plasma emission, laser-induced damage by plasma absorption). The critical plasma density in the Drude approximation is given by

$$N_{critical\ plasma} = \frac{\varepsilon_0 m_e}{e^2} \omega^2 . \tag{3.26}$$

At the wavelength 1550 nm (1.2 x 10^{15} rad/sec) the density of electrons required to reach the critical plasma level is 4.6 x 10^{20} cm^{-3}. Our free-electron density estimate is one order of magnitude below this value.

3.6 Comments on Laser-Induced Damage

It was seen that long exposure of glass to focused IR picosecond pulses led to optical damage. Figure 3.18 shows the morphology of this short pulse damage in fused silica. Small specks of damage can be seen along the filament path. The nature of this damage is not presently understood. On the other hand we can investigate the focusing geometry which led to filamentation but not damage for short exposure times.

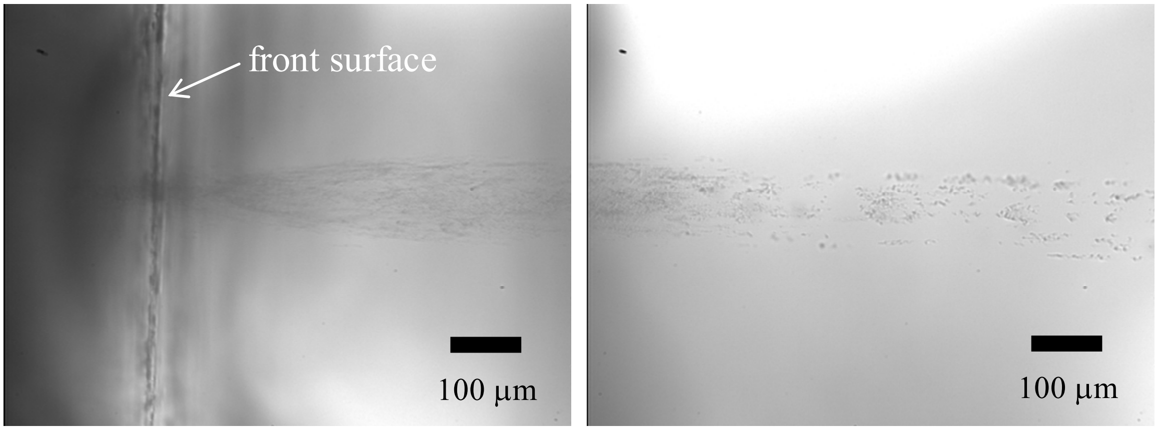

(a). (b).

Figure 3.18. Picosecond laser pulse damage in fused silica glass for long exposure times: (a) close to front surface (b) slightly after front surface.

It was seen that filamentation arises because of balancing between self-focusing and free electron defocusing. Let us consider what happens if self-focusing is prevented. It was shown in Ref. [35]

that self-focusing can be avoided by using a special focusing geometry. Figure 3.19 shows the geometry that was used.

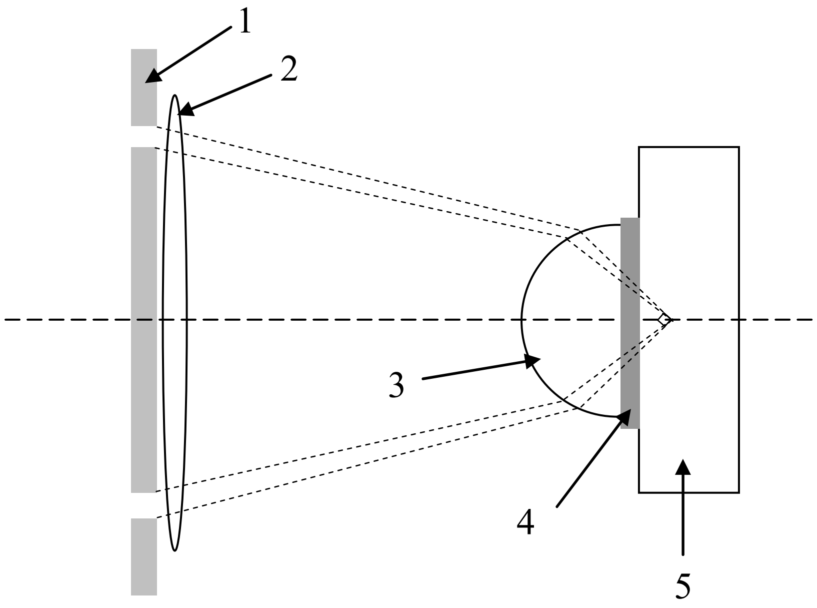

Figure 3.19. Scheme of orthogonal radiation focusing: (1) ring diaphragm (2) lens with relative aperture 1:1 (3) glass sphere (4) immersion layer (5) sample. From Ref. [35].

The result of this configuration was that geometrical focusing below the laser wavelength was obtained. However because an aperture was employed to create the ring-like pattern of irradiation significant energy was lost. We can attempt to avoid this loss in energy by changing the geometry and using a conical lens. In this case ring patterns are also formed as illustrated in Figure 3.20. A fused silica glass sample was tested using conical lens focusing of infrared picosecond laser pulses. Figure 3.21 shows the results. In all cases we did not observe red luminescence in the fused silica bulk because damage happened instantaneously and scattering by third harmonic was strong. This is due to the fact that geometrical focusing prevails over self-focusing and therefore a balance between nonlinear ionization and self-focusing did not occur, i.e. there was no condition to prevent a catastrophic increase in intensity. Thus to have nonlinear ionization in glass without laser-induced damage it is necessary to allow self-focusing to occur in the medium.

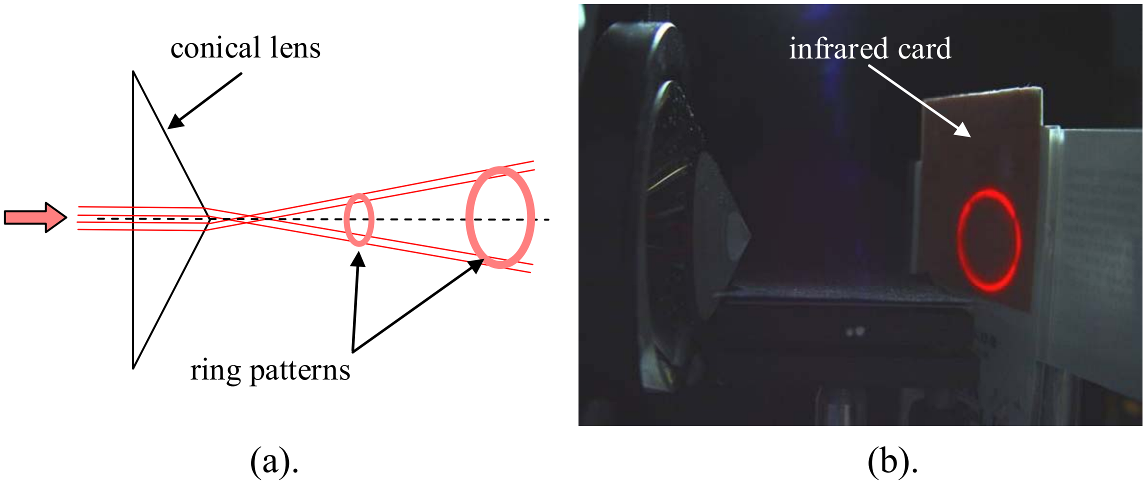

Figure 3.20. A conical lens used to convert collimated picosecond laser pulses into rings: (a) scheme of focusing (b) photograph from experiment.

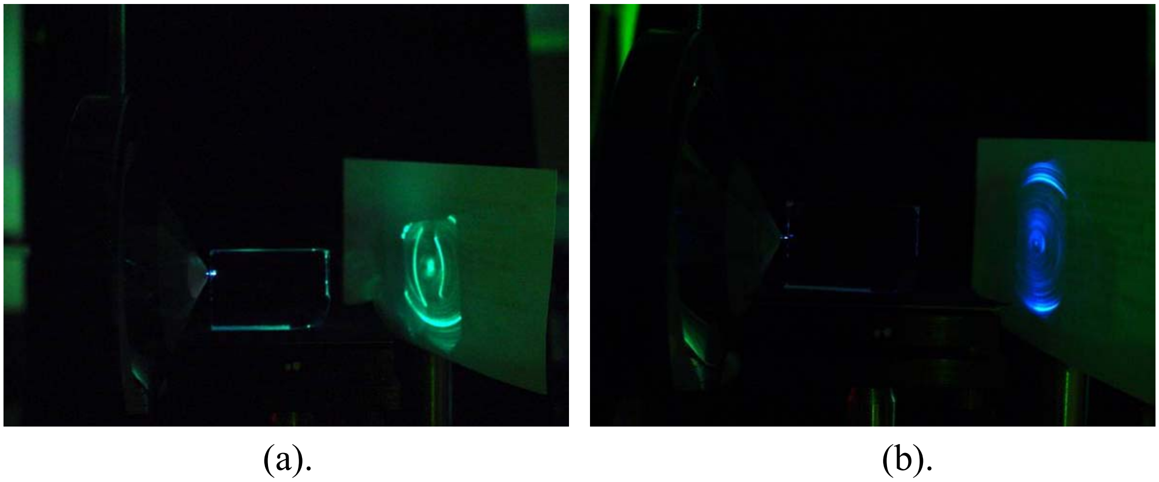

Figure 3.21. A conical lens is used to focus infrared picosecond pulses into fused silica glass: (a) pulses at 1550 nm (b) pulses at 1430 nm.

So far we have modeled photoionization in glasses and concluded that it can occur without optical breakdown when a balance between self-focusing and multiphoton ionization exists. A recent publication has remarked on the difference between optical damage and filamentation in glass [80]. In our experiments no single-shot damage occurred but over long exposure times (i.e. several tens of thousands of pulses) damage did occur. It is probable that the average excitation energy of the laser is transferred to the lattice over time and initiates the laser-induced damage at some critical point due to fatigue of the material.

3.7 Summary

We have used the Keldysh theory of nonlinear ionization to predict values of intensity and free-electron density that will stop self-focusing and form filaments in glass. Reasonable values for both intensity and free-electron density were obtained that agree with experiment. No instantaneous laser-induced optical damage was observed in the experiment. This theory explains the mechanism of nonlinear photosensitivity in PTR glass. In the next chapter we will use this phenomenon to record phase optical elements in PTR glass.

CHAPTER FOUR: PHASE ELEMENT RECORDING

Phase optical elements are attractive because they manipulate wave fields without absorbing energy. In this chapter we demonstrate the use of nonlinear photosensitivity to design and fabricate phase optical elements in PTR glass. It is important that modification of refractive index in PTR glass occurs by a two-step process. The first step is exposure to high-intensity infrared laser pulses. After this step no significant refractive index change occurs. This is in contrast to most methods of femtosecond laser processing of glass that rely on direct modification of the refractive index during exposure. There have been some published reports on the interaction of ultrashort laser pulses with photosensitive glasses [81, 82]. However a predictable and controllable change in refractive index change was not achieved. It is also important to avoid optical breakdown in glass because it will cause undesirable losses in the final optical element. The two-step photo-thermo-refractive process uses heat energy rather than laser energy to change the refractive index. Laser energy is only required for photoionization of electrons in PTR glass and subsequent trapping into silver photosensitivity sites. It is heat energy that causes the silver precursor sites to act as nucleation centers for nanocrystal growth which leads to a change in refractive index. A major advantage of PTR glass is that optical element recording by ultrashort laser pulses can be done below the laser-induced damage threshold.

4.1 Fresnel Lens

The dependence of refractive index change in PTR glass versus femtosecond laser intensity and dosage was described in Chapter 2. The refractive index change is sufficient for generating a π phase shift for optical light propagating through a sample of only a few millimeters. To demonstrate the applicability of recording phase elements in PTR glass by femtosecond laser exposure we chose to record a two-level linear phase Fresnel lens pattern [83]. A phase Fresnel lens is a diffractive element that behaves like a lens. Figure 4.1 shows the structure of this element and how it approximates a conventional lens. The two-level linear Fresnel lens we chose to fabricate consists of a series of linear zones with alternating zones of π phase shift. It behaves like a cylindrical lens.

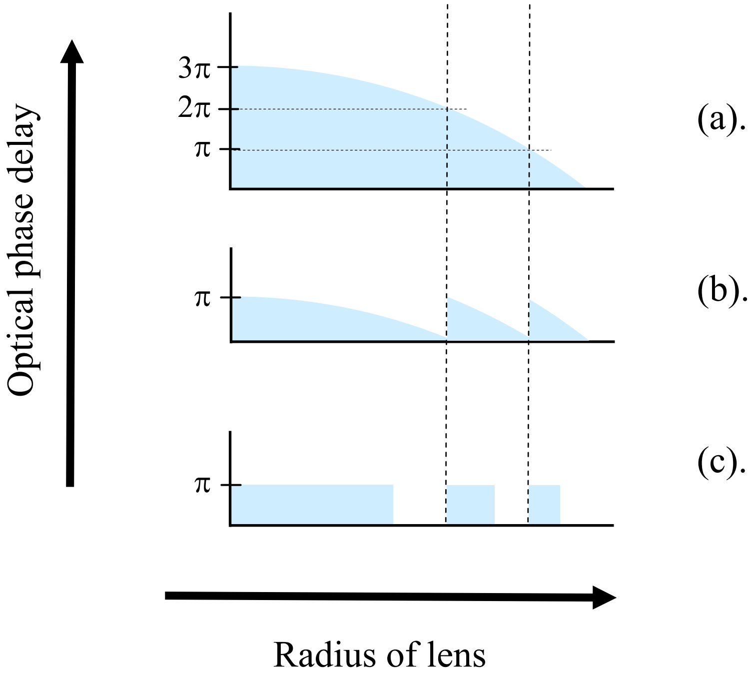

Figure 4.1. Phase profiles of a lens: (a) refractive surface (b) diffractive surface (phase Fresnel lens) (c) two-level approximation of a phase Fresnel lens.

In order to focus light of wavelength λ, the boundaries of the Fresnel zones are determined by

$$R_m = \sqrt{m\lambda f}, \tag{4.1}$$

where f is the desired focal length, m is an integer, and R_m determines the start or end of a zone. A Fresnel lens is symmetric about the central point $R_0 = 0$. The phase shift $\Delta\phi$ between adjacent zones for a two-level Fresnel lens of thickness L with refractive index change Δn between zones is given by

$$\Delta\phi = \frac{2\pi}{\lambda}\Delta n\, L, \tag{4.2}$$

For a PTR glass sample of thickness 1.6 mm and reconstruction at 632.8 nm the desired refractive index change for π phase shift is approximately 200 ppm. Due to its nonlinear nature, an important feature of PTR glass photosensitivity to IR femtosecond laser pulses is that the dependence of refractive index change versus exposure dosage is not identical for different exposure intensities. However at constant intensity, the refractive index change versus energy dosage follows a hyperbolic dependence and is therefore well controlled and predictable (see Figure 2.8). To achieve a refractive index change close to 200 ppm we chose to operate at an intensity of ~3 TW/cm^2 and at a dosage of ~100 J/cm^2. A Ti:sapphire regenerative amplifier generated femtosecond pulses with the following characteristics: pulse duration ~120 fsec, central wavelength 780 nm, repetition rate 1 kHz and energy per pulse up to 1 mJ. A spatial filter consisting of a telescope and a pinhole aperture was used to "cleanup" the beam and help avoid instabilities in mode shape which would lead to filament breakup during pulse propagation in the PTR glass sample. A positive lens with focal length equal to 1 m was used to focus the laser pulses. Knife-edge measurements were performed to determine the beam waist at the focal plane (~170 μm) and to confirm that the beam spot profile was close to Gaussian. A Glan polarizer was used to attenuate the energy per pulse and tune the intensity to the desired 3 TW/cm^2. A PTR glass sample was placed near the focal plane. Computer controlled translation stages were programmed to move the glass sample at a constant velocity during scanning and in the prescribed Fresnel lens pattern. To achieve the required dosage of 100 J/cm^2 the scanning velocity was calculated to be 0.5 mm/sec. The Fresnel lens pattern consisted of nine zones and was designed to focus light at 632.8 nm to a focal length of 400 cm. This design was chosen for demonstration because it does not require the recording of very narrow zones and therefore allows fabrication of a wide aperture (20 mm × 20 mm) element reasonably quickly (~15 minutes). With the development of spatial light modulators and tighter focusing, more complicated patterns can be recorded. Because the refractive index change in PTR is negative laser scanning was done between zone boundaries R_0-R_1, R_2-R_3, R_4-R_5, etc. After scanning the PTR glass sample was thermally developed for one hour at 515°C. The refractive index difference between the exposed and unexposed areas was measured by a shearing interferometer [59]. Figure 4.2(a) shows the measured refractive index difference for four zones of the fabricated Fresnel lens.

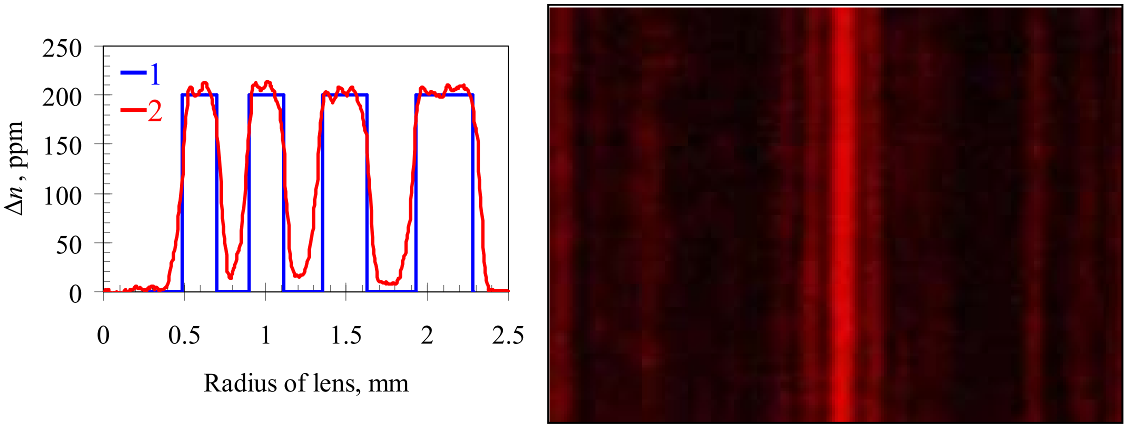

(a). (b).

Figure 4.2. Two-level phase Fresnel lens in PTR glass: (a) refractive index profile of four zones 1 – theory 2 – experiment (b) photograph of uniform collimated He-Ne laser light focused by the Fresnel lens.

The experiment shows that the index contrast between adjacent zones does not always reach the desired value. This can also be due to the limited lateral resolution of the shearing interferometer. Testing of the phase Fresnel lens in PTR glass was done using collimated He-Ne laser light at 633 nm from a Zygo interferometer. This light source provided a wide aperture of uniform and aberration free illumination. The PTR glass Fresnel lens was placed in the beam and the diffracted beam was observed at a distance 400 cm away from the element which corresponded to the designed focal length of the optical element. Figure 4.2(b) shows a photograph of the diffraction pattern at the focal plane and confirms that the element behaved as a cylindrical lens. The intensity profile of the Fresnel lens was measured using the knife-edge method. A sharp edge blade was translated across the focal plane while the transmitted power was continuously measured on an amplified silicon photodiode. First the Fresnel lens was removed from the setup and a knife-edge profile was taken to establish the reference power. Then the Fresnel lens element was positioned into the setup and the integrated power versus knife-edge position was measured. The ratio between the measurements with and without the Fresnel lens gives the integrated power profile which after differentiation gives the intensity profile, Figure 4.3. The theoretical diffraction efficiency for an *N*-level phase Fresnel lens is given by [84]

$$\eta = \frac{\sin^2(\pi/N)}{(\pi/N)^2}. \tag{4.3}$$

For a 2-level element the theoretical diffraction efficiency is ~40%. However, the diffraction efficiency of the phase Fresnel lens we fabricated reached almost 50%. This increase of efficiency can be easily explained by assuming that smooth, rather than sharp, refractive index zone boundaries were created. The resulting phase Fresnel lens was therefore not a strictly 2-level element anymore. To justify this hypothesis, we see from Equation 4.3 that even a 4-level Fresnel lens already gives a theoretical diffraction efficiency of 81.1%. In order to further increase the efficiency of the phase element, implementation of a multi-level Fresnel lens is possible in PTR glass. Different levels correspond to different changes in refractive index and refractive index change in PTR glass depends on dosage. A multi-level phase Fresnel lens could be implemented in PTR glass by changing the scanning velocity to achieve different dosages.

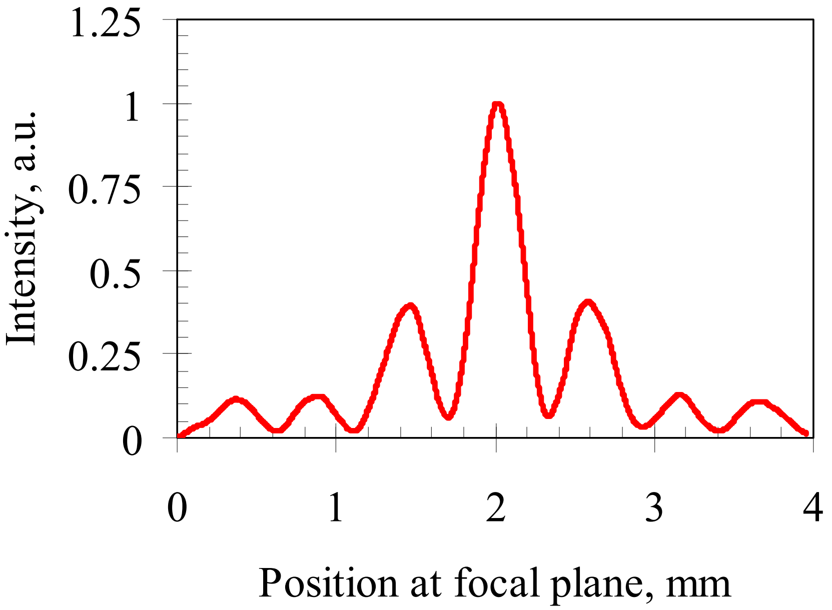

Figure 4.3. Intensity profile of the diffraction pattern generated by a phase Fresnel lens in PTR glass. Measurement at the focal plane.

4.2 Diffraction Gratings

We also looked at the fabrication of gratings by scanning ultrashort laser beam in PTR glass. Figure 4.4(a) shows grating patterns with different spatial periods recorded by exposure to 1550 nm picosecond pulses. Figure 4.4(b) shows that reconstruction by a laser was not perfect because filament breakup inside the glass caused a non-uniform index pattern throughout the glass thickness.

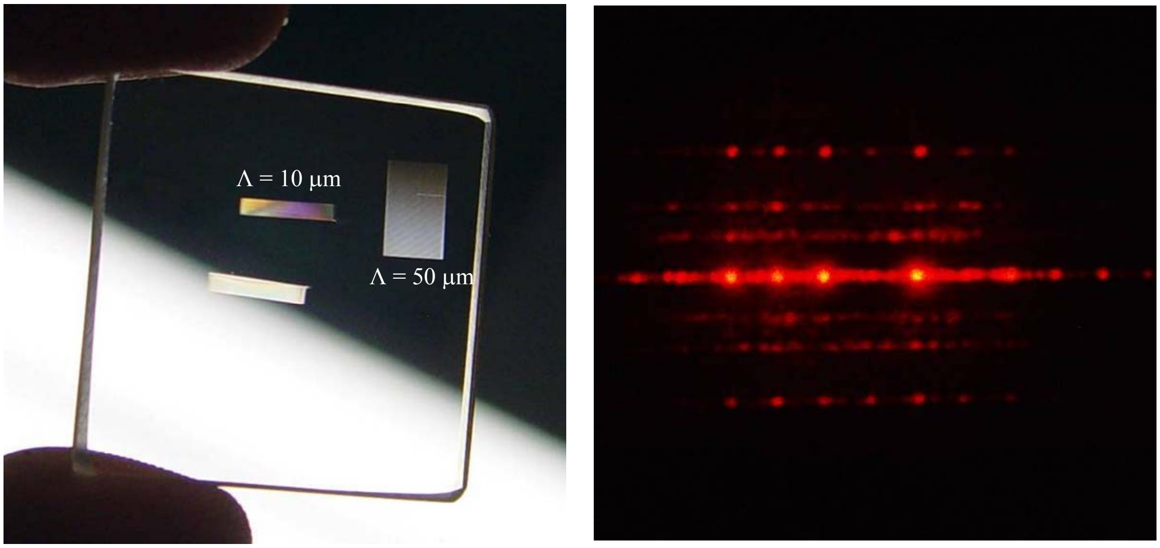

Figure 4.4. Gratings recorded in PTR glass by 1550 nm picosecond laser scanning: (a) photograph of sample illuminated by fluorescent lights (b) photograph of sample illuminated by He-Ne laser at 633 nm.

4.3 Holographic Optical Elements

A preliminary experiment with holographic recording in PTR glass by femtosecond laser pulses at 780 nm was performed. To record interference patterns a Mach-Zehnder interferometer was constructed, Figure 4.5. One of the main challenges of holographic recording with pulses is that before spatial fringes can be observed the interferometer has to be aligned for temporal overlap of the pulses. A convenient technique to check for temporal overlap of broad spectral width laser pulses is spectral interferometry. A fiber spectrometer is used to look at the spectrum of the pulses after exiting the interferometer setup. If the two pulses do not perfectly overlap in time the spectrometer displays fringes, Figure 4.6. To achieve perfect temporal overlap the delay line of one path is adjusted until spectral fringes can no longer be observed.

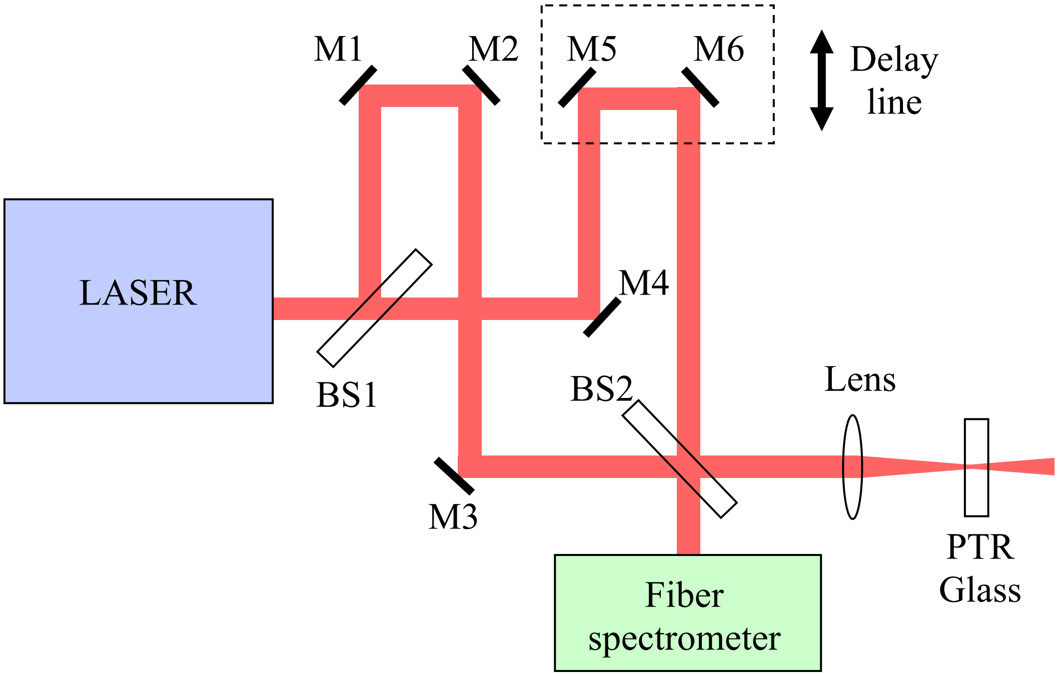

Figure 4.5. Mach-Zehnder interferometer for ultrashort laser pulse holography in PTR glass. M – mirror, BS – beam splitter.

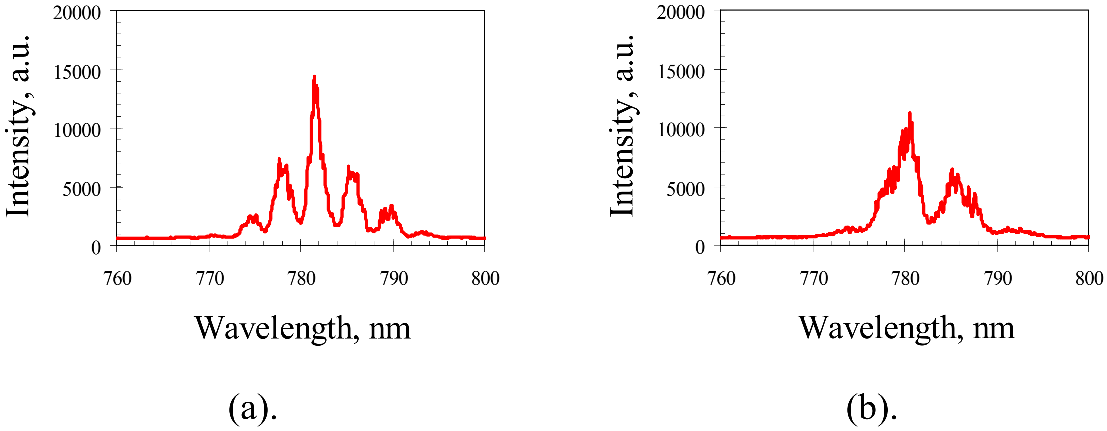

Figure 4.6. Spectral fringes for two pulses that are not perfectly overlapped in time: (a) long time delay (b) shorter time delay.

When temporal overlap of pulses is achieved it is possible to observe spatial fringes, Figure 4.7. By detuning one mirror it is possible to vary the spatial period of the fringes.

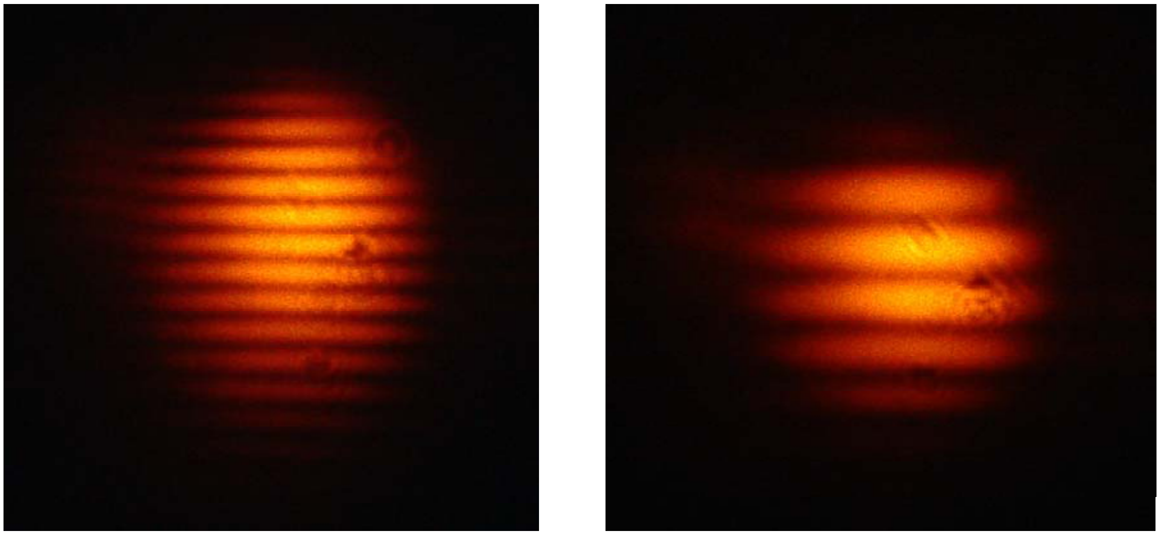
(a). (b).

Figure 4.7. Spatial fringes result from temporally overlapped pulses and non-collinear propagating paths: (a) more wavevector mismatch (b) less wavevector mismatch.

A spatial fringe interference pattern was focused into a PTR glass sample. The intensity of each of the two beam paths was adjusted so that if one beam was blocked no blue luminescence was observed in the PTR glass sample. However when the two beams were allowed to interfere blue luminescence was observed. In this manner holograms were recorded with exposure times less than one second (< 1000 pulses). The size of an individual hologram is on the order of tens of microns and difficult to measure afterwards. Therefore a translation stage was used to move the PTR glass sample and create an array of “point” holograms in a grid pattern. After exposure, the PTR glass sample was thermally developed for one hour at 515 ºC. Figure 4.8 shows reconstruction of the hologram array by a He-Ne laser at 633 nm. One interesting observation is that angular detuning of the sample caused energy coupling between adjacent points. Nevertheless such a structure is quite complex and beyond the scope of this thesis. Additional investigation into complex hologram recording in PTR glass with IR ultrashort laser pulses is required.

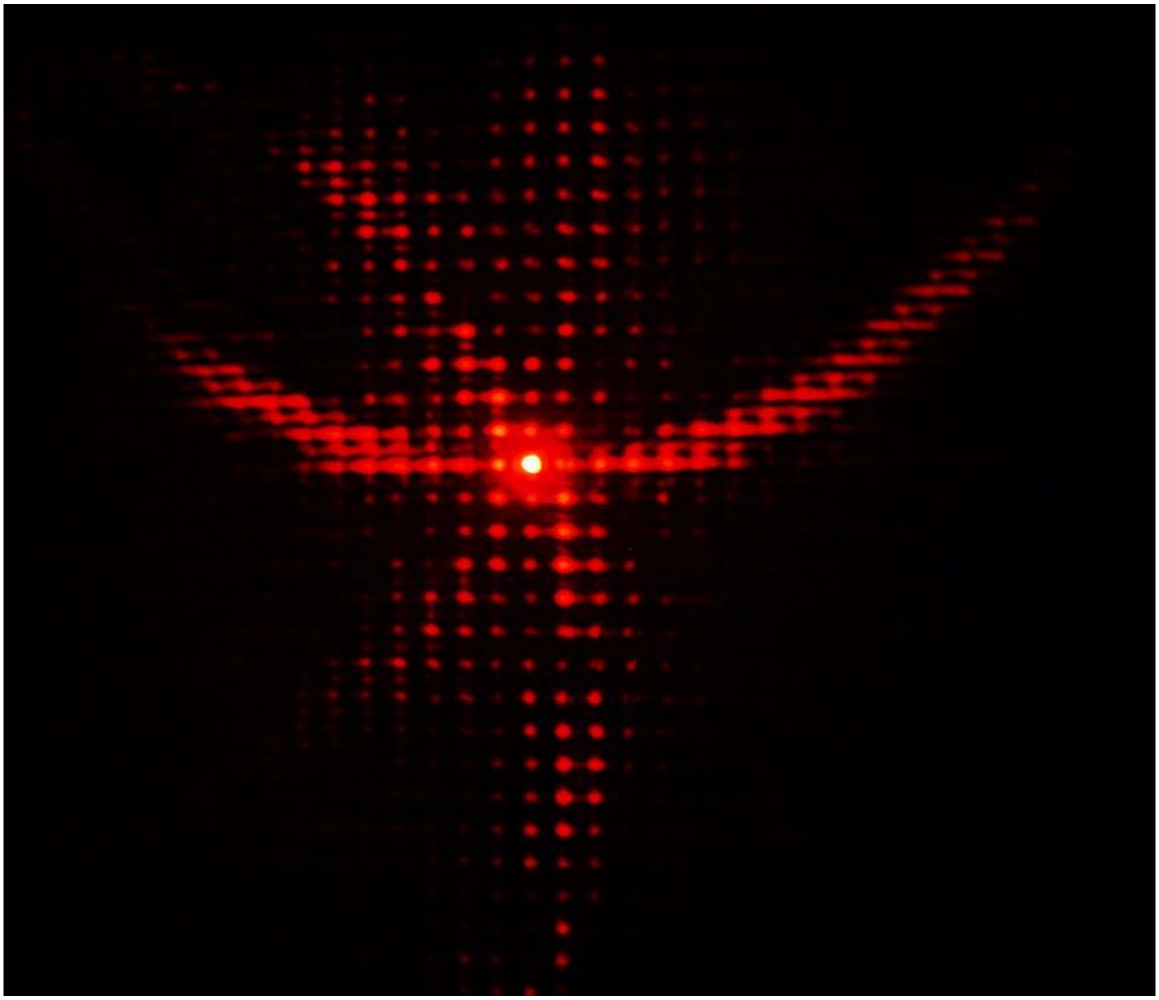

Figure 4.8. Reconstruction of an array of point holograms recorded in PTR glass by IR femtosecond pulses. Recording by femtosecond pulses at 780 nm, reconstruction by cw He-Ne laser at 633 nm.

4.4 Summary

A phase Fresnel lens in PTR glass was successfully designed and fabricated by IR femtosecond laser scanning. A measured diffraction efficiency of almost 50% was better than the theoretical limit for a two-level design but is consistent for an element with smooth zone boundaries. Apodized phase elements can be fabricated by modifying the scanning pattern to include variable scanning velocities. Tighter focusing of the laser beam would allow for an arbitrary 3D phase pattern to be fabricated in PTR glass. Grating patterns as well as initial results with hologram recording by IR femtosecond laser pulses were also demonstrated.

CHAPTER FIVE: LINEAR DIFFRACTION OF ULTRASHORT LASER PULSES BY VOLUME BRAGG GRATINGS

Volume Bragg gratings find many applications such as spectral beam combining and semiconductor laser stabilization where they are advantageous due to their spectral filtering properties. However when volume Bragg gratings are used with ultrashort pulse lasers some problems will arise. The Fourier transform relationship between time and frequency requires that an ultrashort laser pulse have a broad linewidth. In the case of femtosecond pulse generation by mode-locking the pulse is obtained from a coherent superposition of many longitudinal modes. Each mode has a slightly different frequency and a fixed phase relationship. The combination of these modes results in a broad spectrum. If an optical element affects the in-phase combination of modes then the pulse is distorted. In this chapter we investigate the performance of transmitting volume Bragg gratings in PTR glass by femtosecond pulse irradiation at intensities below ~10^{12} W/cm^2.

5.1 Diffraction Efficiency

The diffraction efficiency of volume Bragg gratings by plane wave cw laser light is well modeled using Kogelnik's coupled-wave analysis [see Appendix]. For unslanted TBGs the diffraction efficiency is given by

$$\eta(\lambda,\theta)=\frac{\sin^2\left\{\sqrt{\nu^2(\lambda,\theta)+\xi^2(\lambda,\theta)}\right\}}{1+\xi^2(\lambda,\theta)/\nu^2(\lambda,\theta)}. \tag{5.1}$$

where

$$\nu(\lambda,\theta) = \frac{\pi n_1 L}{\lambda \cos\theta}, \tag{5.2}$$

$$\xi(\lambda,\theta) = \frac{L}{2\cos\theta}\left[\mathrm{K}\sin\theta - \frac{\mathrm{K}^2\lambda}{4\pi\, n(\lambda)}\right], \tag{5.3}$$

$$\mathrm{K} = \frac{2\pi}{\Lambda}. \tag{5.4}$$

The parameters used in Equations 5.1-5.4 are wavelength λ, incident angle of light on grating θ, grating thickness L, amplitude of refractive index modulation n_1, refractive index as a function of wavelength $n(\lambda)$, grating vector K, and grating period Λ. Several TBGs with different parameters were recorded in PTR glass for testing with IR femtosecond pulse irradiation. Table 5.1 summarizes the different gratings and labels each grating with a different name.

Table 5.1. PTR glass TBGs. †Bragg angle and wavelength selectivity determined for central wavelength at 810 nm.

Grating name	Λ, µm	L, mm	n_1, ppm	θ_{Br}, deg†	$\Delta\lambda$, nm†
G1	5.97	2.15	200	3.9	33
G2	1	0.74	507	23.9	2.5
G3	5.54	2.06	200	4.2	30
G4	5.97	5.11	80	3.9	14

Femtosecond pulses were generated by a Ti:sapphire femtosecond laser system (pulsewidth ~150 fsec, central wavelength tunable from 760 nm to 840 nm, Gaussian spectral shape, repetition rate 80 MHz, energy per pulse on the order of 10 nJ). The diffraction efficiency of gratings G1 and G2 was measured with femtosecond pulses at 810 nm and compared to theory, Figure 5.1. For grating G1 the spectral selectivity of the grating was greater than the bandwidth of the femtosecond pulse and experiment and theory were in agreement, Figure 5.1(a). However, for grating G2 the spectral selectivity was less than the bandwidth of the laser and the diffraction efficiency decreased from Kogelnik's plane wave theory, Figure 5.1(b). To account for diffraction by a polychromatic beam it is necessary to perform a convolution between the diffraction efficiency of a monochromatic wave with the spectral distribution of the polychromatic beam [85]. For a Gaussian spectral distribution the new diffraction efficiency is given by

$$\eta(w,\theta)=\sqrt{\frac{2}{\pi}}\frac{1}{w}\int\eta(\lambda,\theta)\exp\left[-2\left(\frac{\lambda-\lambda_0}{w}\right)^2\right]d\lambda, \tag{5.5}$$

where w is the HWe^{-2}M spectral width, λ_0 is the central wavelength of the laser, and $\eta(\lambda,\theta)$ is determined from Equation 5.1. Using Equation 5.5 we were able to match the diffraction efficiency to the experimental result.

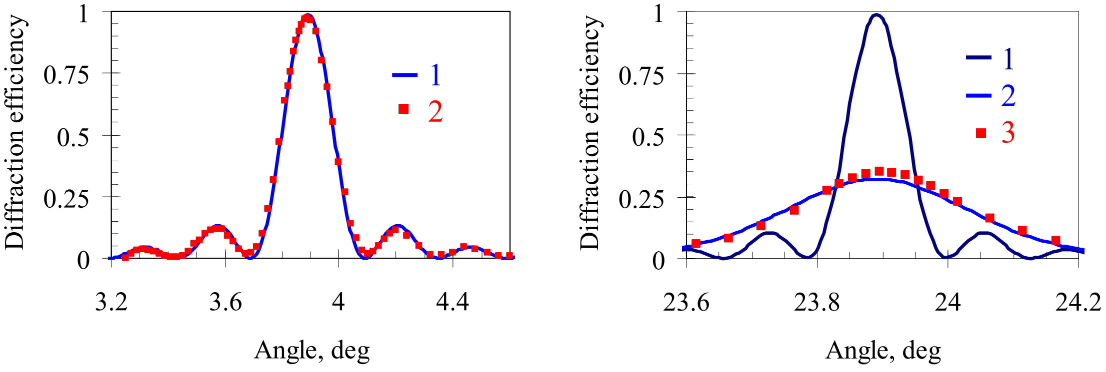

(a).

(b).

Figure 5.1. Diffraction efficiency of PTR glass gratings reconstructed by IR femtosecond pulses (~150 fsec, 810 nm, 6.4 nm bandwidth); (a) grating G1, 1 – plane wave modeling, 2 – experiment (b) grating G2, 1 – plane wave modeling, 2 – Gaussian wave modeling, 3 – experiment.

5.2 Angular Dispersion

For a given wavelength the angle of diffraction by an unslanted TBG is determined by Bragg's law

$$\theta(\lambda) = \sin^{-1}\left(\frac{\lambda}{2\Lambda}\right), \tag{5.6}$$

A TBG with wide spectral selectivity will efficiently diffract different wavelength components but at different angles. Experimental measurements of output diffraction angle versus wavelength for grating G3 were performed by tuning the central wavelength of the femtosecond laser and then rotating the grating to a new angle for maximum diffraction efficiency. Figure 5.2 compares the experimental results with the theoretical equation given by Equation 5.6. When grating G3 was set at a fixed angle (4.2° for maximum diffraction efficiency at 810 nm) we see from Figure 5.2 that many different wavelength components can be diffracted efficiently. The effect of this angular dispersion is that a collimated femtosecond beam incident on a TBG will diverge along one axis after diffraction. A simple way to see this effect is to focus the diffracted beam with a lens. At the focal plane a line, instead of a spot, is seen.

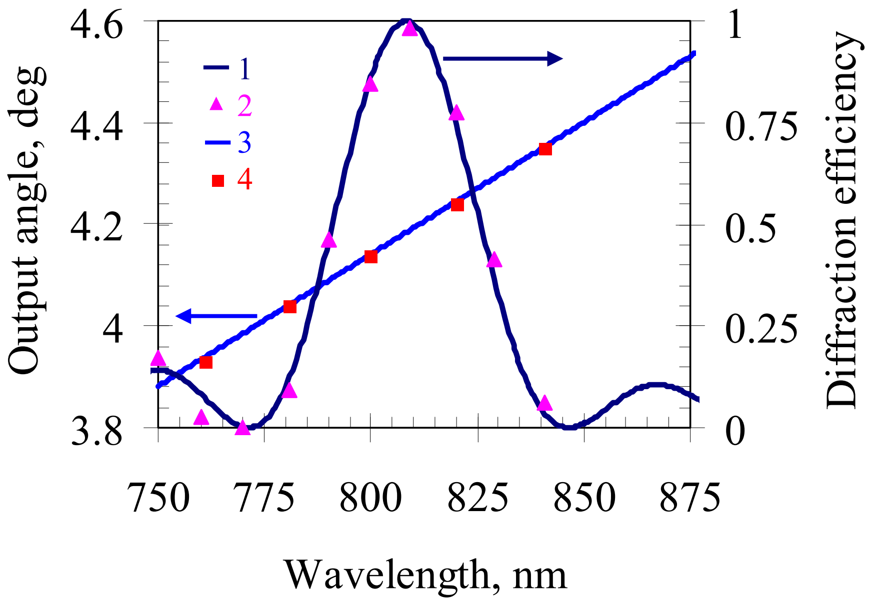

Figure 5.2. Diffraction efficiency and output angle dependence on central wavelength of femtosecond laser for grating G3 fixed at an angle of 4.2°. Diffraction efficiency versus wavelength, 1 – plane wave modeling, 2 – experiment. Output angle of diffracted beam versus wavelength, 3 – theory, 4 – experiment.

5.3 Pulse Front Tilt

It is known that diffraction of femtosecond pulses by surface transmitting gratings generates pulse front tilt [86]. PFT is a time delay across the transverse direction of the pulse due to the fact that the pulse front is no longer perpendicular to the propagation direction after diffraction. Figure 5.3(a) shows how a pulse acquires a tilt angle γ after diffraction. By calculating the delay Δ and knowing the beam diameter x the PFT is given by

$$\mathrm{PFT} = \frac{\Delta / c}{x} = \frac{(\mathrm{BC}+\mathrm{CD})/c}{x} = \frac{2\tan\theta}{c}, \tag{5.7}$$

where c is the speed of light. To measure the PFT of diffracted femtosecond pulses by TBGs in PTR glass we used spectral interferometry [87]. The SI technique relies on frequency-domain interference between two beams of different optical path. The number of interference fringes that are observed corresponds to the relative time delay between the two beams. Femtosecond pulses from a Ti:sapphire laser were split into two paths by a beam splitter. One path was used as a reference arm while the other path was diffracted by a TBG in PTR glass. The two paths were then recombined with a second beam splitter. Placing a slit in the diffracted beam path allowed us to look at different transverse parts of the diffracted pulse and determine the time delay from the resulting interferogram, Figure 5.3(a). The theoretical value of PFT for grating G1 is calculated by substituting $\theta = 3.9°$ into Equation 5.7 to give 0.45 psec/mm. Experimental measurements of the PFT for grating G1 were performed by displacing the slit position and measuring the time delay using SI, Figure 5.3(b). It is seen that the experimental data points fit on a line with slope 0.45 psec/mm. Thus PFT by TBGs in PTR glass obeys the classical relation given by Equation 5.7.

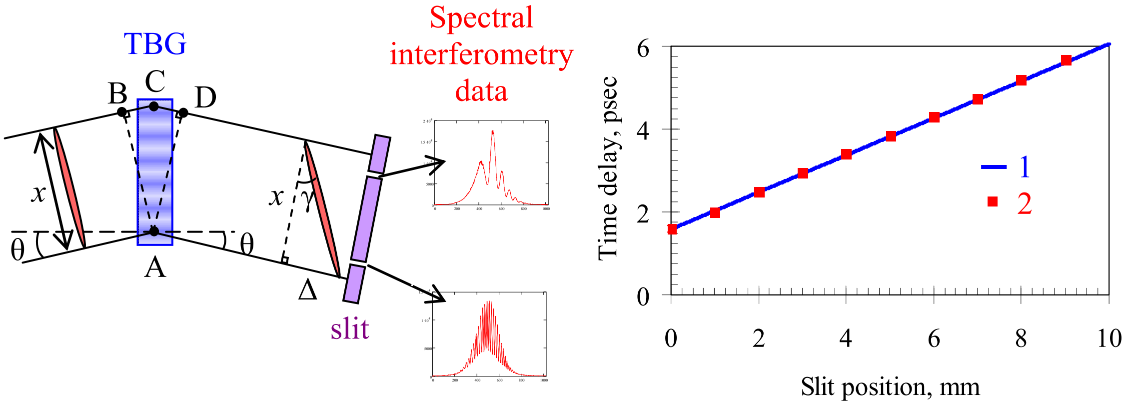

(a). (b).

Figure 5.3. Pulse front tilt of diffracted femtosecond pulses by a PTR glass grating: (a) geometrical optics scheme of PFT and method of spectral interferometry used to measure it (b) time delay versus slit position for grating G1, 1 – theory, 2 – experiment.

5.4 Grating Pair Arrangement

We also checked the performance of a two PTR glass volume gratings in the traditional grating pair arrangement. Surface grating pairs were first utilized by Treacy for pulse compression [88]. We first tested a single grating and then added a second grating to form the grating pair arrangement. Pulse analysis was done using FROG [89]. Figure 5.4 shows the experiment.

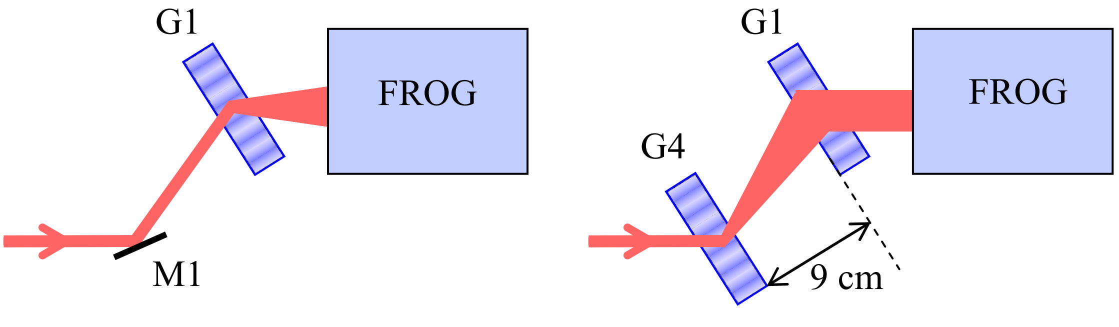

(a). (b).

Figure 5.4. Arrangement of PTR glass gratings for short pulse characterization by FROG: (a) single grating (b) grating pair. G – grating name, M – mirror. The divergence of the polychromatic laser beam after diffraction has been greatly exaggerated.

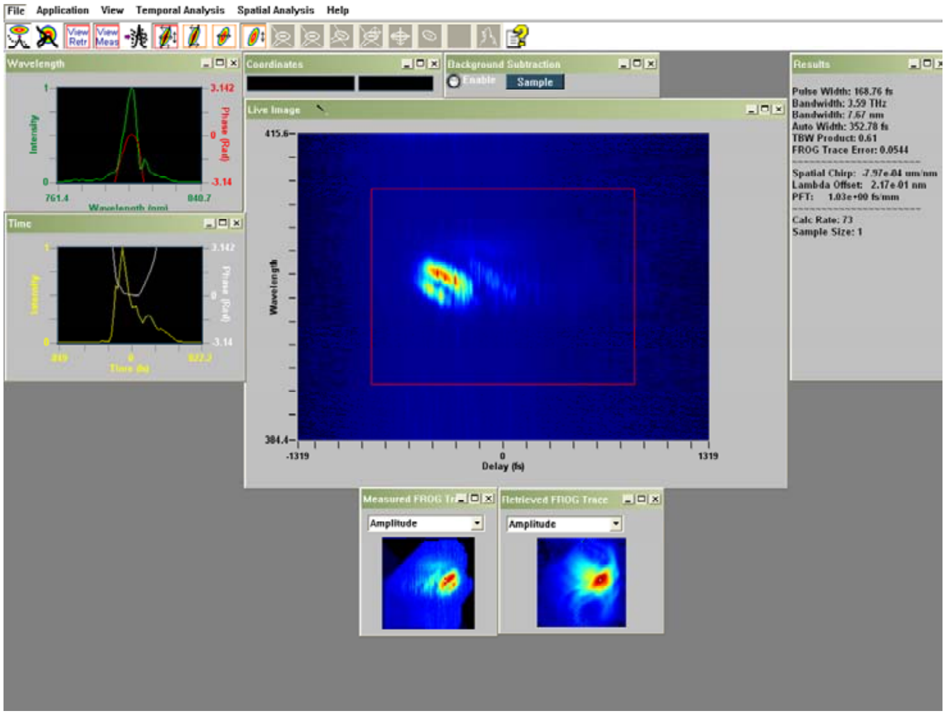

Pulse Width: 168.76 fs
Bandwidth: 3.59 THz
Bandwidth: 7.67 nm
Auto Width: 352.78 fs
TBW Product: 0.61
FROG Trace Error: 0.0544
Spatial Chirp: -7.97e-04 um/nm
Lambda Offset: 2.17e-01 nm
PFT: 1.03e+00 fs/mm
Calc Rate: 73
Sample Size: 1

(a).

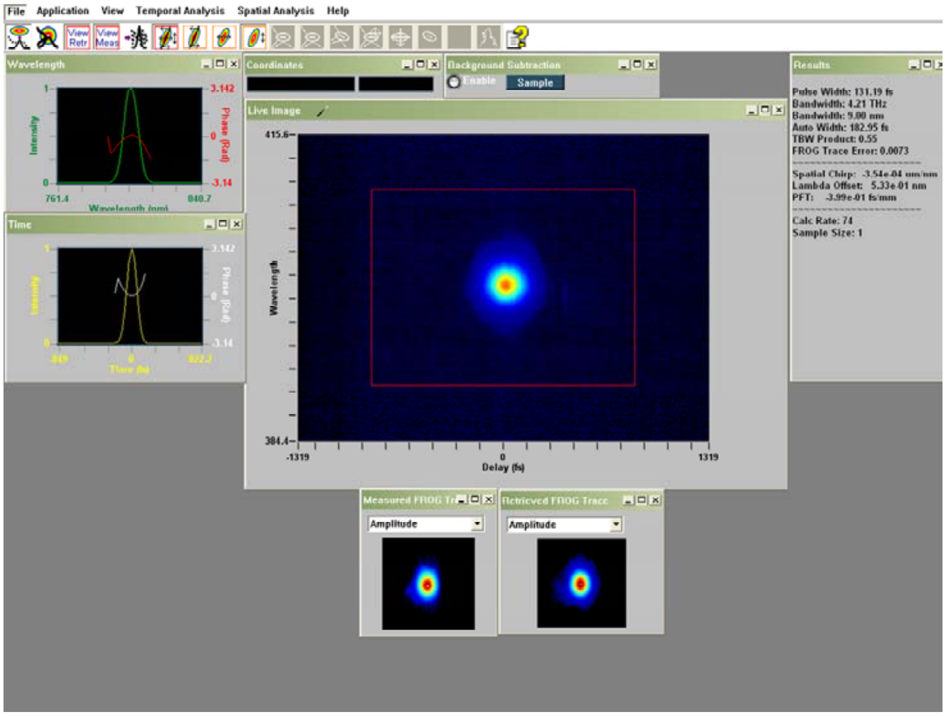

Pulse Width: 131.19 fs
Bandwidth: 4.21 THz
Bandwidth: 9.00 nm
Auto Width: 182.95 fs
TBW Product: 0.55
FROG Trace Error: 0.0073
Spatial Chirp: -3.54e-04 um/nm
Lambda Offset: 5.33e-01 nm
PFT: -3.99e-01 fs/mm
Calc Rate: 74
Sample Size: 1

(b).

Figure 5.5. Results of FROG analysis for: (a) single grating (b) grating pair. The pulsewidth of the laser source is 125 fsec.

The results from FROG analysis are shown in Figure 5.5. It can be seen that the pulse distortions from single volume grating diffraction (i.e. pulse front tilt, angular dispersion) are compensated for by the volume grating pair configuration. For theoretical calculations is it useful to consider the grating pair arrangement shown in Figure 5.6.

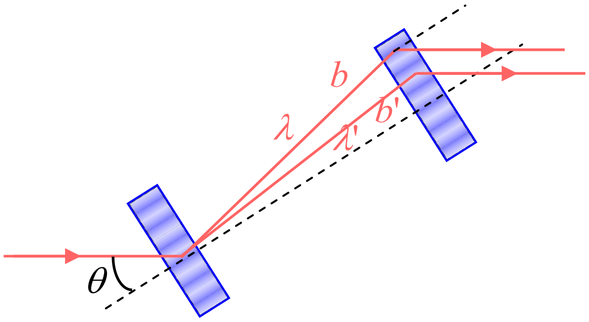

Figure 5.6. Geometrical arrangement of the TBG pair pulse compressor: b and b' – slant distances, θ – Bragg angle.

It was shown in Ref. [90] that transmitting Bragg gratings will lead to an identical result for the pulse compression factor as was derived by Treacy in his analysis of pulse compression using a pair of reflection gratings. The expression for variation of group delay with wavelength is

$$\frac{\Delta\tau}{\Delta\lambda}=\frac{b(\lambda/\Lambda)}{c\Lambda[1-(\lambda/\Lambda-\sin\theta)^2]}, \tag{5.8}$$

where b is the slant distance for laser wavelength λ, Λ is the grating period, c is the speed of light, and θ is the Bragg angle. For a PTR grating pair composed of gratings G1 and G4 we have Λ = 5.97 μm and θ = 3.9°. For the femtosecond laser at 810 nm the separation distance between gratings was set to 9 cm. The dispersive delay parameter $\Delta\tau/\Delta\lambda$ was calculated to be ~8 fsec/nm. In general this is an order of magnitude smaller than what is desired for compression. The reason is due to the large grating period (~6 μm). Unfortunately a smaller period volume grating acts as a spectral filter and does not diffract all wavelengths in the femtosecond pulse. Therefore TBGs in PTR glass are not useful for pulse compression because large compression ratios are unobtainable. However chirped Bragg gratings in PTR glass have shown remarkable success in compressing ultrashort laser pulses [91]. A different application for ultrashort laser pulse manipulation by TBGs can be considered. It is known that the angular selectivity of PTR glass TBGs make them useful for selection of a single transverse mode. We saw that the pulsewidth change with the TBG pair was insignificant (~5% increase). The spatio-temporal quality of the beam, as demonstrated in Figure 5.5(b), was also good. Furthermore, double pass propagation through a volume grating pair will correct spatial chirp which is inherent in single pass propagation through a volume grating pair. Therefore TBGs can be used in ultrafast laser systems as transverse mode selection elements without introducing significant amounts of pulsewidth broadening, spatio-temporal distortions, or energy losses.

5.5 Summary

In conclusion, we have shown that diffraction of femtosecond pulses by TBGs in PTR glass obey several classical equations. The diffraction efficiency was well modeled using a convolution between Kogelnik's plane wave diffraction efficiency for a monochromatic wave and the spectral distribution of the femtosecond beam. The diffracted beam diverges due to angular dispersion and was determined using Bragg's formula. The pulse front tilt of the diffracted beam obeys the classical result given by the accumulation of 2π phase jumps existing between two neighboring lines of a grating. A TBG grating pair was shown to have negligible effect for pulse compression but can be useful for transverse mode selection. These results show that TBGs in PTR glass perform as traditional optical gratings and because of their high damage threshold can be used in high power femtosecond laser systems. In the next chapter we study nonlinear effects of TBGs in PTR when the intensity of ultrashort pulses reaches ~10^{12} W/cm^2.

CHAPTER SIX: NONLINEAR DIFFRACTION OF ULTRASHORT LASER PULSES BY VOLUME BRAGG GRATINGS

Non-collinear third harmonic generation by a volume transmitting Bragg grating in PTR glass under high-intensity femtosecond pulse irradiation near 800 nm was first observed by Smirnov et al. when a TBG was placed at Bragg angle for the fundamental wavelength [92]. In addition to the expected transmitted and diffracted beams, two THG beams with propagation directions corresponding to the condition of sum-frequency generation were observed. However the phase matching condition for SFG was not satisfied. A possible explanation in terms of self-phase matching via Cherenkov radiation has been proposed [93]. One limitation of this experimental configuration is that the use of femtosecond pulses near 800 nm places THG in the ultraviolet regime and within the absorption region of PTR glass. This configuration prevents propagation of surface or bulk third harmonic inside the PTR glass and therefore does not allow for a complete study of the THG phenomena. Investigation of THG by a TBG in PTR glass at third harmonics within the transparency range of PTR glass requires fundamental pulses longer than 1000 nm. Therefore, this chapter discusses experiments dealing with THG by a TBG in PTR glass using femtosecond pulses at 1300 nm and 1588 nm. For this case third harmonics are centered at 433 nm and 529 nm and two new angular orientations of the TBG are shown to produce non-collinear third harmonic generation [94]. We provide theoretical explanations to account for these new angles. In one case phase-matching can arise due to interaction with a modulated nonlinear refractive index in PTR glass. Finally we consider the angular dependence of the intensity for the case of two-beam THG. Based on this data, we derive a theoretical model to predict the experimental behavior [95]. The model provides further support for a SFG interaction.

6.1 Experimental Observations

We used a Ti:sapphire regenerative amplifier laser system generating femtosecond pulses with the following parameters: pulsewidth ~120 fsec, repetition rate 1 kHz, central wavelength at 780 nm and pulse energies up to 1 mJ. The beam was focused by a lens with focal length equal to 1 m. An unslanted TBG with spatial period 4 µm, thickness 0.85 mm, and amplitude of refractive index modulation 467 ppm, was placed near the focal plane. Figure 6.1 shows the experimental arrangement.

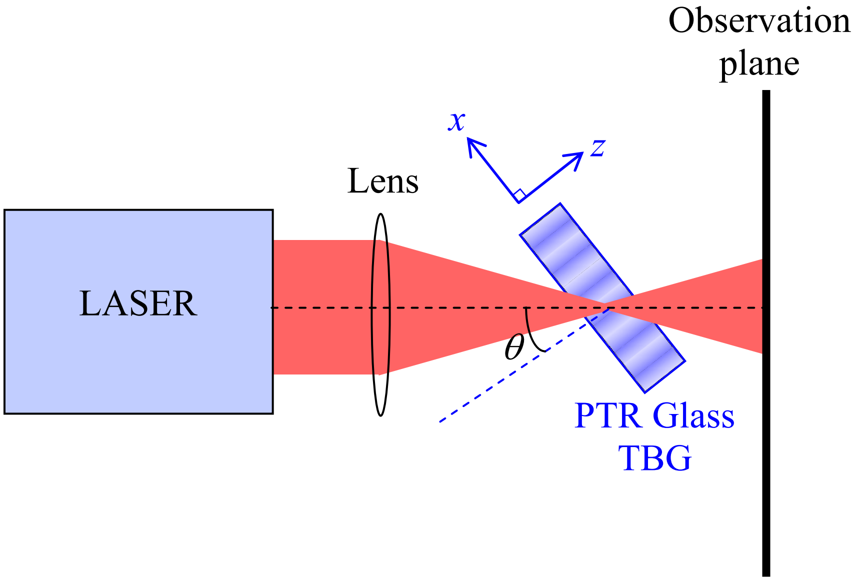

Figure 6.1. Experimental arrangement for investigating third harmonic generation and diffraction by transmitting Bragg gratings in PTR glass.

The angle θ of the TBG was set to Bragg angle for 780 nm and calculated according to Bragg's law

$$\sin\theta = \frac{\lambda}{2n(\lambda)\Lambda}, \tag{6.1}$$

where $n(\lambda)$ is the refractive index of PTR glass at wavelength λ. Figure 6.2 shows that after propagation through the TBG, two THG beams ($3\omega^{(i)}$ and $3\omega^{(ii)}$) appeared between the diffracted (ω_D)and transmitted (ω_T) beams. We call this configuration two-beam THG and distinguish the beams by labeling THG closest to the transmitted beam as $3\omega^{(i)}$ and THG closest to the diffracted beam as $3\omega^{(ii)}$. The beams appear blue on white paper because the ultraviolet photons cause luminescence of chemicals in the paper. A spectrometer confirmed that the beams were at 266 nm. Figure 6.2(b) shows that the direction of the two THG beams is determined by assuming a SFG interaction between transmitted and diffracted photons, i.e. two transmitted photons plus one diffracted photon or vice versa. For this grating spatial period (4 μm) and wavelength of irradiation (780 nm) no other angles were observed to generate non-collinear THG.

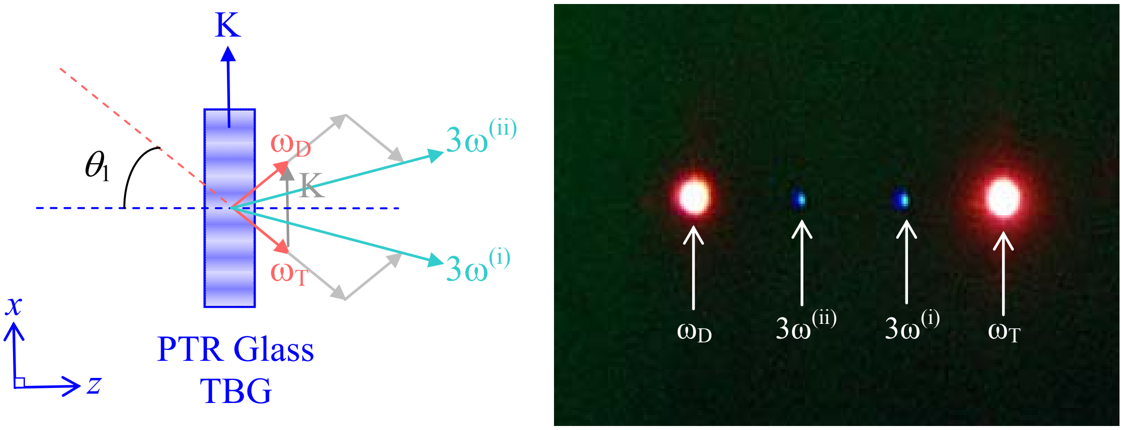

(a). (b).

Figure 6.2. Two-beam THG by a PTR glass TBG illuminated with IR femtosecond pulses: (a) wavevector additions of transmitted and diffracted photons to produce third harmonic (b) photograph from experiment. K – grating vector, ω_T – transmitted photon, ω_D –diffracted photon. Phase-matching is not satisfied.

The wavelength dependence of THG was tested with an optical parametric amplifier (OPA) laser system (pulsewidth <200 fsec, pulse energies up to 0.1 mJ, and repetition rate at 1 kHz) that generated femtosecond pulses at 1300 nm and 1588 nm. Long focal lenses focused the femtosecond beam in order to achieve intensity at the focal point of about 10^{12} W/cm^2. A TBG in PTR glass with 4 μm spatial period, 0.97 mm thickness, and amplitude of refractive index modulation of 607 ppm was placed near the focal plane. The angles of the TBG at which non-collinear THG was generated were measured and given in Table 6.1.

Table 6.1. Measured angles for non-collinear THG by a TBG in PTR glass ($\Lambda = 4$ μm, $z = 0.97$ mm, $n_1 = 607$ ppm). Accuracy of angular measurements ±0.5°.

Angle	$\lambda = 1300$ nm	$\lambda = 1588$ nm
θ_1	9.8°	11.5°
θ_2	3.5°	3.4°
θ_3	14.8°	7.7°
$-\theta_3$	-14.3°	-8.3°
$-\theta_2$	-2.9°	-3.9°
$-\theta_1$	-9.6°	-11.8°

At the wavelengths 1300 nm and 1588 nm it was again observed that for the TBG oriented at Bragg angle for fundamental, two THG beams appeared between the transmitted and diffracted beams. We will designate the Bragg angle for fundamental as θ_1. In addition to THG at θ_1 two other angles also resulted in non-collinear generation of third harmonic. These two interactions are illustrated in Figure 6.3 along with the assumed wavevector conditions responsible for their generation. At angle θ_2, THG is attributed to Bragg diffraction for incident light at wavelength $\lambda/3$. This interaction is likely due to generation of third harmonic at the front interface of the glass grating and subsequent diffraction. This phenomenon could not be seen with fundamental pulses at 780 nm because of absorption of 266 nm light in the bulk of PTR glass after generation by the front surface. We designate THG at angle θ_2 as surface diffracted THG. The appearance of THG at angle θ_3 represents a non-Bragg resonance condition where three fundamental photons interact with a grating vector to generate the third harmonic. We label the THG process at angle θ_3 as generation and diffraction by a nonlinear grating. In the next section we impose phase-matching on the three assumed wavevector interactions and derive theoretical values for the angles at which THG is expected. A comparison of these theoretical values is then done with the experimentally measured values of Table 6.1.

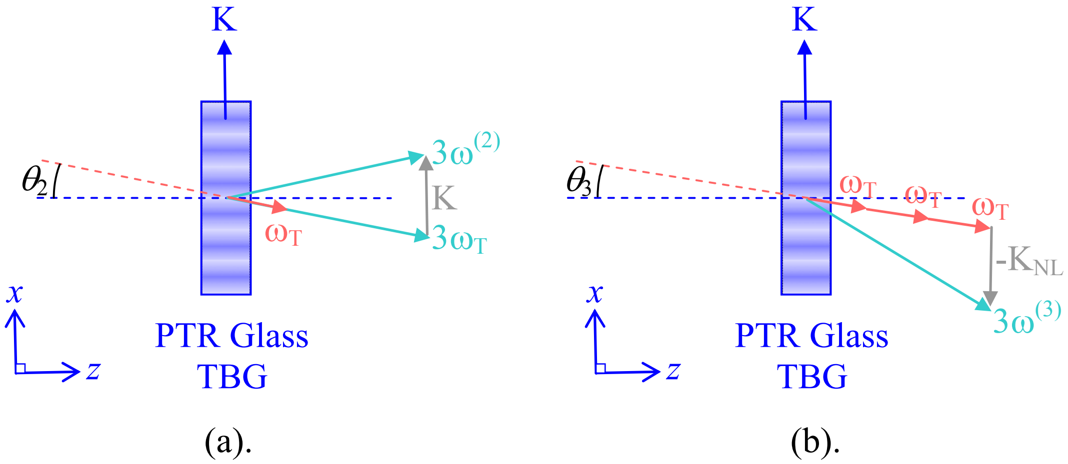

Figure 6.3. Wavevector conditions for non-collinear THG by a PTR glass TBG: (a) front surface diffracted THG (b) generation and diffraction by a nonlinear grating. K_{NL} – nonlinear grating vector.

6.2 Phase-Matching Conditions

There are three interactions with a TBG in PTR glass that exhibit non-collinear THG under high-intensity femtosecond irradiation. For the two-beam THG interaction shown in Figure 6.2(b) the assumed SFG wavevector equations can be written as

$$\mathbf{k}_{3\omega^{(i)}} = 2\mathbf{k}_{\mathrm{T}}(\lambda,\theta) + \mathbf{k}_{\mathrm{D}}(\lambda,\theta), \tag{6.2}$$

$$\mathbf{k}_{3\omega^{(ii)}} = \mathbf{k}_{\mathrm{T}}(\lambda,\theta) + 2\mathbf{k}_{\mathrm{D}}(\lambda,\theta), \tag{6.3}$$

where the transmitted wavevector $\mathbf{k}_{\mathrm{T}}(\lambda,\theta)$and the diffracted wavevector $\mathbf{k}_{\mathrm{D}}(\lambda,\theta)$ are given by

$$\mathbf{k}_{\mathrm{T}}(\lambda,\theta) = \mathbf{k}(\lambda,\theta), \tag{6.4}$$

$$\mathbf{k}_{\mathrm{D}}(\lambda,\theta) = \mathbf{k}(\lambda,\theta) + \mathbf{K}, \tag{6.5}$$

and the incident wavevector $\mathbf{k}(\lambda,\theta)$ and grating vector $\mathbf{K}$ are

$$\mathbf{k}(\lambda,\theta) = \frac{2\pi}{\lambda} n(\lambda)\left[\sin\theta\,\hat{\mathbf{x}} + \cos\theta\,\hat{\mathbf{z}}\right], \tag{6.6}$$

$$\mathbf{K} = \frac{2\pi}{\Lambda}\hat{\mathbf{x}}. \tag{6.7}$$

The refractive index of PTR glass as a function of wavelength is given by a Cauchy fit of the form

$$n(\lambda) = \sqrt{\mathrm{A} + \mathrm{B}\lambda^2 + \mathrm{C}\lambda^{-2} + \mathrm{D}\lambda^{-4} + \mathrm{E}\lambda^{-6} + \mathrm{F}\lambda^{-8}}, \tag{6.8}$$

where λ is expressed in microns and the values of A, B, C, D, E and F are given in Table 6.2.

Table 6.2. Cauchy coefficients for PTR glass.

Coefficient	Value	Units
A	2.20959×10^{0}	
B	-9.71400×10^{-3}	μm^{-2}
C	9.99400×10^{-3}	μm^{2}
D	1.37070×10^{-4}	μm^{4}
E	-2.40635×10^{-6}	μm^{6}
F	-2.96604×10^{-7}	μm^{8}

In order for the wavevectors given by Equations 6.2 & 6.3 to be phase-matched their magnitude must equal the magnitude of a third harmonic wavevector, i.e.

$$k_{3\omega} = k(\lambda/3,\theta) = 3\left(\frac{2\pi}{\lambda}\right)n(\lambda). \tag{6.9}$$

However, when the laser and grating parameters used to generate the THG beams seen in Figure 6.1(b) are substituted into Equation 6.9 we have a mismatch. In general there will always be a mismatch. This suggests that the SFG assumption which Equations 6.2 & 6.3 represent is wrong. Nevertheless the SFG assumption proves useful for studying the intensity dependence of the two THG beams as a function of angle as will be shown in the next section. For now let us continue to analyze the phase-matching conditions and look at the other two cases where THG was observed. To check phase-matching for the wavevector interactions at angle θ_2 and θ_3 we write

$$\mathbf{k}_{3\omega^{(2)}} = \mathbf{k}(\lambda/3, \theta) + \mathbf{K}, \tag{6.10}$$

$$\mathbf{k}_{3\omega^{(3)}} = 3\mathbf{k}(\lambda, \theta) + \mathbf{K}_{\mathrm{NL}}. \tag{6.11}$$

Equation 6.10 relates to the case seen in Figure 6.3(a) and Equation 6.11 relates to the case seen in Figure 6.3(b). The angle θ in each of the above wavevector equations is solved for by imposing the phase-matching condition given by Equation 6.9. The grating vectors $\mathbf{K}$ and $\mathbf{K}_{\mathrm{NL}}$ are both evaluated using Equation 6.7. We label the angles that satisfy Equations 6.10 & 6.11 as θ_2 and θ_3 respectively. The resulting solutions are for angles inside a medium of refractive index n and are converted to angles in air by Snell's law

$$\theta = \sin^{-1}\left[n \sin \theta_{\mathrm{media}}\right]. \tag{6.12}$$

Table 6.3 shows that the theoretical angles agree with the experimentally measured values. Also, the theory is able to account for the large change in angle θ_3 as the wavelength changed from 1300 nm to 1588 nm. Hence we have justified the assumed wavevector equations given by Equations 6.10 & 6.11.

Table 6.3. Theoretically derived and experimentally measured angles of grating orientation to obtain non-collinear THG for a PTR glass TBG ($\Lambda = 4$ µm, $L = 0.97$ mm, $n_1 = 607$ ppm).

Angle	$\lambda = 1300$ nm		$\lambda = 1588$ nm	
	experiment	*theory*	*experiment*	*theory*
θ_1	9.8°	9.36°	11.5°	11.45°
θ_2	3.5°	3.1°	3.4°	3.8°
θ_3	14.8°	14.4°	7.7°	8.2°
$-\theta_3$	-14.3°	-14.4°	-8.3°	-8.2°
$-\theta_2$	-2.9°	-3.1°	-3.9°	-3.8°
$-\theta_1$	-9.6°	-9.36°	-11.8°	-11.45°

6.3 Angular Selectivity of Two-beam THG

It was seen in the last section that phase-matching assuming SFG is not satisfied for the two-beam THG condition at angle θ_1. Let us see if we can support an SFG interaction by measuring the angular selectivity of the two THG beams. Angular detuning from Bragg condition affects the relative intensities of transmitted and diffracted beams. Therefore, if THG is a result of interaction between transmitted and diffracted photons, the intensities of the THG beams will be affected differently. A Ti:sapphire regenerative amplifier laser system operating at 780 nm, ~120 fsec, 1 kHz, and pulse energies up to 1 mJ was used with a TBG with the following parameters: $\Lambda = 4$ μm, $L = 0.85$ mm, $n_1 = 467$ ppm. A computer controlled rotation stage controlled the angle of the TBG while an amplified GaP photodetector measured the intensity of THG. Due to the bandwidth sensitivity of the detector, no light was detected from transmitted or scattered fundamental radiation, and only radiation from THG was detected. Figure 6.4 shows the experimentally obtained angular selectivity profiles for the two THG beams. It is evident that the $3\omega^{(i)}$ and $3\omega^{(ii)}$ beams shows different angular dependencies. To model the angular selectivity of third harmonic generation for the two-beam THG case let us assume SFG interactions. We can then write the intensity of THG for each of the beams as

$$I_{3\omega^{(i)}} = \kappa I_{\omega_T} I_{\omega_T} I_{\omega_D}, \tag{6.13}$$

$$I_{3\omega^{(ii)}} = \kappa I_{\omega_D} I_{\omega_D} I_{\omega_T}, \tag{6.14}$$

where κ is a constant, $I_{\omega T}$ is the intensity of the transmitted beam and $I_{\omega D}$ is the intensity of the diffracted beam. Assuming that the spectral selectivity of the TBG is larger than the bandwidth of the laser it is possible to neglect the integration between the spectral profile of the beam and the diffraction efficiency of the TBG.

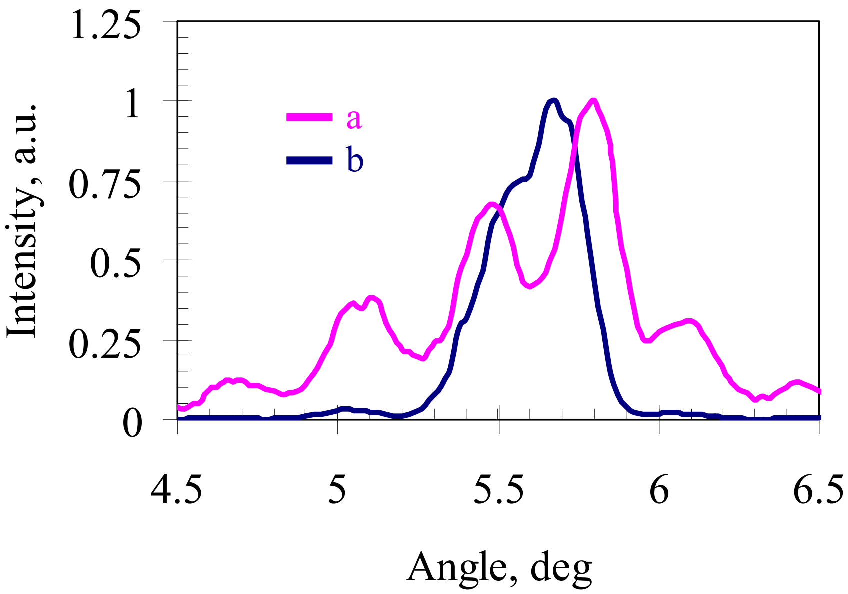

Figure 6.4. Dependence of third harmonic intensity from PTR glass TBG on incident angle for (a) $3\omega^{(i)}$ beam (b) $3\omega^{(ii)}$ beam.

When the grating selectivity is greater than the laser spectral bandwidth the intensity of the diffracted and transmitted beams can be written as

$$I_{\omega_D} = I_0 \eta(\theta), \tag{6.15}$$

$$I_{\omega_T} = 1 - I_{\omega_D}, \tag{6.16}$$

where I_0 is the incident intensity and $\eta(\theta)$ is the diffraction efficiency of the TBG as a function of incident angle θ. The diffraction efficiency for an unslanted TBG at resonant frequency is

$$\eta(\theta) = \frac{\sin^2\left\{\sqrt{\nu^2(\theta) + \xi^2(\theta)}\right\}}{1 + \xi^2(\theta)/\nu^2(\theta)}, \tag{6.17}$$

where

$$\nu(\theta) = \frac{\pi n_1 z}{\lambda \cos\theta}, \tag{6.18}$$

$$\xi(\theta) = \frac{z}{2\cos\theta}\left[\mathrm{K}\sin\theta - \frac{\mathrm{K}^2 \lambda}{4\pi n(\lambda)}\right]. \tag{6.19}$$

We multiplied Equation 6.17 by a constant factor of 0.7 because the maximum experimental diffraction efficiency did not reach 100% as predicted theoretically due to a limited interaction distance in the TBG and divergence of the beam resulting in integration of the diffraction efficiency over several incidences [85]. We then solved for the theoretical THG intensities, Equations 6.13 & 6.14. Figure 6.5 shows how the theoretical solutions compare to the experimentally measured THG intensities. It is seen that the theoretical model produces angular profiles for $3\omega^{(i)}$ and $3\omega^{(ii)}$ that account for the main intensity fluctuations seen in the experimental measurements. Lobe maxima and minima are in agreement for both experiment and theory. The model however does not predict the asymmetry seen in the experimental measurements. This asymmetry is likely a consequence of the asymmetry of the fundamental pulse spectrum shown in Figure 6.6.

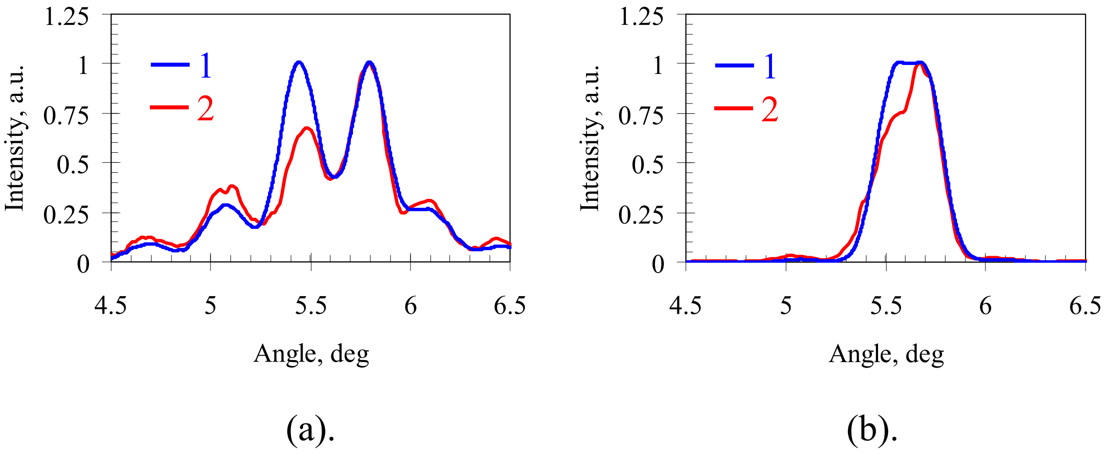

Figure 6.5. Dependence of third harmonic intensity on incident angle for the two-beam THG case: (a) $3\omega^{(i)}$ beam (b) $3\omega^{(ii)}$ beam. 1 – theory 2 – experiment.

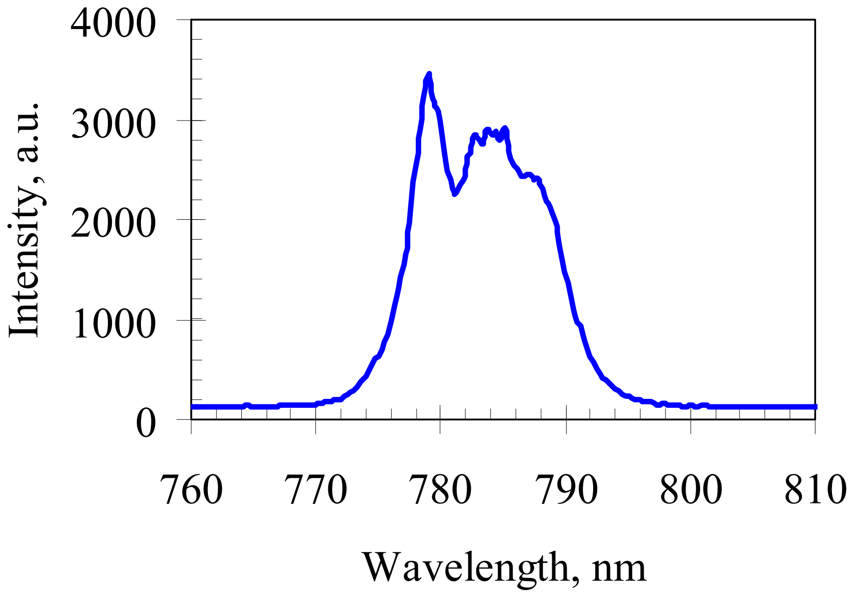

Figure 6.6. Spectrum of femtosecond pulse shows an asymmetric profile.

6.4 Nonlinear Refractive Index Grating

The resonant process assumed in Equation 6.11 that determines the angle θ_3 and generates THG requires three fundamental photons to interact with a grating vector. This is a χ_3 process and no interaction can occur with the linear grating vector of the TBG recorded inside PTR glass. Therefore the interaction occurs between the incident wavevectors and a grating vector arising from the nonlinear contribution of χ_3. This is possible if we assume that modulation in χ_3 occurs concurrently with modulation in the linear refractive index. The nonlinear susceptibility can then be written as

$$\chi_3 = \chi_3^{(0)} + \delta\chi_3^{(0)} e^{i\mathbf{K}_{\mathrm{NL}}\cdot\mathbf{r}}, \tag{6.20}$$

showing a static part and a modulated part that depends on the nonlinear grating vector $\mathbf{K}_{\mathrm{NL}}$. Using a Green's formulation [96] to solve the nonlinear wave equation gives a solution of the form

$$\mathbf{E}_{3\omega} \propto \iiint e^{i\mathbf{k}_{3\omega}\cdot\mathbf{r}} \mathbf{P}_{3\omega} d^3 r, \tag{6.21}$$

where

$$\mathbf{P}_{3\omega} = \chi_3 \mathbf{E}_1 \mathbf{E}_2 \mathbf{E}_3. \tag{6.22}$$

For the case of angle θ_3 with three incident fundamental photons we can write the electric fields as

$$\mathbf{E}_1 = \mathbf{E}_2 = \mathbf{E}_3 = \mathbf{E}_0 e^{-i\mathbf{k}_{\omega}\cdot\mathbf{r}}, \tag{6.23}$$

and after substitution into Equation 6.22 we arrive at

$$\mathbf{E}_3 \propto \int_V \chi_3^{(0)} E_0^3 e^{i\left(\mathbf{k}_{3\omega}\cdot\mathbf{r}\text{-}3\mathbf{k}_{\omega}\cdot\mathbf{r}\right)} d^3 r + \int_V \delta\chi_3 E_0^3 e^{i\left(\mathbf{k}_{3\omega}\cdot\mathbf{r}\text{-}3\mathbf{k}_{\omega}\cdot\mathbf{r}+\mathbf{K}_{\mathrm{NL}}\cdot\mathbf{r}\right)} d^3 r. \tag{6.24}$$

In order for phase-matching to occur the argument of the exponentials must go to zero. In the first integral this is not possible because of PTR glass dispersion. However, in the second integral the nonlinear grating vector can compensate for dispersion mismatch and we have the condition

$$\mathbf{k}_{3\omega}\cdot\mathbf{r}\,\text{-}\,3\mathbf{k}_{\omega}\cdot\mathbf{r} + \mathbf{K}_{\mathrm{NL}}\cdot\mathbf{r} = 0. \tag{6.25}$$

Since we expect that the change in nonlinear refractive index follows the change in linear refractive index we equate $\mathbf{K}_{\mathrm{NL}}$ with $\mathbf{K}$. In this case Equation 6.25 is equivalent to Equation 6.11. Thus the THG condition given by Equation 6.11 can be justified by assuming a nonlinear grating arising from modulation in χ_3 in PTR glass. The change in χ_3 occurs concurrently with the change in linear refractive index and therefore the spatial period of the nonlinear grating is the same as the spatial period of the linear grating. It is also possible to formulate the SFG interaction from Equation 6.21. For example to derive Equation 6.2 we write the electric fields as

$$\mathbf{E}_1 = \mathbf{E}_2 = \mathbf{E}_0 e^{-i\mathbf{k}_{\mathrm{T}}\cdot\mathbf{r}}, \tag{6.26}$$

$$\mathbf{E}_3 = \mathbf{E}_0 e^{-i\mathbf{k}_{\mathrm{D}}\cdot\mathbf{r}}. \tag{6.27}$$

Then after substitution into Equations 6.22 & 6.21 we have

$$\mathbf{E}_3 \propto \int_V \chi_3^{(0)} E_0^3 e^{i\left(\mathbf{k}_{3\omega}\cdot\mathbf{r}-2\mathbf{k}_\mathrm{T}\cdot\mathbf{r}-\mathbf{k}_\mathrm{D}\cdot\mathbf{r}\right)} d^3r + \int_V \delta\chi_3 E_0^3 e^{i\left(\mathbf{k}_{3\omega}\cdot\mathbf{r}-2\mathbf{k}_\mathrm{T}\cdot\mathbf{r}-\mathbf{k}_\mathrm{D}\cdot\mathbf{r}+\mathbf{K}_\mathrm{NL}\cdot\mathbf{r}\right)} d^3r. \tag{6.28}$$

Equating the argument in the first integral to zero we obtain

$$\mathbf{k}_{3\omega}\cdot\mathbf{r} - 2\mathbf{k}_\mathrm{T}\cdot\mathbf{r} - \mathbf{k}_\mathrm{D}\cdot\mathbf{r} = 0, \tag{6.29}$$

which is equivalent to Equation 6.2. Likewise Equation 6.3 can be derived in a similar manner. As was seen previously, Equation 6.2 is not phase-matched and therefore Equation 6.29 is not exactly equal to zero. However it is still possible to have *unphase*-matched THG at the expense of low efficiency. The efficiency of THG for the SFG interaction was estimated using the responsivity of GaP photodetectors to be on the order of 10^{-4}.

6.5 Summary

We have shown new conditions for THG from a TBG in PTR glass illuminated by high intensity infrared femtosecond pulses. The two new interactions correspond to Bragg diffraction at 3ω and a three photon interaction with the modulated nonlinear refractive index of PTR glass. We measured the angular selectivity of THG for the two-beam THG condition. A simple theoretical model assuming SFG was used to explain the measured angular profiles.

CHAPTER SEVEN: CONCLUSION

7.1 Thesis Summary

A new approach for fabricating phase optical elements in PTR glass has been shown. It was demonstrated that ultrashort laser pulses with intensity below the laser-induced damage threshold photoionize PTR glass and subsequently lead to a negative refractive index change after thermal development. The photosensitizing dopant cerium was not necessary for photosensitivity because ultrashort laser pulses photoionize the glass matrix. Filaments that formed in PTR glass during irradiation were a result of balancing between self-focusing and defocusing by free electron generation. The free electrons were generated by strong electric field ionization and Keldysh theory was used to estimate a value of about 10^{19} cm^{-3} for the free-electron density. Optical microscopy and scattering probe measurements showed that for short exposure times it was possible to have photoionization without laser-induced optical damage. The dependence of refractive index change on laser intensity and laser dosage was measured and showed that the refractive index change is predictable and controllable. A phase Fresnel lens optical element was designed and fabricated in PTR glass by exposure to IR ultrashort laser pulses.

The interaction of PTR glass volume gratings with ultrashort laser pulses was studied in two laser intensity regimes. At intensities below ~10^{12} W/cm^2 the diffraction efficiency of volume gratings was accurately predicted using Kogelnik theory taking into account the spectral selectivity of the grating on the spectral bandwidth of the laser pulse. Angular divergence and pulse front tilt of a pulse after diffraction by a single TBG could be compensated by utilizing a volume grating pair arrangement. At intensities of irradiation above ~10^{12} W/cm^2 nonlinear generation and diffraction of third harmonic was observed for three cases. The three interactions corresponded to sum-frequency generation, front-surface THG generation, and THG due to phase-matching with a grating formed by modulation of the nonlinear refractive index in PTR glass.

7.2 Outlook

PTR glass offers a new possibility for creating optical elements in glass by ultrashort laser pulse exposure. Previously, micromachining of glass by intense ultrashort laser pulses was performed in one step, i.e. direct writing, in order to change the refractive index of glass. This process requires very intense pulses which cause optical breakdown or large permanent structuration on the order of the laser wavelength. Both of these effects exhibit strong scattering and are therefore not favorable for fabricating low loss optical elements. With PTR glass it is unnecessary (even undesirable) to directly change the refractive index. The exposure step should be able to photoionize the glass but not cause permanent changes. It is during the second step, thermal development, when the refractive index is modified due to the formation of nanocrystals. Because the nanocrystals are transparent and small in size they allow one to fabricate phase optical elements with minimal losses due to absorption or scattering. In general, focused ultrashort laser pulses and a 3D translation stage would allow one to fabricate any arbitrary volume phase pattern in PTR glass. Moreover holographic techniques can be employed to create optical elements in PTR glass using infrared ultrashort laser pulses. These two directions, arbitrary phase plate recording and holographic recording, require further investigation.

The mechanism responsible for nonlinear photosensitivity, strong electric field ionization as modeled by Keldysh theory, requires more detailed study and justification of its applicability to disordered solids such as glass. PTR glass is unique in that single-shot filamentation and nonlinear photoionization by ultrashort laser pulses does not require real-time instantaneous measurements. After exposure a PTR glass sample can be thermally developed in such a manner to grow large size microcrystals rather than the typical nanocrystals. This allows one to use optical microscopy to observe the distribution and morphology of the crystals. Since the distribution of the crystals corresponds to how the laser pulse photoionized the glass it is possible to study the effects of instantaneous electronic processes in glass without pump-probe or other real-time experiments.

Laser-induced damage in glass by ultrashort laser pulses occurred only after several tens of thousands of pulses. Because the repetition rate of the lasers was 1 kHz (1 msec between pulses) there was sufficient time for electronic relaxation and thus damage could not occur by avalanche breakdown. The morphology of damage as seen by optical microscopy showed a peculiar strucuture atypical of fracture damage. The mechanism and characteristics of laser-induced by ultrashort laser pulses requires further investigation.

It was seen that a volume grating pair arrangement is desirable for correcting pulse distortions that occur after diffraction by a single volume grating. In fact volume gratings have the additional property that they exhibit angular selectivity. This property can be used to force a laser to operate with only a single transverse mode. It would be interesting to place a volume grating pair inside a Ti:sapphire oscillator to achieve single transverse mode generation of ultrashort pulses.

We saw that non-collinear THG results from the interaction of PTR glass volume holograms with high-intensity ultrashort laser pulses. Unfortunately the efficiency of conversion was low due to a limited interaction distance as well as a small value of nonlinear refractive index in PTR glass. One approach to obtain higher efficiency would be to dope PTR glass with elements that have large nonlinearities. In the case of non-collinear THG due to nonlinear index modulation one could expect that the photo-thermo-refractive responsible for nanocrystal growth would also have the effect of causing a distribution in the elements with large nonlinearities. If this modulation follows the same distribution as the linear modulation then we could expect higher conversion efficiency of fundamental into third harmonic.

Finally, it should be noted that all experiments related to testing volume holograms with ultrashort laser pulses in this thesis dealt with transmitting Bragg gratings in PTR glass. Reflecting Bragg gratings were not utilized because their spectral selectivity (typically less than 1 nm) does not allow for efficient diffraction of ultrashort laser pulses (the spectral bandwidth of the pulses is typically larger than 6 nm). However chirped Bragg gratings in PTR glass offer large spectral bandwidth selectivity and therefore can be studied using the techniques (e.g. spectral interferometry) employed in this thesis.

APPENDIX: COUPLED-WAVE THEORY

A.1 Electromagnetic Wave Propagation

All electromagnetic phenomena are governed by the fundamental laws known as Maxwell's equations. They can be written as

$$\nabla \times \mathbf{E} + \frac{\partial \mathbf{B}}{\partial t} = 0, \tag{A.1}$$

$$\nabla \times \mathbf{H} - \frac{\partial \mathbf{D}}{\partial t} = \mathbf{J}, \tag{A.2}$$

$$\nabla \cdot \mathbf{D} = \rho, \tag{A.3}$$

$$\nabla \cdot \mathbf{B} = 0, \tag{A.4}$$

which together with the Lorentz force law,

$$\mathbf{F} = e(\mathbf{E} + \mathbf{v} \times \mathbf{B}), \tag{A.5}$$

summarize all classical electrodynamic phenomena. The vectors in the above equations are identified as follows: **E** is called the electric field [V/m], **D** is the electric displacement [C/m^2], **B** is the magnetic field [Wb/m^2], **H** we will call the "H" field [A/m], **J** is the volume current density [A/m^2], and **v** is the velocity of a particle with unit charge. The scalar quantities in the above equations are ρ for charge density [C/m^3] and *e* for a unit of electric charge [C]. The great success of Maxwell's theory was that it correctly predicted the existence and properties of electromagnetic waves. In present form the fields are functions of position and time, i.e. **E**(**r**, *t*). It is useful to express the fields as functions of position and frequency. This can be done by assuming a simple sinusoidal dependence. The relationship we use is

$$\mathbf{A}(\mathbf{r},t) = \mathbf{A}(\mathbf{r})\exp(i\omega t), \tag{A.6}$$

where **A(r)** is an arbitrary vector. Fourier analysis allows one to reconstruct a complex time dependent function as a linear superposition of simple sinusoids. If we make certain assumptions about the material response to the fields we can write Maxwell's equations in terms of just **E** and **H**. We characterize a medium in the absence of free charge (i.e. ρ equal to zero) by a conductivity σ, dielectric constant ε, permeability μ and use the following constitutive relationships

$$\mathbf{D} = \varepsilon \mathbf{E}, \tag{A.7}$$

$$\mathbf{B} = \mu \mathbf{H}, \tag{A.8}$$

$$\mathbf{J} = \sigma \mathbf{E}, \tag{A.9}$$

to rewrite Maxwell's equations as

$$\nabla \times \mathbf{E} + i\omega\mu \mathbf{H} = 0, \tag{A.10}$$

$$\nabla \times \mathbf{H} - (i\omega\varepsilon + \sigma)\mathbf{E} = 0, \tag{A.11}$$

$$\nabla \cdot \varepsilon \mathbf{E} = 0, \tag{A.12}$$

$$\nabla \cdot \mu \mathbf{H} = 0. \tag{A.13}$$

To derive the wave equation for this medium we take a curl operation on Equation A.10 and eliminate the $\nabla \times \mathbf{H}$ term by using Equation A.11. We then have

$$\nabla \times (\nabla \times \mathbf{E}) + i\omega\mu(i\omega\varepsilon + \sigma)\mathbf{E} = 0. \tag{A.14}$$

The first term in Equation A.14 can be expanded using the vector identity

$$\nabla \times (\nabla \times \mathbf{E}) = \nabla(\nabla \cdot \mathbf{E}) - \nabla^2 \mathbf{E}. \tag{A.15}$$

We see that the first term on the right hand side of Equation A.15 is zero from Equation A.12. Thus, Equation A.14 becomes

$$\nabla^2 \mathbf{E} + k^2 \mathbf{E} = 0, \tag{A.16}$$

where

$$k^2 = \omega^2 \mu\varepsilon - i\omega\mu\sigma. \tag{A.17}$$

Equation A.16 is known as the Helmholtz wave equation.

A.2 Modeling Volume Gratings

An exact solution to wave diffraction by a volume grating requires solving Maxwell's equation for a material with periodic variation in dielectric constant. The goal is to solve Equation A.16 assuming

$$\varepsilon = \varepsilon_0 \left[\varepsilon_r + \varepsilon_1 \exp\left(i \mathbf{K} \cdot \mathbf{r} \right) \right], \tag{A.18}$$

and applying the appropriate boundary conditions. This is a formidable task and approximations are necessary to reach a solution. The most useful theoretical approach to solving this problem is coupled wave theory. Other approaches include modal theory and perturbation theory.

A.3 Kogelnik Model

Coupled-wave theory was first applied to volume Bragg gratings in the classic paper by H. Kogelnik in 1969 [8]. The theory assumes monochromatic plane wave light incident on an infinite grating at or near the Bragg angle. Only two waves are assumed to be important, the incoming reference wave and an outgoing signal wave. We consider a grating of thickness L with surface boundaries parallel to the x-axis. The fringe planes are perpendicular to the x-z plane and are slanted with respect to the grating boundary. The grating vector $\mathbf{K}$ is oriented perpendicular to the fringe planes. Incident light, polarized along the y-axis, arrives at angle θ with respect to the grating surface normal. The angle θ is measured *in* the medium. Figure A.1 shows the situation which we have described.

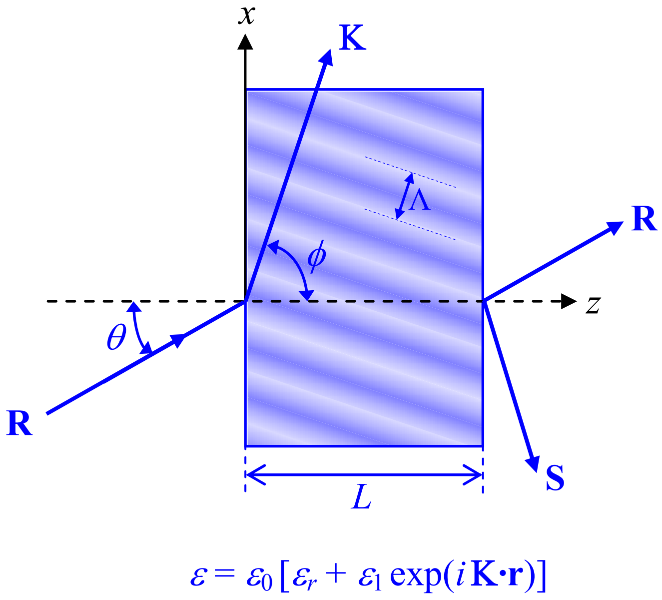

Figure A.1. Geometry for diffraction by a volume Bragg grating.

We will consider a lossless, nonmagnetic, material which allows us to make the following simplifications

$$\varepsilon = \varepsilon_0 [\varepsilon_r + \varepsilon_1 \cos(\mathbf{K}\cdot\mathbf{r})], \tag{A.19}$$

$$\mu = \mu_0, \tag{A.20}$$

$$\sigma = 0, \tag{A.21}$$

and hence the wave equation inside the grating becomes

$$\nabla^2 \mathbf{E} + \frac{\omega^2}{c^2} \varepsilon_r \left[1 + \frac{\varepsilon_1}{\varepsilon_r} \cos(\mathbf{K}\cdot\mathbf{r}) \right] \mathbf{E} = 0. \tag{A.22}$$

We will see that it is useful to introduce an average propagation vector β and a coupling coefficient κ and rewrite Equation A.22 as

$$\nabla^2 \mathbf{E} + \beta^2 \left[1 + 4\frac{\kappa}{\beta} \cos(\mathbf{K}\cdot\mathbf{r}) \right] \mathbf{E} = 0, \tag{A.23}$$

where

$$\beta = \frac{\omega}{c}\sqrt{\varepsilon_r}, \tag{A.24}$$

$$\kappa = \frac{1}{4}\frac{\omega}{c}\varepsilon_1 \Big/ \sqrt{\varepsilon_r}\,. \tag{A.25}$$

The total electric field is the sum of the reference and signal waves and is written as

$$\mathbf{E} = \mathbf{R}\, e^{-i(\boldsymbol{\rho}\cdot\mathbf{r})} + \mathbf{S}\, e^{-i(\boldsymbol{\sigma}\cdot\mathbf{r})}, \tag{A.26}$$

where **ρ** and **σ** are the propagation vectors for the reference and signal waves respectively. Since we assumed TE polarization the vector wave equation is actually a scalar equation

$$\mathrm{E} = \mathrm{R}(z)e^{-i(\boldsymbol{\rho}\cdot\mathbf{r})} + \mathrm{S}(z)e^{-i(\boldsymbol{\sigma}\cdot\mathbf{r})}, \tag{A.27}$$

and we can write the reference wave propagation vector as

$$\boldsymbol{\rho} = \beta \begin{pmatrix} \sin\theta \\ 0 \\ \cos\theta \end{pmatrix}. \tag{A.28}$$

The signal wave propagation vector is determined by interaction of the reference wave interaction with the grating vector

$$\boldsymbol{\sigma} = \boldsymbol{\rho} - \mathbf{K}, \tag{A.29}$$

where the grating vector is given by

$$\mathbf{K} = K \begin{pmatrix} \sin\phi \\ 0 \\ \cos\phi \end{pmatrix}; \qquad K = 2\pi/\Lambda, \tag{A.30}$$

and Λ is the spatial period of the grating. We now substitute Equation A.27 into Equation A.23 which results in the following set of coupled wave equations

$$c_{\mathrm{R}} \frac{\mathrm{dR}}{\mathrm{dz}} = -i\kappa \mathrm{S}, \tag{A.31}$$

$$c_{\mathrm{S}} \frac{\mathrm{dS}}{\mathrm{dz}} + i\vartheta \mathrm{S} = -i\kappa \mathrm{R}, \tag{A.32}$$

where

$$c_{\mathrm{R}} = \rho_z / \beta = \cos\theta, \tag{A.33}$$

$$c_{\mathrm{S}} = \sigma_z / \beta = \cos\theta - \frac{\mathrm{K}}{\beta}\cos\phi, \tag{A.34}$$

$$\vartheta \equiv \left(\beta^2 - \sigma^2\right) / 2\beta = \mathrm{K}\cos(\phi - \theta) - \frac{\mathrm{K}^2}{4\pi n}\lambda. \tag{A.35}$$

The general solution to the coupled wave equations is

$$\mathrm{R}(z) = r_1 \exp(\gamma_1 z) + r_1 \exp(\gamma_2 z), \tag{A.36}$$

$$\mathrm{S}(z) = s_1 \exp(\gamma_1 z) + s_1 \exp(\gamma_2 z), \tag{A.37}$$

The constants r_1, r_2, s_1, and s_2 are determined by the boundary conditions. The constants γ_1 and γ_2 are determined by substituting Equations A.36 & A.37 into the coupled wave equations. The result is

$$\gamma_{1,2} = -i\frac{\vartheta}{2c_{\mathrm{S}}} \pm \frac{1}{2}\left[-\frac{\vartheta}{c_{\mathrm{S}}} - 4\frac{\kappa^2}{c_{\mathrm{R}} c_{\mathrm{S}}}\right]^{1/2}. \tag{A.38}$$

Let us multiply Equation A.31 by R* and add the result to the complex conjugate of Equation A.31 multiplied by R. The result is

$$2c_{\mathrm{R}}\frac{\mathrm{d}}{\mathrm{dz}}\mathrm{RR}^* + i\kappa SR^* - i\kappa S^* R = 0. \tag{A.39}$$

Now let us derive an energy balance equation which will allow us to determine the efficiency of energy conversion from the reference wave into the signal wave. We begin by multiplying Equation A.32 by S* and adding the result to the complex conjugate of Equation A.32 multiplied by S. The result is

$$2c_{\mathrm{S}}\frac{\mathrm{d}}{\mathrm{dz}}\mathrm{SS}^* - i\kappa SR^* + i\kappa S^* R = 0. \tag{A.40}$$

Adding together Equations A.39 & A.40 results in the following energy balance expression

$$\frac{\mathrm{d}}{\mathrm{dz}}\left(c_{\mathrm{R}} RR^* + c_{\mathrm{S}}\mathrm{SS}^*\right) = 0, \tag{A.41}$$

which yields

$$c_{\mathrm{R}} RR^* + c_{\mathrm{S}} \mathrm{SS}^* = C, \tag{A.42}$$

where C is a constant. To determine C we consider that initially the reference power RR^* to be 1. At this initial time no propagation (and hence no energy coupling from reference into signal) has occurred. Thus the signal power SS^* must be zero. Hence the constant C is equal to c_{R}. We can then solve Equation A.42 for the reference power RR^* and obtain

$$RR^* = 1 - \frac{c_{\mathrm{S}}}{c_{\mathrm{R}}} \mathrm{SS}^*. \tag{A.43}$$

This expression tells us about t power flow from the reference wave into the signal wave. If there is no energy coupling, i.e. $SS^* = 0$, then $RR^* = 1$. If all energy is depleted from the reference wave, i.e. $RR^* = 0$, then $SS^* = 1$. The definition for diffraction efficiency is given by

$$\eta = \frac{|c_{\mathrm{S}}|}{c_{\mathrm{R}}} \mathrm{SS}^*, \tag{A.44}$$

where a magnitude sign is included on c_{s} to ensure that by definition diffraction efficiency is always positive. The value of S depends on boundary conditions. In the next two sections we consider separately the boundary conditions for transmitting and reflecting Bragg gratings.

A.4 Transmitting Bragg Grating

The transmitting Bragg grating geometry is shown in Figure A.2. The boundary conditions are $\mathbf{R}(0) = 1$ and $\mathbf{S}(0) = 0$. We want to solve for the diffracted signal $\mathbf{S}(L)$.

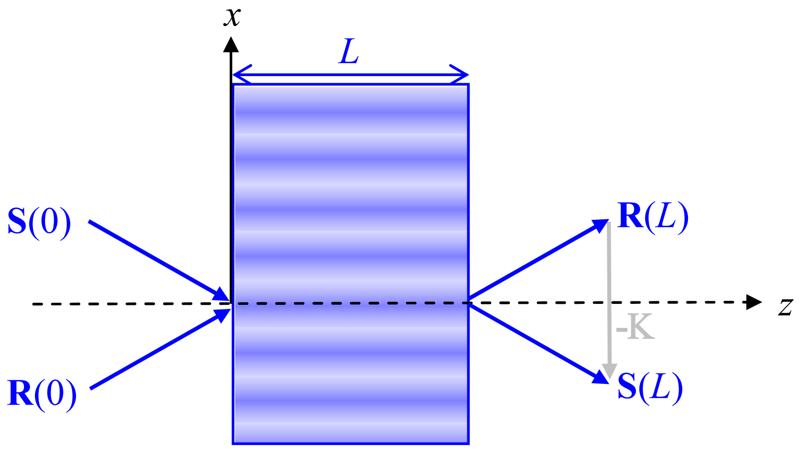

Figure A.2. Geometry for a transmitting Bragg grating.

Using the boundary conditions the expression for the signal field from a transmitting Bragg grating is

$$\mathrm{S} = -i\left(\frac{c_{\mathrm{R}}}{c_{\mathrm{S}}}\right)^{1/2} e^{-i\xi} \frac{\sin\sqrt{\nu^2+\xi^2}}{\sqrt{1+\xi^2/\nu^2}}, \qquad (\text{A.45})$$

where

$$\nu = \frac{\pi n_1 L}{\lambda\sqrt{c_{\mathrm{R}} c_{\mathrm{S}}}}, \qquad (\text{A.46})$$

$$\xi = \frac{\vartheta L}{2c_{\mathrm{S}}}. \qquad (\text{A.47})$$

The equation for diffraction efficiency is obtained by substituting Equation A.45 into Equation A.44

$$\eta = \frac{\sin^2\sqrt{\nu^2+\xi^2}}{1+\xi^2/\nu^2}. \qquad (\text{A.48})$$

A.5 Reflecting Bragg Grating

The reflecting Bragg grating geometry is shown in Figure A.3. The boundary conditions are **R**(0) = 1 and **S**(L) = 0. We want to solve for the diffracted signal **S**(0).

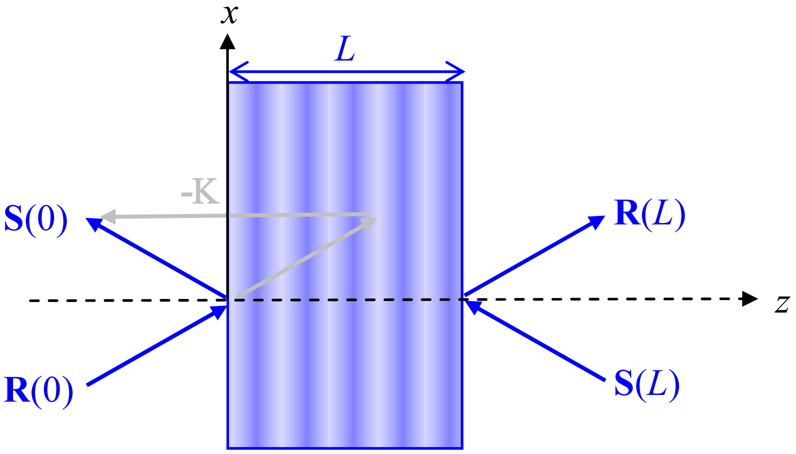

Figure A.3. Geometry for a reflecting Bragg grating.

Using the boundary conditions the expression for the signal field from a transmitting Bragg grating is

$$\mathrm{S} = \left(\frac{c_\mathrm{R}}{c_\mathrm{S}}\right)^{1/2} \Big/ \left\{ i\xi/\nu + \left(1 - \xi^2/\nu^2\right)^{1/2} \cdot \coth\left(\nu^2 - \xi^2\right)^{1/2} \right\}, \tag{A.49}$$

where

$$\nu = i\frac{\pi n_1 L}{\lambda\sqrt{c_\mathrm{R} c_\mathrm{S}}}, \tag{A.50}$$

$$\xi = -\frac{\vartheta L}{2c_\mathrm{S}}. \tag{A.51}$$

The equation for diffraction efficiency is obtained by substituting Equation A.49 into Equation A.44

$$\eta = \left[1 + \frac{1 - \xi^2 / \nu^2}{\sinh^2 \sqrt{\nu^2 - \xi^2}} \right]^{-1}. \tag{A.52}$$

A.6 Gaussian Wave Theory

Kogelnik's coupled wave theory for volume grating diffraction models all the electromagnetic waves as plane waves. In practice laser beams are best modeled as Gaussian waves. Ref. [85] shows that divergent and polychromatic waves with Gaussian profiles require a convolution integral to be performed in order to correctly predict the diffraction efficiency. The adjusted value of the diffraction efficiency $\eta(b,w)$ for a diffraction-limited beam is

$$\eta(b,w) = \frac{2}{\pi} \frac{1}{wb} \iint \eta(\theta,\lambda)\, G(\theta,\lambda,b,w) d\theta\, d\lambda, \tag{A.53}$$

where

$$G(\theta,\lambda,b,w) = \exp\left[-2\left(\frac{\theta - \theta_{Br}}{b} \right)^2 \right] \exp\left[-2\left(\frac{\lambda - \lambda_0}{w} \right)^2 \right], \tag{A.54}$$

and

$$b = \frac{2\lambda_0}{\pi D}. \tag{A.55}$$

In the above equations the parameters are defined as follows: w is the HWe^{-2}M spectral width, λ_0 is the central wavelength, b is the beam divergence, D is the beam diameter, θ_{Br} is the Bragg angle, and $\eta(\theta,\lambda)$ is the plane wave diffraction efficiency given by either Equation A.48 or Equation A.52. When the beam divergence or beam spectral width becomes comparable with the grating selectivity the maximal diffraction efficiency decreases significantly.

LIST OF REFERENCES

[1] D. Gabor, "A new microscopic principle," *Nature* **161**, 777-778 (1948); "Microscopy by reconstructed wave fronts," *Proceedings of the Royal Society of London, Series A, Mathematical and Physical Sciences* **197**, 454-487 (1949); "Microscopy by reconstructed wave fronts: II," *Proceedings of the Physical Society of London, Series B, Biological Sciences* **64**, 449 (1951).

[2] T.H. Maiman, "Stimulated Optical Radiation in Ruby," *Nature* **187**, 493-494 (1960).

[3] A. Javan, W.R. Bennett Jr., and D.R. Herriott, "Population inversion and continuous optical maser oscillation in a gas discharge containing a He-Ne mixture," *Physical Review Letters* **6**, 106-113 (1961).

[4] E.N. Leith and J. Upatnieks, "Reconstructed wavefronts and communication theory," *Journal of the Optical Society of America* **52**, 1123-1130 (1962); "Wavefront reconstruction with continuous tone objects," *Journal of the Optical Society of America* **53**, 1377-1381 (1963); "Wavefront reconstruction with diffused illumination and three-dimensional objects," *Journal of the Optical Society of America* **54**, 1295-1301 (1964).

[5] Y.N. Denisyuk, "Photographic reconstruction of the optical properties of an object in its own scattered radiation field," *Soviet Physics-Doklady* **7**, 543 (1962).

[6] P.J. van Heerden, "Theory of optical information storage in solids," *Applied Optics* **2**, 393-400 (1963).

[7] W.H. Bragg and W.L. Bragg, "The reflection of X-rays by crystals," *Proceedings of the Royal Society of London, Series A, Mathematical and Physical Sciences* **88**, 428-438 (1913).

[8] H. Kogelnik, "Coupled wave theory for thick hologram gratings," *The Bell System Technical Journal* **48**, 2909-2947 (1969).

[9] R.W. Gurney and N.F. Mott, "The theory of the photolysis of silver bromide and the photographic latent image," *Proceedings of the Royal Society of London, Series A, Mathematical and Physical Sciences* **164**, 151-167 (1938).

[10] J.W. Mitchell, "On the electronic conductivity of crystals of silver halides", *Philosophical Magazine* **2**, 1276-1281 (1957).

[11] J.W. Mitchell, "Elementary processes in the concentration theory of latent image formation," *Journal of Imaging Science* **31**, 1 (1987).

[12] A. Ashkin, G.D. Boyd, J.M. Dziedzic, R.G. Smith, A.A. Ballman, J.J. Levinstein, and K. Nassau, "Optically-induced refractive index inhomogeneities in $LiNbO_3$ and $LiTaO_3$," *Applied Physics Letters* **9**, 72-74 (1966).

[13] N.V. Kukhtarev, V.B. Markov, S.G. Odulov, M.S. Soskin, and V.L. Vinetskii, "Holographic storage in electro-optic crystals. Beam coupling and light amplification," *Ferroelectrics* **22**, 961-964 (1979).

[14] S.D. Stookey, “Photosensitive glass – A new photographic medium,” *Industrial and Engineering Chemistry* **41**, 856-861 (1949).

[15] S.D. Stookey, G.H. Beall, and J.E. Pierson, “Full-color photosensitive glass,” *Journal of Applied Physics* **49**, 5114-5123 (1978).

[16] N.F. Borrelli, D.L. Morse, and A. Sachenik, “Integral photosensitive optical device and method,” *United States Patent* 4,514,053 (1985).

[17] V.A. Borgman, L.B. Glebov, N.V. Nikonorov, G.T. Petrovskii, V.V. Savvin, and A.D. Tsvetkov, “Photo-thermal refractive effect in silicate glasses,” *Soviet Physics-Doklady* **34**, 1011-1013 (1989).

[18] O.M. Efimov, L.B. Glebov, L.N. Glebova, K.C. Richardson, and V.I. Smirnov, “High-efficiency Bragg gratings in photothermorefractive glass,” *Applied Optics* **38**, 619-627 (1999).

[19] O.M. Efimov, L.B. Glebov, V.I. Smirnov, and L. Glebova, “Process for production of high efficiency volume diffractive elements in photo-thermo-refractive glass,” *United States Patent* 6,586,141 (2003).

[20] O.M. Efimov, L.B. Glebov, and V.I. Smirnov, “High efficiency volume diffractive elements in photo-thermo-refractive glass,” *United States Patent* 6,673,497 (2004).

[21] G.B. Venus, A. Sevian, V.I. Smirnov, and L.B. Glebov, “High-brightness narrow-line laser diode source with volume Bragg-grating feedback,” *Proceedings of the SPIE* **5711**, 166-176 (2005).

[22] G.B. Venus, L. Glebov, V. Rotar, V. Smirnov, P. Crump, and J. Farmer, “Volume Bragg semiconductor lasers with near diffraction limited divergence,” *Proceedings of the SPIE* **6216**, 621602 (2006).

[23] A. Sevian, O. Andrusyak, I. Ciapurin, V. Smirnov, G. Venus, and L. Glebov, “Efficient power scaling of laser radiation by spectral beam combining,” *Optics Letters* **33**, 384-386 (2008).

[24] G.H. Beall, D.A. Duke, “Transparent glass ceramics,” *Journal of Materials Science* **4**, 340-352 (1969).

[25] F.J. McClung and R.W. Hellwarth, “Giant optical pulsations from ruby,” *Journal of Applied Physics* **33**, 828-829 (1962).

[26] D. Strickland and G. Mourou, “Compression of amplified chirped optical pulses,” *Optics Communications* **56**, 219-221 (1985).

[27] E.B. Treacy, “Optical pulse compression with diffraction grating,” *IEEE Journal of Quantum Electronics* **QE-5**, 454-458 (1969).

[28] R.W. Boyd, *Nonlinear Optics*, 3rd edition, Academic Press (2008).

[29] H.A. Lorentz, “Versuch einer theorie der electrischen und optischen erscheinungen bewegten koerpern,” *Leiden*, (1895).

[30] M. Hercher, “Laser-induced damage in transparent media,” *Journal of the Optical Society of America* **54**, 563 (1964).

[31] N. Bloembergen, “Laser induced electric breakdown in solids,” *IEEE Journal of Quantum Electronics* **QE-10**, 375-386 (1974).

[32] A.A. Manenkov, “New results on avalanche ionization as a laser damage mechanism in transparent solids,” *National Bureau of Standards (U.S.), Special Publication* **509**, 455 (1977).

[33] E.W. Van Stryland, M.J. Soileau, A.L. Smirl, and William E. Williams, “Pulsewidth and focal volume dependence of laser-induced breakdown,” *Physical Review B* **23**, 2144 (1981).

[34] M. Sparks, D.L. Mills, R. Warren, T. Holstein, A.A. Maradudin, L.J. Sham, E. Loh, Jr., and D.F. King, “Theory of electron-avalanche breakdown in solids,” *Physical Review B* **24**, 3519 (1981).

[35] L.B. Glebov, O.M. Efimov, M.N. Libenson, and G.T. Petrovskii, “New ideas about the intrinsic optical breakdown of tranparent insulators,” *Soviet Physics–Doklady* **31**, 326-328 (1986).

[36] S.C. Jones, P. Braunlich, R.T. Casper, and X.A. Shen, “Recent progress on laser-induced modifications and intrinsic bulk damage of wide-gap optical materials,” *Optical Engineering* **28**, 1039-1068 (1989).

[37] E.N. Glezer, M. Milosavljevic, L. Huang, R.J. Finlay, T.-H. Her, J.P. Callan, and E. Mazur, “Three-dimensional optical storage inside transparent materials,” *Optics Letters* **21**, 2023-2025 (1996).

[38] K.M. Davis, K. Miura, N. Sugimoto, and K. Hirao, “Writing waveguides in glass with a femtosecond laser,” *Optics Letters* **21**, 1729-1731 (1996).

[39] D. von der Linde and H. Schüler, “Breakdown threshold and plasma formation in femtosecond laser-solid interaction,” *Journal of the Optical Society of America B: Optical Physics* **13**, 216-222 (1996).

[40] L.B. Glebov, “Optical absorption and ionization of silicate glasses,” *Proceedings of the SPIE* **4347** 343-356 (2001).

[41] S.M. Avanesyan, S. Orlando, S.C. Langford, and J.T. Dickinson, “Through a glass, darkly: point defect production by ultrafast laser irradiation of alkali-containing silica glasses and alkali halide single crystals,” *Proceedings of the SPIE* **5647**, 501-512 (2005).

[42] H.L. Smith and A.J. Cohen, “Absorption spectra of cations in alkali-silicate glasses of high ultra-violet transmission” *Physics and Chemistry of Glasses* **4**, 173-187 (1963).

[43] F.P. Kapron, D.B. Keck, and R.D. Maurer, “Radiation losses in glass optical waveguides,” *Applied Physics Letters* **17**, 423-425 (1970).

[44] L.B. Glebov and V.I. Smirnov, “Interaction of photo-thermo-refractive glass with nanosecond pulses at 532 nm,” *Proceedings of the SPIE* **5273**, 396-401 (2003).

[45] L.A. Siiman, V.I. Smirnov, L.N. Glebova, and L.B. Glebov, “Nonlinear bleaching of induced absorption in PTR glass,” oral presentation at American Ceramic Society's Glass and Optical Materials Division annual meeting (2004).

[46] F. Bloch, “Über die quantenmechanik der elektronen in kristallgittern”, *Zeitschrift für Physik* **52**, 555 (1928).

[47] W.B. White, “Investigaton of phase separation by Raman spectroscopy,” *Journal of Non-Crystalline Solids* **49**, 321-329 (1982).

[48] W.H. Zachariasen, “The atomic arrangement in glass,” *Journal of the American Chemical Society* **54**, 162-162 (1932).

[49] N.F. Mott, “Electrons in glass,” http://nobelprize.org/nobel_prizes/physics/laureates/1977/mott-lecture.pdf (1977); *Reviews of Modern Physics* **50**, 203-209 (1978).

[50] P.W. Anderson, “Absence of diffusion in certain random lattices,” *Physical Review* **109**, 1492-1505 (1958).

[51] A.F. Ioffe and A.R. Regel, “Non-crystalline, amorphous, and liquid electronic semiconductors,” *Progress in Semiconductors* **4**, 237-291 (1960).

[52] S. John, “Electromagnetic absorption in a disordered medium near a photon mobility edge,” *Physical Review Letters* **53**, 2169-2172 (1984).

[53] T. Scwartz, S. Fishman, and M. Segev, “Localisation of light in disordered lattices,” *Electronics Letters* **44** (2008).

[54] N.F. Mott, “Electrons in disordered structures,” *Advances in Physics* **16**, 49-144 (1967).

[55] R.A. Weeks, “Paramagnetic resonance of lattice defects in irradiated quartz,” *Journal of Applied Physics* **27**, 1376-1381 (1956).

[56] L.B. Glebov, V.G. Dokuchaev, M.A. Petrov, and G.T. Petrovskii “Absorption spectra of color centers in alkali silicate glasses,” *Soviet Journal of Glass Physics and Chemistry* **16**, 31-38 (1990).

[57] L. Siiman and L. Glebov “Color center generation in sodium-calcium silicate glass by nanosecond and femtosecond laser pulses,” *Proceedings of the SPIE* **5991**, 599112 (2005).

[58] L.B. Glebov, “Kinetics modeling in photosensitive glass,” *Optical Materials* **25**, 413-418 (2004).

[59] O.M. Efimov, L.B. Glebov, and H.P. Andre, “Measurement of the induced refractive index in a photothermorefractive glass by a liquid-cell shearing interferometer,” *Applied Optics* **41**, 1864-1871 (2002).

[60] L.A. Siiman, J. Lumeau, L.B. Glebov, “Nonlinear photosensitivity of photo-thermo-refractive glass by high intensity laser irradiation,” *Journal of Non-Crystalline Solids* DOI: 10.1016/j.jnoncrysol.2008.05.051 (2008).

[61] O.M. Efimov, L.B. Glebov, S. Grantham, and M. Richardson, “Photoionization of silicate glasses exposed to IR femtosecond pulses,” *Journal of Non-Crystalline Solids* **253**, 58-67 (1999).

[62] G.M. Zverev, E.K. Maldutis, and V.A. Pashkov, “Development of self-focusing filaments in solid dielectrics,” *JETP Letters* **9**, 61-63 (1969).

[63] M.M.T. Loy, and Y.R. Shen, “Small-scale filaments in liquids and tracks of moving foci,” *Physical Review Letters* **22**, 994-997 (1969).

[64] A.N. Trukhin, M.N. Tolstoi, L.B. Glebov, and V.L. Savel’ev, “Elementary electronic excitations in pure sodium silicate glasses,” *Physica Status Solidi B: Basic Research* **99**, 155-162 (1980).

[65] S. Santran, M. Martinez-Rosas, L. Canioni, L. Sarger, L. Glebova, A. Tirpak, and L. Glebov, "Nonlinear refractive index of photo-thermo-refractive glass," *Optical Materials* **28**, 401–407 (2006).

[66] R.Y. Chiao, E. Garmire, and C.H. Townes, “Self-trapping of optical beams,” *Physical Review Letters* **13**, 479-482 (1964).

[67] R.R. Alfano, S.L. Shapiro, “Observation of self-phase modulation and small-scale filaments in crystals and glasses,” *Physical Review Letters* **24**, 592-594 (1970).

[68] V.I. Bespalov and V.I. Talanov, “Plane wave instability and filamentation of light,” *JETP Letters* **3**, 307-310 (1966).

[69] H.J. Fitting, A.N. Trukhin, T. Barfels, B. Schmidt, and A. Von Czarnowsi, “Radiation induced effects in SiO2,” *Radiation Effects & Defects in Solids* **157**, 575-581 (2002).

[70] W. Franz, “Einfluß eines elektrischen feldes auf eine optische absorptionskante,” *Zeitschrift für Naturforschung* **13a**, 484-491 (1958).

[71] L.V. Keldysh, “Behavior of nonmetallic crystals in strong electric fields,” *Soviet Physics-JETP* **6**, 763 (1958).

[72] L.V. Keldysh, ‘‘Ionization in the field of a strong electromagnetic wave,’’ *Soviet Physics-JETP* **20**, 1307-1314 (1965).

[73] S.A. Slattery and D.N. Nikogosyan, “Two-photon absorption at 211 nm in fused silica, crystalline quartz and some alkali halides,” *Optics Communications* **228**, 127-131 (2003).

[74] J.N. Chróinín, A. Dragomir, J.G. McInerney, and D.N. Nikogosyan, “Accurate determination of two-photon absorption coefficients in fused silica and crystalline quartz at 264 nm,” *Optics Communications* **187**, 185-191 (2001).

[75] E. Yablonovitch and N. Bloembergen, “Avalanche ionization and the limiting diameter of filaments induced in by light pulses in transparent media,” *Physical Review Letters* **29**, 907-910 (1972).

[76] A. Brodeur and S.L. Chin, ‘‘Ultrafast white-light continuum generation and self-focusing in transparent condensed media,’’ *Journal of the Optical Society of America B: Optical Physics* **16**, 637-650 (1999).

[77] J.B. Ashcom, R.R. Gattass, C.B. Schaffer, and Eric Mazur, “Numerical aperture dependence of damage and supercontinuum generation from femtosecond laser pulses in bulk fused silica,” *Journal of the Optical Society of America B: Optical Physics* **23**, 2317-2322 (2006).

[78] O. Efimov, S. Juodkazis, and H. Misawa, “Intrinsic single- and multiple-pulse laser-induced damage in silicate glasses in the femtosecond-to-nanosecond region,” *Physical Review A* **69**, 042903 (2004).

[79] D.G. Papazoglou, I. Zergioti, and S. Tzortzakis, “Plasma strings from ultraviolet laser filaments drive permanent structural modifications in fused silica,” *Optics Letters* **32**, 2055-2057 (2007).

[80] N.T. Nguyen, A. Saliminia, W. Liu, S.L. Chin, and R. Vallée, ‘‘Optical breakdown versus filamentation in fused silica by use of femtosecond infrared laser pulses,’’ *Optics Letters* **28**, 1591-1593 (2003).

[81] J. Qiu, M. Shirai, T. Makaya, J. Si, X. Jiang, C. Zhu, and K. Hirao, “Space-selective precipitation of metal nanoparticles inside glasses,” *Applied Physics Letters* **81**, 3040-3042 (2002).

[82] Y. Cheng, K. Sugioka, M. Masuda, K. Shihoyama, K. Toyoda, and K. Midorikawa, “Optical gratings embedded in photosensitive glass by photochemical reaction using a femtosecond laser,” *Optics Express* **11**, 1809-1809-1816 (2003).

[83] L. Siiman, J. Lumeau, and L.B. Glebov, “Sensitivity of photo-thermo-refractive glass to IR femtosecond pulses: application for the recording of phase elements,” *CLEO Europe* **CE4-5-TUE**, (2007).

[84] H. Dammann, "Blazed Synthetic Phase-Only Holograms," Optik 31, 95-104 (1970).

[85] I.V. Ciapurin, L.B. Glebov, and V.I. Smirnov, “Modeling of Gaussian beam diffraction on volume Bragg gratings in PTR glass,” *Proceedings of the SPIE* **5742**, 183-194 (2005).

[86] Z. Bor, B. Racz, G. Szabo, M. Hilbert, H.A. Hazim, “Femtosecond pulse front tilt caused by angular dispersion”, *Optical Engineering* **32**, 2501 (1993).

[87] L. Lepetit, G. Cheriaux, and M. Joffre, “Linear techniques of phase measurement by femtosecond spectral interferometry for applications in spectroscopy”, *Journal of the Optical Society of America B: Optical Physics* **12**, 2467 (1995).

[88] E.B. Treacy, “Optical pulse compression with diffraction gratings,” *IEEE Journal of Quantum Electronics* **5**, 454-458 (1969).

[89] R. Trebino, *Frequency-Resolved Optical Gating: The measurement of ultrashort laser pulses*, Kluwer Academic Publishers (2000).

[90] T. Yang, P. Ho, A. Katz, R. Alfano, and R. Ferrante, “Femtosecond laser pulse compression using volume phase transmission holograms”, *Applied Optics* **24**, 2021 (1985).

[91] K.-H. Liao, M.-Y. Cheng, E. Flecher, V.I. Smirnov, L. Glebov, and A. Galvanauskas, "Large-aperture chirped volume Bragg grating based fiber CPA system," *Optics Express* **15**, 4876-4882 (2007).

[92] V.I. Smirnov, S. Juodkazis, V. Dubikovsky, J. Hales, B. Ya. Zel’dovich, H. Misawa, and L.B. Glebov, “Resonant third harmonic generation by femtosecond laser pulses on Bragg grating in photosensitive silicate glass,” *Conference on Lasers and Electro-Optics* CLEO-2002 paper CTuG7.

[93] S Juodkazis, E Gaizauskas, V Jarutis, J Reif, S Matsuo, and H Misawa, “Optical third harmonic generation during femtosecond pulse diffraction in a Bragg grating,” *Journal of Physics D: Applied Physics* **39**, 50-53 (2006).

[94] L. Siiman, J. Lumeau, L. Canioni, and L.B. Glebov, “Third harmonic generation by volume Bragg grating in photo-thermo-refractive glass irradiated by IR femtosecond pulses,” *Proceedings of the SPIE* **6875** 687510 (2008).

[95] L. Siiman, J. Lumeau, L. Glebov, and L. Canioni, “Angular selectivity of third harmonic generated in a PTR transmitting Bragg grating by femtosecond pulses,” *23rd Advanced Solid State Photonics (ASSP) Topical Meeting: ASSP Technical Digest* **WB31**, (2008).

[96] J.X. Cheng and X.S. Xie, “Green’s function formulation for third-harmonic generation microscopy,” *Journal of the Optical Society of America B: Optical Physics* **19**, 1604-1610 (2007).